DOKUZ EYLÜL UNIVERSITY
GRADUATE SCHOOL OF NATURAL AND APPLIED SCIENCES

DETERMINATION OF MECHANICAL PROPERTIES OF COMPOSITE MATERIALS REINFORCED BY MINERAL

by
Dilek ATİLLA

June, 2019
İZMİR

DETERMINATION OF MECHANICAL PROPERTIES OF COMPOSITE MATERIALS REINFORCED BY MINERAL

A Thesis Submitted to the
Graduate School of Natural and Applied Sciences of Dokuz Eylül University
In Partial Fulfillment of the Requirements for the Degree of
Master Science in Mechanical Engineering, Mechanics Program

by

Dilek ATİLLA

June, 2019
İZMİR

M.Sc THESIS EXAMINATION RESULT FORM

We have read the thesis entitled **"DETERMINATION OF MECHANICAL PROPERTIES OF COMPOSITE MATERIALS REINFORCED BY MINERAL"** completed by **DİLEK ATİLLA** under supervision of **PROF.DR. BİNNUR GÖREN KIRAL** and we certify that in our opinion it is fully adequate, in scope and in quality, as a thesis for the degree of Master of Science.

Prof. Dr. Binnur GÖREN KIRAL

Supervisor

Prof. Dr. Güner E. Yeni

(Jury Member)

Doç. Dr. Sauli SAYER

(Jury Member)

Prof.Dr. Kadriye ERTEKİN

Director
Graduate School of Natural and Applied Sciences

ACKNOWLEDGEMENT

First of all, I would like to express my gratitude to my supervisor Prof. Dr. Binnur Gören KIRAL for lead the way when I get lost and shed light on when I fall the darkness, while this thesis come to exist from soup to nuts. Like what Sir Isaac Newton said “If I have seen further, it is by standing upon the shoulders of giants”, she raised me upward alltime. Fortunately, I met with her and embark on a journey which will not end.

I am grateful to Assist. Prof. Metin YURDDAŞKAL because of providing reinforcement minerals which are huntite and graphene.

I would like to thank to Prof. Dr. Ramazan KARAKUZU for allowing me to use devices and chemicals for produce specimens in Dokuz Eylül University Composite Laboratory and also thank to Res.Assist. Akar DOĞAN for helping me to use devices, produce specimens and make an experiment whenever I want.

Besides I am especially indebted to Prof. Dr. Zeki KIRAL and Res.Assist. Berkan HIZARCI for sharing experiment setup and knowledge for vibration experiment.

Lastly, I would like to give special thank my family, to encourage me throughout this experience and support my dream with love.

Dilek ATİLLA

DETERMINATION OF MECHANICAL PROPERTIES OF COMPOSITE MATERIALS REINFORCED BY MINERAL

ABSTRACT

In the present study, mechanical properties of composite materials reinforced by mineral were investigated. Mechanical properties of the composite specimens reinforced by minerals were determined experimentally and numerically for different weight ratios of mineral particles. Graphene and huntite minerals were added to epoxy resin to examine the effect of mineral types on the mechanical properties. In addition, the effect of non-layered huntite mineral unlike graphene, in nano-sized grain structure, was investigated. For these purposes, 0.5 weight percent , 1 weight percent and 3 weight percent graphene and huntite minerals were added to the epoxy and huntite-epoxy, graphene-epoxy, huntite-graphene-epoxy mineral reinforced samples were manufactured. Composite beams reinforced by the nano-sized minerals were examined numerically and experimentally for the determination of the mechanical properties. In the numerical analyses, the critical buckling load and free vibration response were obtained using ANSYS Mechanical APDL 17.0 finite element software. In addition, mechanical properties of composites specimens were examined by tensile test, dynamic mechanical analysis, free vibration test and buckling test.

Keywords: Graphene, huntite, composite materials reinforced by mineral, critical buckling load, dynamic mechanical analysis, vibration response, finite element method, experimental investigation

MİNERAL KATKILI KOMPOZİT MALZEMELERİN MEKANİK ÖZELLİKLERİNİN BELİRLENMESİ

ÖZ

Bu çalışmada, mineral katkılı kompozit malzemelerin mekanik özellikleri incelenmiştir. Mineral katkılı kompozit numunelerin mekanik özellikleri, mineral partiküllerin farklı ağırlık oranları için deneysel ve sayısal olarak belirlenmiştir. Mekanik cevap üzerinde mineral tipinin etkilerini incelemek için grafen ve huntit mineralleri epoksi reçineye eklenmiştir. Ayrıca, grafenden farklı olarak, tabaka halinde olmayan huntit mineralinin nano boyuttaki tanecik yapısındaki etkisi incelenmiştir. Bu amaçlarla, ağırlıkça yüzde 0,5, yüzde 1 ve yüzde 3 oranlarındaki grafen ve huntit mineralleri epoksiye eklenerek, huntit-epoksi, grafen-epoksi, huntit-grafen-epoksi, mineral katkılı numuneleri üretilmiştir. Nano boyut mineral katkılı kompozit kirişler mekanik özelliklerin tespiti için sayısal ve deneysel olarak incelenmiştir. Sayısal analizlerde, kritik burkulma yükü ve serbest titreşim cevabı ANSYS Mechanical APDL 17.0 sonlu elemanlar yazılımı kullanılarak belirlenmiştir. Ek olarak, kompozit numunelerin mekanik özellikleri çekme testi, dinamik mekanik analiz, serbest titreşim testi ve burkulma testi ile incelenmiştir.

Anahtar kelimeler: Grafen, huntit, mineral katkılı kompozit malzemeler, kritik burkulma yükü, dinamik mekanik analiz, titreşim cevabı, sonlu elemanlar yöntemi, deneysel inceleme

CONTENTS

Page

LIST OF FIGURES

Page

LIST OF TABLES

Page

CHAPTER ONE
INTRODUCTION

1.1 Composite Materials

Composite materials occur with at least two or more different materials which are combined in typically macroscopic level or nanometer-sized. Composite technology has advanced over the last few decades but this materials were used since ancient times. For example, adobe houses which are one of the first composite structures, consist of straw and mud (Gibson, 2011; Kaw, 2006; Mallick, 2008).

Composites run across various areas. Today, composites are used in aerospace, military and aircraft applications, manufacturing automotive parts, sporting goods, marine applications and infrastructures. The widespread use of composite materials is due to their superior properties such as high modulus, high strength in proportion to weight ratio, low density, higher hardness than other materials such as metals (Gibson, 2011; Kaw, 2006; Mallick, 2008).

1.1.1 Classification of Composite Materials

Composite materials are divided as reinforcing phase and matrix parts. The reinforcing materials may be in the form of fibers, particles or flakes. Matrix parts may be in the form of polymer, metal or ceramic (Gibson, 2011; Kaw, 2006; Mallick, 2008).

1.1.1.1 Reinforcing Phase

Particles reinforce: They contains of particles spread into matrices such as alloys and ceramics. They are usually isotropic because the particles are joined arbitrarily. They have high feature such as develop strength of second material, increased operating temperature, oxidation resistance, etc. Use of aluminum particles in rubber,

silicon carbide particles in aluminum, and gravel, sand, and cement to make concrete are given as example (Kaw, 2006).

Flake reinforce: They are flat reinforcements of composites. Typical flake materials are glass, mica, aluminum, and silver. Flake reinforces icrease out-of-plane flexural modulus, strength, and decrease cost. However, flakes cannot be oriented easily and materials of flake reinforce are limited for use (Kaw, 2006).

Fiber reinforce: Fiber reinforces that are added in matrix consist of short (discontinuous) or long (continuous) fibers. Fibers are generally anisotropic and carbon, glass and aramids are given as an example. In addition, resins such as epoxy, metals such as aluminum, and ceramics such as calcium–alumino silicate are examples of different types of matrices. The fundamental units of continuous fiber matrix composite are unidirectional or woven fiber laminas. Laminas are stacked on top of each other at various angles to form a multidirectional laminate (Kaw, 2006).

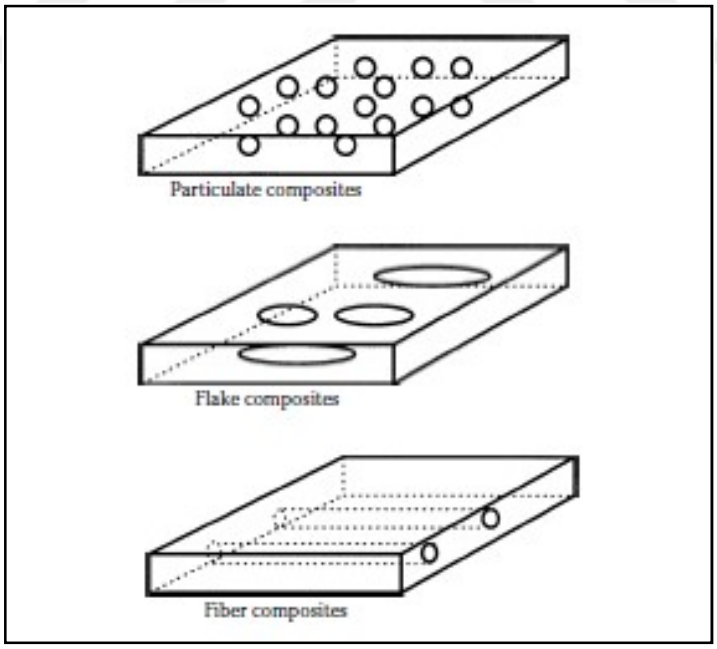

Figure 1.1 Types of composites based on reinforcement shape (Kaw, 2006)

1.1.1.2 Matrix Phase

Polymer matrix: A polymer consists of long-chain molecules interconnected by strong covalent bonds. A polymeric material is a gathering of a large number of polymer molecules of corresponding chemical structure (Mallick, 2008).

Polymers are categorized into two main heading which are thermoplastics and thermosets. In a thermoplastic polymer, molecules are not chemically joined together. They are linked each other with weak secondary bonds or intermolecular forces, like van der Waals bonds and hydrogen bonds. This weak molecular bonds broke if the polymer is heated. Conversely, broken bonds are restored when the liquid thermoplastic polymer is cooled. So, a thermoplastic polymer can be heat-softened, melted, and reshaped (Mallick, 2008).

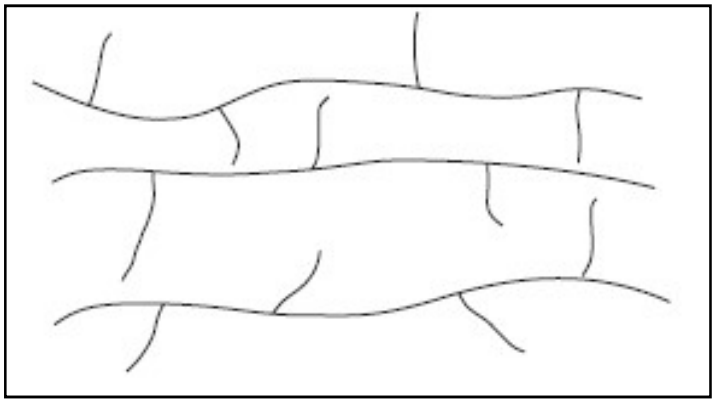

Figure 1.2 Bonds of thermoplastic polymer (Mallick, 2008)

In a thermoset polymer, however, the molecules are chemically bonded together by strong, cross-links, forming a rigid, three-dimensional network structure. These bonds occur during the polymerization reaction or the curing reaction. The bonds are not broken when the liquid thermoset polymer is heated so the thermoset polymer cannot be melted, and reshaped. However, if the number of crosslinks is low, it may be possible to soften them at high temperatures (Mallick, 2008).

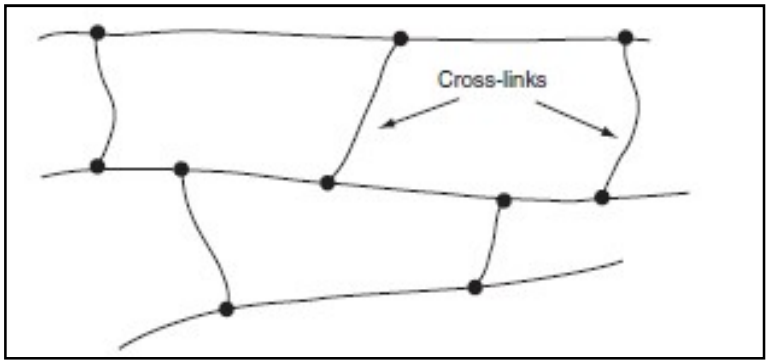

Figure 1.3 Bonds of thermoset polymer (Mallick, 2008)

Metal matrix: Metal matrix has the numerous advantage compare with polymeric matrix. For example, most metals has higher yield strength than most polymer matrices. A further advantage of using metal is that it can be formed and strengthened by various thermal and mechanical processes. But metals have high density, high melting point, corrosion and etc. Aluminum and its alloys are used mostly as matrix material in metal matrix composites because of good corrosion resistance. Carbon fiber is used with aluminum alloys; however, at typical fabrication temperatures of 5008ºC or higher, carbon reacts with aluminum to form aluminum carbide (Al_4C_3), which severely degrades the mechanical properties of the composite (Mallick, 2008).

Ceramic matrix: Ceramics are prefered at high temperature where desired because of their high properties such as temperature stability, thermal shock resistance, high modulus, high hardness, corrosion resistance, and low density. However, they are brittle materials and possess low fracture toughness and low resistance to crack propagation. The reason that adding reinforced materials in ceramic matrix increase fracture toughness of composites. Alumina (Al_2O_3) and mullite (Al_2O_3–SiO_2) are the two most commonly used ceramics (Mallick, 2008).

1.2.1 Manufacture Methods of Composite Materials

1.2.1.1 Prepreg Lay Up Process

This manufacturing process is called the autoclave processing or vacuum bagging process. It is suitable for the production of complex shapes and very widespread in production, especially in the aerospace industry (Bratukhin & Bogolyubov, 1995; Gay & Hoa, 2003; Mazumdar, 2002).

In this process, prepregs or resin impregnated fabrics are cut and laid down on the mold. After vacuum bagging, the composite with the mold exposed to heat and pressure for curing and solidify (Bratukhin & Bogolyubov, 1995; Gay & Hoa, 2003; Mazumdar, 2002).

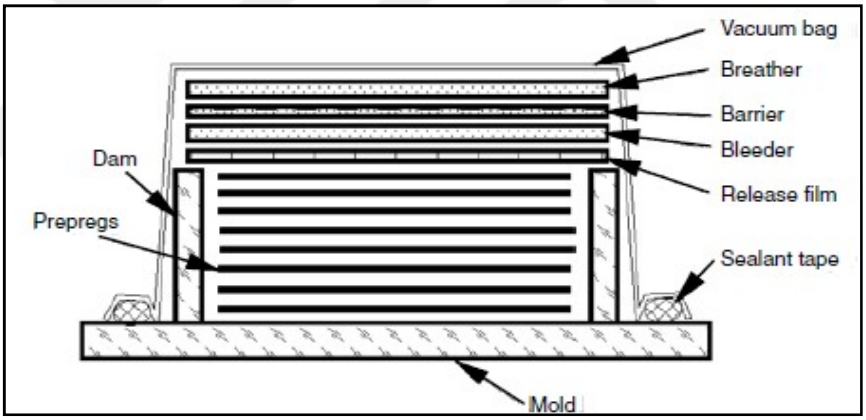

Figure 1.4 Vacuum bagging for prepreg lay-up process (Mazumdar, 2002)

1.2.1.2 Wet Lay Up Process

In this process, liquid resin and fabrics are applied to the mold with a room temperature at cure environment and low pressures. A roller is used to compress excessive resin and impregnated with resin by fabric to provide uniform distribution and wetting. This method allows the production of different composites by placing different types of fabric materials manually. It is also called the hand lay-up process (Bratukhin & Bogolyubov, 1995; Gay & Hoa, 2003; Mazumdar, 2002).

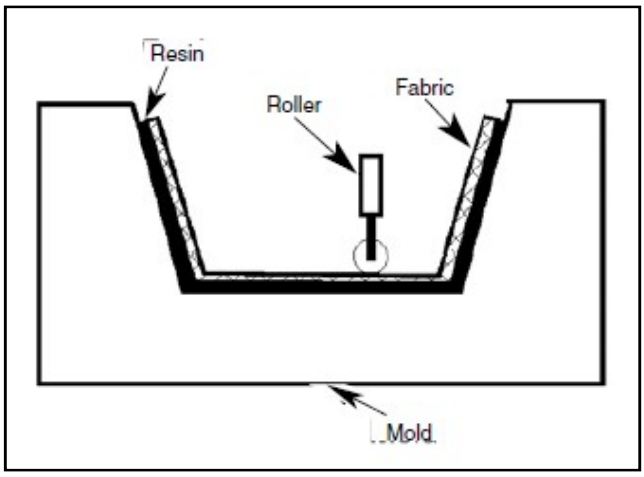

Figure 1.5 Wet lay-up process (Mazumdar, 2002)

1.2.1.3 Spray-Up Process Process

The spray-up process is similar with the wet lay-up process. In this method, a spray gun is used to deliver mix of resin and chopped fiber reinforcements, which is situated in tube, onto the mold manually. The gun cuts continuous fiber with intended length and passes it through a resin then spray onto the mold. The spray-up process is much faster and less expensive than the wet lay-up process (Bratukhin & Bogolyubov, 1995; Gay & Hoa, 2003; Mazumdar, 2002).

Figure 1.6 Spray-up process (Mazumdar, 2002)

1.2.1.4 Filament Winding Process

Resin impregnated fibers are wrapped over a rotating mandrel at the desired angle. In filament winding process, carriage unit which carry resin impregnated fibers moves throughout guide rail. At the same time mandrel rotates at a constant speed. So, with adjusting carriage unit and mandrel speed, the desired fiber angle is provided and cylindrical or tubuler parts are obtained (Bratukhin & Bogolyubov, 1995; Gay & Hoa, 2003; Mazumdar, 2002).

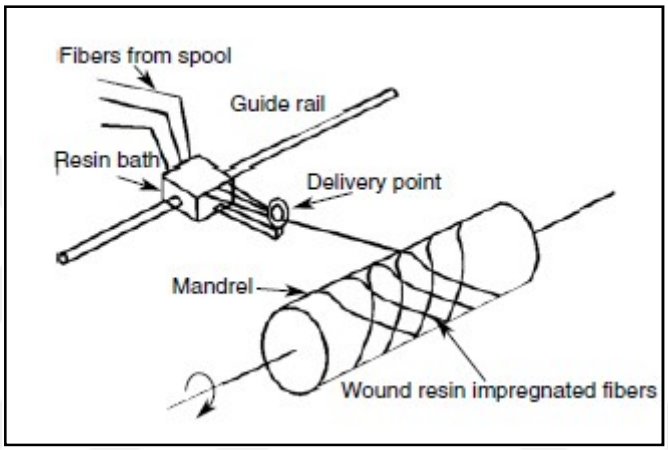

Figure 1.7 Filament winding process (Mazumdar, 2002)

1.2.1.5 Pultrusion Process

Pultrusion is used to manufacture of solid and hollow structures with constant cross-sections like beams, channels and tubes. In this process, reinforcements are passed through an open resin bath and coated with resin. Then, reinforcements impregnated with resin are passed through a heated die. Thanks to the heated die, curing start and continue throughout the die length. Last of operation, manufactured composite is cut off desired length (Bratukhin & Bogolyubov, 1995; Gay & Hoa, 2003; Mazumdar, 2002).

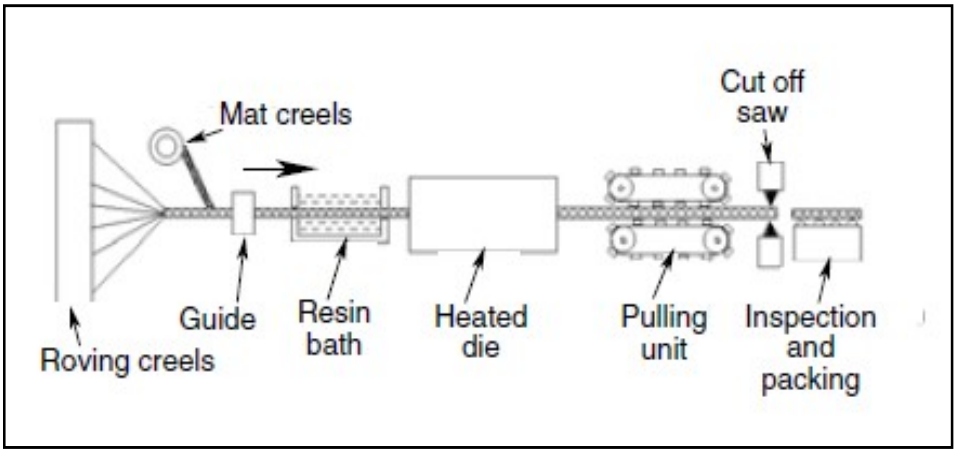

Figure 1.8 Pultrusion process (Mazumdar, 2002)

1.2.1.6 Resin Transfer Molding Process

Resin Transfer Molding (RTM) process is a process that is a closed mold operation. Firstly, dry fiber preform is laid out on the mold and second mold is closed on the mold and preform. Then, thermoset resin is pumped into the mold at a constant pressure. After exothermic curing, mold is opened and manufactured part is removed (Bratukhin & Bogolyubov, 1995; Gay & Hoa, 2003; Mazumdar, 2002).

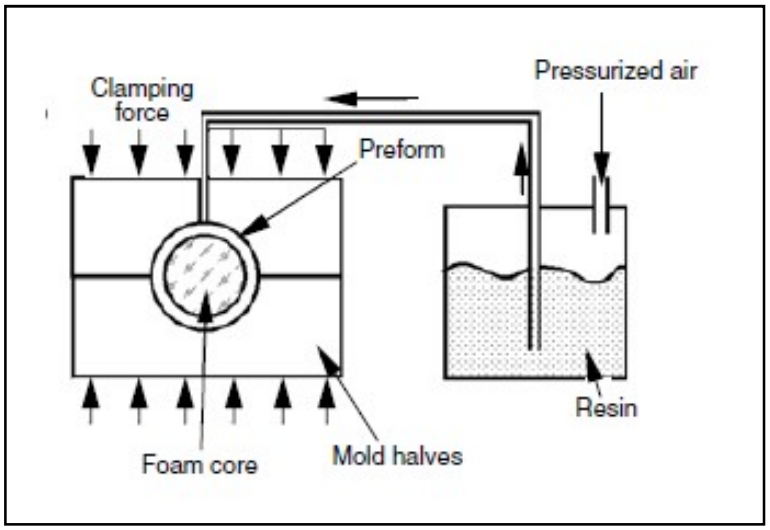

Figure 1.9 Resin transfer molding process (Mazumdar, 2002)

1.2.1.7 Compression Molding Process

In compression molding process, the molds are preheated to about 140°C. Sheet molding compounds which are called charge, are placed middle of the mold. When the mold is closed, the charge fills the cavity of the mold. Using heat and pressure cause curing of the composite. After the curing process the mold is opened and the part is removed from the mold (Bratukhin & Bogolyubov, 1995; Gay & Hoa, 2003; Mazumdar, 2002).

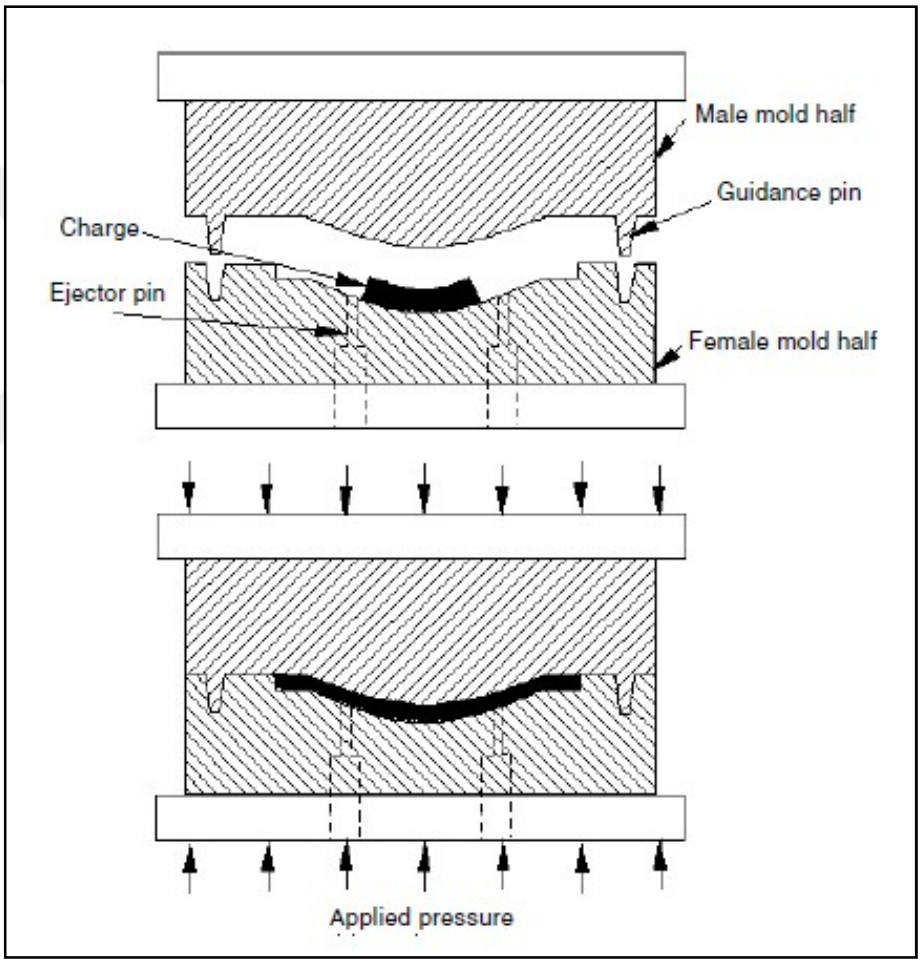

Figure 1.10 Compression molding process (Mazumdar, 2002)

1.2.1.8 Roll Wrapping Process

In the roll wrapping process, the prepreg sheet is cut rectangular or trapezoidal shapes with the help of an automatic prepreg cutter. Prepreg plies are stacked together. Then, the mandrel is placed over the prepreg layers at a specific angle and then rolled carefully. While rolling, pressure is applied at the rolling table to obtain good prepreg and mandrel contact as well as good interlayer contact (Bratukhin & Bogolyubov, 1995; Gay & Hoa, 2003; Mazumdar, 2002).

1.2.1.9 Injection Molding Process

In injection molding process, the reinforcements (mats, fabrics) are filled between the mold and countermold. The polyester or phenolic resin is injected. The mold pressure is low. It has application in automobile bodies (Bratukhin & Bogolyubov, 1995; Gay & Hoa, 2003; Mazumdar, 2002).

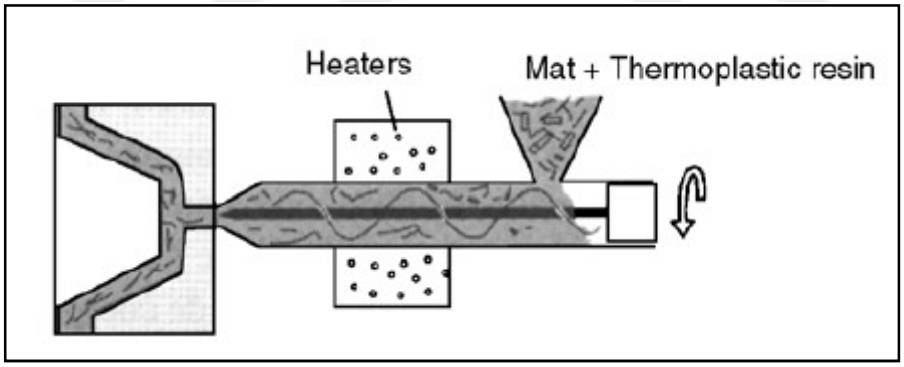

Figure 1.11 Injection molding process (Gay, 2003)

CHAPTER TWO
MINERALS

2.1 Carbon and Allotropes

Carbon is one of the most abundant elements on Earth. In addition that, due to the superior properties such as lower density than metallic materials, higher thermal conductivities, high stiffness, low coefficient of thermal expansions, strong for its very low weight, this make it and its allotropes preferable materials in fields of industries (Tong, 2011).

Carbon atoms come together with the different sequence of atoms. This new form of atoms which are named as allotropes may have private material properties. For instances, allotropes of diamond, graphite, fullerene, and nanotube, creating materials with very different properties and shapes (Tong, 2011).

2.1.1 Diamond

It is a meta-stable allotrope of carbon with the carbon atoms arranged in a face-centred cubic crystal structure given in Figure 1.4 (Karthik, Himaja, & Singh, 2014). Diamond has combination of physical, optical, and thermal properties and these make it proper material for many applications. It provide ultrahigh thermal conductivity, high strength and wear resistant. Therefore, it uses for electrically insulating, thermal management of electronic packaging, small-scale chip cooling applications, manufacuring composite structures (Tong, 2011).

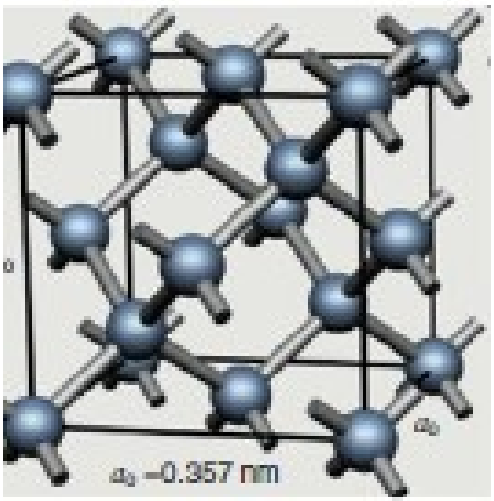

Figure 2.1 Diamond molecule (Tong, 2011)

2.1.2 Fullerene

A fullerene is a convex closed cage molecule formed out of only carbon atoms to form the shape of hexagonal and pentagonal faces (Yakobson, & Smalley, 1997). Fullerene which is an enclosed spherical structure with hexagonal and pentagonal rings are named also bucky ballswhich shown in Figure 1.5 (Karthik et al., 2014).

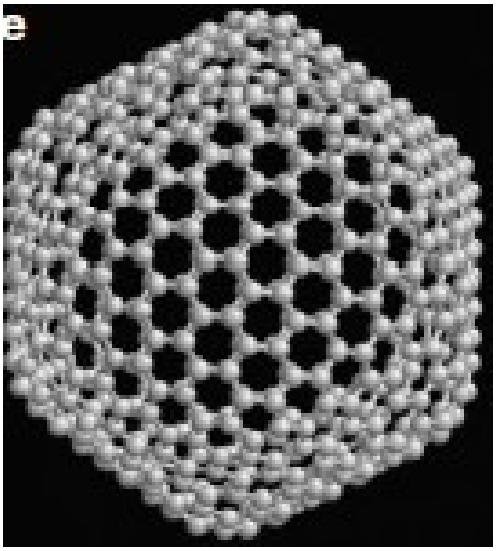

Figure 2.2 Fullerene molecule (Tong, 2011)

2.1.3 Carbon nano tube (CNT):

Carbon nano tube is a cylindrical structure consist of graphene sheet in one atom thick. While single walled nanotubes (SWNT) are formed by rolled up a single sheet of graphene, multi-walled nanotubes (MWNT) are formed by concentrically rolled up sheets of graphene shown in Figure 2.3 (Karthik et al., 2014).

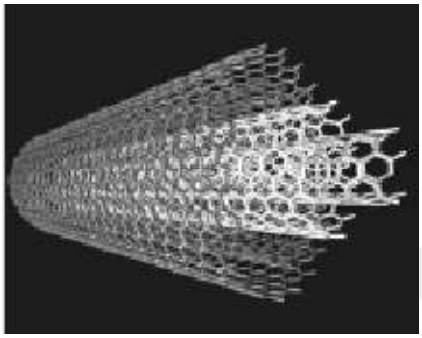

Figure 2.3 Multi-walled carbon nano tube (Tong, 2011)

2.1.4 Graphite:

Graphite was named by a German geologist Abraham Gottlob Werner in 1789. It is a planar layers structure of carbon atoms in a honeycomb mesh structure. Each layer is stand together with the help of weakly unsaturated π-bond. Each layer of graphite consists of two-dimensional graphene molecules (Karthik et al., 2014).

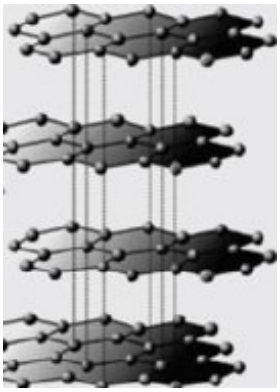

Figure 2.4 Graphite (Tong, 2011)

2.1.5 Graphene

Professors Andre Geim and Konstantin Novoselov were awarded at the 2010 Nobel Prize in physic field for their extraordinary and ground-breaking discovery on graphene. They were started a new age with their pioneering work on a single atomic layer of carbon, graphene which is two-dimensional atomic crystals, in the material fields (Hancock, 2011).

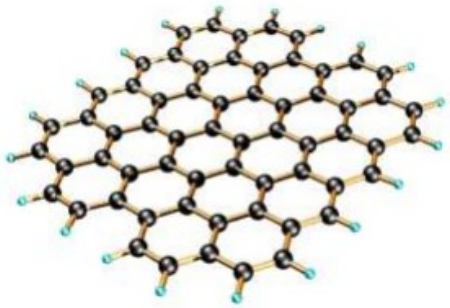

Figure 2.5 Single graphene sheet (Radadiva, 2015)

Graphene consists of one thin layer pure carbon and thickness of graphene is one atom. The reason being ground-breaking discovery of graphene that it is 100 times stronger than steel is very light, flexible and the strongest material ever discovered. Also, it conducts heat and electricity with great efficiency. Due to their two dimensional structures and very thin diameter, it can be used various area like as a sensor device, semiconductor or used for components of integrated circuits. The reported properties and applications of graphene may be opened up new opportunities for the future devices and systems (Radadiva, 2015).

Therefore, nowadays there are increasing interest for graphene and its effects are investigated in all respects especially onto the composite materials (D'Aloia & et al., 2018; He & et al., 2019).

The effect of the dispersion of the graphene into the epoxy resin was investigated. Thermally reduced graphite oxide sheets (RGO) were added into epoxy with

different ratios and various mechanical properties were determined using dynamic mechanical analysis, tensile, flexural and fracture test etc. Highly disperced RGO resulted in high stress and fracture toughness value. In addition highly disperced RGO increased Tg value according to low disperced RGO (Tang & et al., 2013).

Additionally, effects of graphene oxide and epoxy coated glass fiber composites were compared with uncoated ones (Mahmood, Vanzetti, Bersani & Pegoretti, 2018).

Comparision of graphene – epoxy composites and CNT – epoxy composites were studied according to mecanical properties. It was obtained that graphene was superior to CNT according to Young's module, tensile strength and crack energy (Li, Wang, Wang & Xing, 2018).

In addition, investigation of mechanical properties, electrical conductivity of graphene – epoxy composites were compared with CNT – epoxy composites (Govorov, Wentzel, Miller, Kanaan & Sevostianov, 2018).

Also, thermal conductivity and electrical insulation were studied with the added of graphene in the SiC nanowires (He & et al., 2019).

One of the different studies on graphene is researching of both shape memory effect and mechanical properties with utilizing tensile test, dynamic mechanical analysis and fold deploy shape memory test according to different mass fraction (Zhao, Feng, Li & Mi, 2014).

However, in generally, this investigations handle the behaviour of graphene oxide in literature (Jamali, Khosravi, Rezvani & Tohidlou, 2019; Haeri, Asghari & Ramezanzadeh, 2017). Namely, study of thermoset polymer composites reinforced by graphene is inadequate. In this thesis, it is aimed to examine the graphene effect in terms of mechanical properties in epoxy and to bring it into literature.

2.2 Huntite

Huntite is a calcium magnesium carbonate mineral with molecular weight and density are 353.03 gr and 2.696 g/cm^3 (at 4 ºC), respectively. Chemical formula of huntite is $CaMg_3(CO_3)_4$, (%15.88 CaO, %34.25 MgO ve %49.87 CO_2). Huntite is found together with mostly hydromanyesite or magnesite. It has a pure white appearance (Yücel & Gül, 2017).

Huntite was first discovered by Faust (1953) in carbonated volcanic tuffs in Currant Creek, Nevada, USA. It was accepted that huntite occurred thanks to react magnesite and dolomite with meteoric waters at the time. Huntite mineral; was named after The American mineralogist Walter Frederick Hunt (1882-1975) (Yücel & Gül, 2017).

Huntite is widely used in flame retardant as plastic, polymer, rubber, paint etc. is a source of raw materials for the sectors. The result of endothermic reaction; absorbs heat, reduces flame and surface temperatures. It also dilutes all kinds of fumes and combustible gases (Kaya, 1998; Yücel & Gül, 2017).

Huntite decomposes endothermically releasing carbon dioxide over a temperature range of approximately 450°C to 800°C (Hollingbery & Hull, 2010).

$$Mg_3Ca(CO_3)_4 \rightarrow 3MgO + CaO + 4CO_2 \qquad (2.1)$$

The flame retardant feature is prominent; flame retardants reduce the flammability of materials. It reduces the risk of fire and reduces the risk of fire spread. With these properties, it increases the time of the escape from the fire and reduces the loss of life and injuries, while also preventing serious financial losses and negative environmental effects (Yücel & Gül, 2017).

Due to the positive effects of huntite minerals, different materials are investigated reinforced by huntite mineral in literature.

Nano-sized huntite / hydromanyesite mineral is added to the paint materials in different ratios. Flame retardant properties and mechanical properties of the coating materials are investigated. Flame retardant and mechanical properties were developed with adding mineral (Yıldırım & Çelik, 2014).

In general, owing to low thermal properties, polimer matrix used with flame retardant minerals. So, huntite is added into the poly(ethylene-*co*-vinyl acetate)(EVA) resin with different ratios and different sizes for investigation of mineral effect (Atay & Çelik, 2013).

Similarly, huntite hydromagnesite mineral is added into polipropilen matrix to describe mechanic properties of composite structure (Kanbur & Tayfun, 2017).

Additonally, huntite mineral was used in different weight ratios to determine the thermal and mechanical properties of huntite on polyester matrix. In that reason, various experiments like tensile test, three point bending test, thermogravimetric analysis were applied (Seki, Sever, Sarikanat, Sakarya & Elik, 2013).

In other matrix to improve thermal properties of composite with adding huntite / hydromagnesite mineral was polyethylene terephthalate (PET). For determination of thermal properties whether improve or not, pure PET and huntite added PET were compared. Huntite added PET composite was demostrated beter thermal stabilities than pure PET (Baştürk, Madakbaş, Karadoğan & Kahraman, 2016).

In literature, there are different studies that investigate matrix materials with reinforced by huntite but the investigation of most used thermoset resin, epoxy, is rare (Lee & Neville, 1967). In that reason, huntite and nano size huntite effect on resin with different weight ratios were investigated and mechanical properties of composites were determined.

CHAPTER THREE
PREPARATION OF THE SPECIMENS

3.1 Mold Design and Production

In this study, diverse mold shapes were designed and manufactured according to proper experiment standards so as to form the epoxy resin and mineral mixture that was in liquid state before curing. In this reason, three types of molds were used for forming mixture of epoxy resin and mineral at curing time.

Mold 1 shown in Figure 3.1 was manufactured from aluminum plate with milling operation. There are three cavities with two different sizes on the mold. The small cavity which has 20 x 4 x 0.3 cm^3 dimensions was designed to determine Poisson's ratio and modulus of elasticity using the strain gauge. These mechanical properties were used as inputs in the numerical analyses by ANSYS Mechanical APDL 17.0 finite element software. The other ones which have 25 x 5 x 0.3 cm^3 dimension were designed for vibration and buckling tests to determine the natural frequency, damping ratio and the critical buckling loads of the specimens, respectively.

Figure 3.1 Mold 1, aluminum mold (Personal archive, 2018)

Mold 2 shown in Figure 3.2 was designed according to ASTM D3039 tensile test standard using SolidWorks 2017 software. It was manufactured with additive manufacturing method using 3D printer. Mold 2 was made of ABS material whose melting point is higher than the curing temperature which was 80°C. It means that, mold was not deform and protect the first form on curing time. This mold has 175 x 230 x 5.5 mm^3 dimension and three tensile specimens can be obtained.

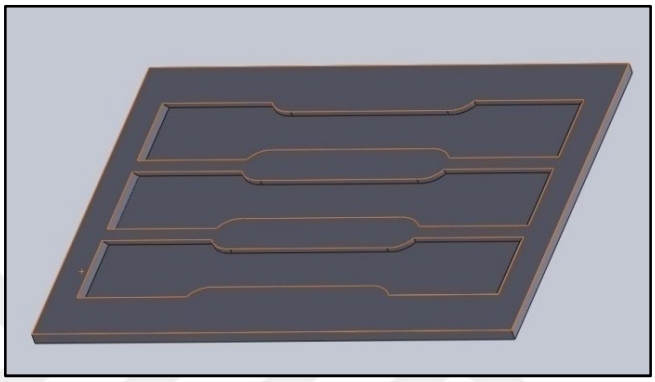

Figure 3.2 Mold 2, ABS mold (Personal archive, 2018)

Mold 3 shown in Figure 3.3 was produced from aluminum material. It has 120 mm outer diameter, 100 mm interior hole diameter and 2 mm dept. 45° radius was added to the inner diameter for effortless separation of the produced specimens. They were used to manufacture specimens to be used in the dynamic mechanical analysis.

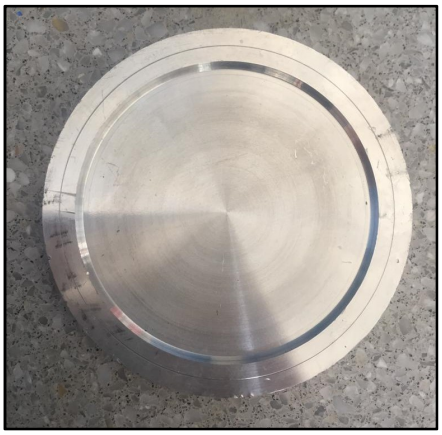

Figure 3.3 Mold 3, circular aluminum mold (Personal archive, 2018)

Initially, the mixture of epoxy resin and mineral is liquid before pouring into molds. When temperature increases from room temperature to curing temperature, the mixture starts to become solid in the molds. To prevent the mixture from adhering to the mold as it passes from liquid state to solid state, all molds were coated with the self-adhesive teflon fabric which was supplied from Manisa Endüstri, shown in Figure 3.4. Thus, contact between mixture of epoxy resin and mold was prevented.

Figure 3.4 Coated molds with the self-adhesive teflon fabric (Personal archive, 2018)

3.2 Adjustment of Mineral Particle Size

In this study, graphene and huntite minerals having different weight ratios were added into epoxy resin to examine the effect on mechanical properties of the composite specimens. In addition, the effect of non-layered huntite mineral unlike graphene, in nano-sized grain structure, was investigated. For these purposes, the grain size of the huntite mineral was decreased to nano dimensions with Fritsch Planetary Micro Mill PULVERISETTE 7 machine which is shown in Figure 3.5. The machine is used for grinding down to materials with the thanks to grinding balls.

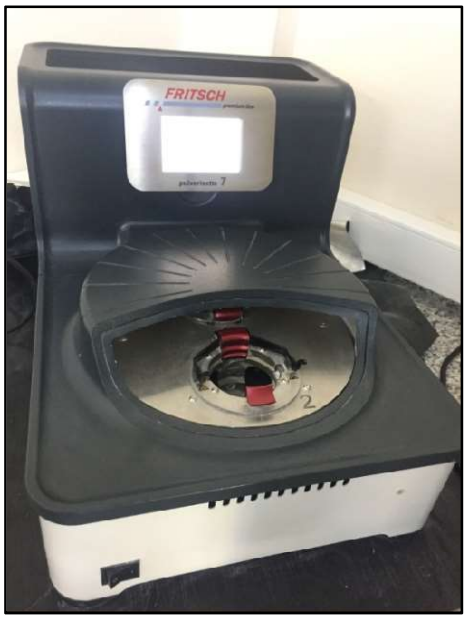

Figure 3.5 Fritsch planetary micro mill pulverisette 7 machine (Personal archive, 2018)

Grinding balls, huntite mineral and Tekkim stearic acid used for lubricant agent to prevention of dust adhesion were added in the grinding bowl of the machine. Then the bowl was rotated around its own axis and machine's main disk in the opposite direction at 300 rpm speed for 20 minutes. Due to the centrifugal force and friction force between grinding balls and the inner wall of the grinding bowl, the mineral in the grinding bowl with aid of the grinding balls, was reduced to the desired nanometer dimensions.

3.3 Preparation of Mixture of Epoxy Resin and Mineral

Graphene, huntite, nano sized huntite and mix of huntite-graphene were added into epoxy resin with different weight ratios of 0.5 wt%, 1 wt% and 3 wt% to identify effects of the mineral on the mechanical properties. Huntsman Araldite LY 1564 SP and Fibermak F3484 were chosen properly each other as epoxy resin and curing agent respectively. Epoxy resin and curing agent were mixed consisdering the weight ratio of 1:3 according to epoxy resin and curing agent catalog.

According to weight ratios associated with the mass of the epoxy resin and curing agent, minerals measurements were carried out with Kern precision scales for each mineral as shown in Figure 3.6.

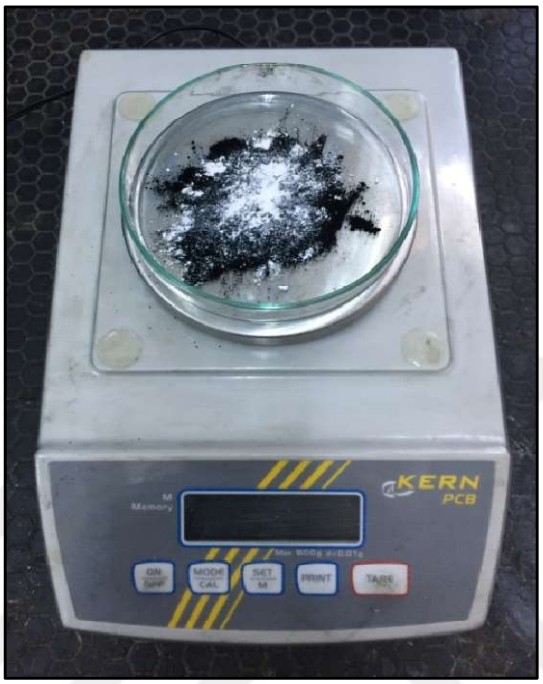

Figure 3.6 Measurement of mineral weight with precision scale (Personal archive, 2018)

In order to obtain homogeneous distribution of mineral and prevent clumping of the mineral into the epoxy resin, mechanical mixing and magnetic stirrer were employed. Firstly, epoxy resin was poured into the 250 ml beaker and measured mineral was added into the epoxy resin. Then, mixture was stirred both mechanically with spatula during 5 minutes and magnetically with magnetic stirrer machine in 15 minutes with the small aid of magnet as shown in Figure 3.7 and Figure 3.8. The speed of the magnetic stirrer machine was started 350 rpm and increased up to 1500 rpm gradually.

At the end of the stirring, curing agent was added into the mix of epoxy resin and mineral on the magnetic stirrer machine. For good dispersion, final mix which consists of epoxy resin, curing agent and mineral, was stirred with magnetic stirrer machine during 10 minutes from 350 rpm to 1500 rpm, additionally.

Figure 3.7 Magnetic stirrer machine's magnet (Personal archive, 2018)

Figure 3.8 Magnetic stirrer machine and mixing epoxy resin and mineral (Personal archive, 2018)

Finally, mixture was poured into the self-adhesive teflon fabric coated molds. Then, the molds were placed into the JSR brand JSOF-050 Forced convection oven in Dokuz Eylül University, Mechanical Engineering Department, Composite Laboratory. The oven shown in Figure 3.9 was set at 80°C for 4 hours for curing and solidifying the specimens shown in Figure 3.10. So, to investigate huntite, nano size

huntite, graphene and huntite-graphene effect and the effects of these minerals' mass-to-mixture ratio on epoxy resin, specimens were created to use on the experimental analysis. All operations that are described above were repeated for each parameter.

Figure 3.9 JSR brand JSOF-050 forced convection oven (Personal archive, 2018)

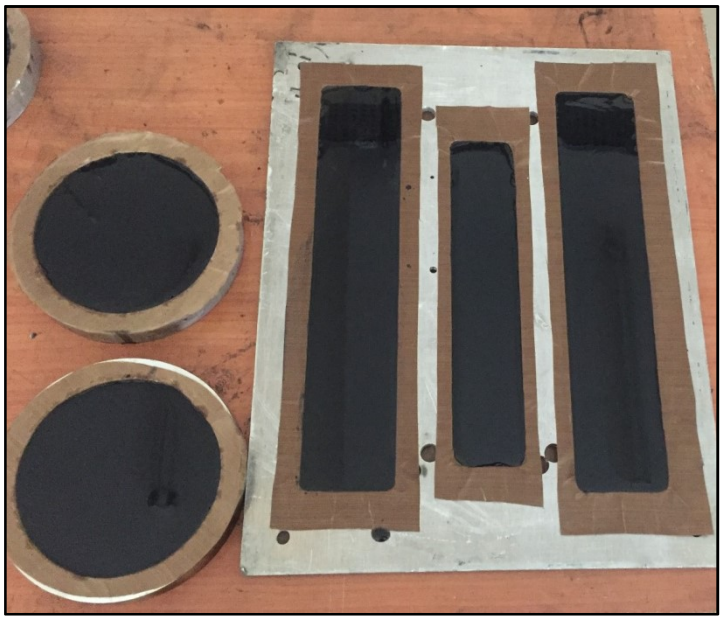

Figure 3.10 Mixture of the epoxy resin-graphene in the mold 1 and mold 3 (Personal archive, 2018)

3.4 Nomenclature of Specimens

Specimens were demonstrated with codes so that it can be easily expressed. There were four different mineral types and three weight ratios. With the adding pure resin, totally thirteen parameters were examined. As shown in Table 3.1 and Figure 3.11, pure resin, huntite, graphene, huntite nano sized and mixture of huntite and graphene were named as Rc, H, G, Hn and HG, respectively. In addition, the numbers next to the letters were expressed the weight ratios of mineral in the resin. For example, G05 represents graphene mineral with 0.5% weight ratio added into the resin.

Table 3.1 Demonstration of the codes in accordance with percent weight ratio and reinforced minerals

	wt%	0.5 wt%	1 wt%	3 wt%
Pure resin	Rc			
Huntite	H05	x		
	H1		x	
	H3			x
Graphene	G05	x		
	G1		x	
	G3			x
Huntite nano size	Hn05	x		
	Hn1		x	
	Hn3			x
Huntite and Graphene mixture	HG05	x		
	HG1		x	
	HG3			x

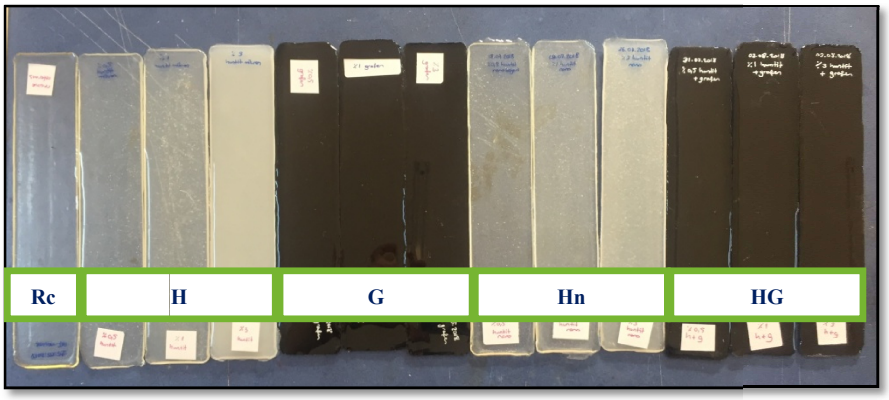

Figure 3.11 Nomenclature of specimens (Personal archive, 2018)

CHAPTER FOUR

TENSILE TEST AND DETERMINATION OF THE POISSON'S RATIO

4.1 Insertion of The Strain Gauge

Strain gauge is a sensor that converts the amount of deformation occurred in the unit length to electrical resistance when the load is applied on the specimen. The deformation values are provided by means of the gauge indicator. Indicators are used as four strain gauge elements that are electrically connected in the form of a Wheatstone Bridge circuit shown in Figure 4.1.

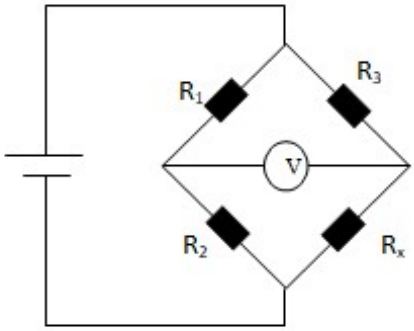

Figure 4.1 Wheatstone bridge circuit

In this experiment, Quarter Wheatstone Bridge type was used. Because, single strain gauge was placed in replace for R_x resistance for measuring voltage in that axis. Thus, longitudinal strain was measured with the strain gauge parallel to the lengthwise axis and lateral strain was measured with the second strain gauge perpendicular to the that axis. Therefore, two strain gauges were used perpendicular to one another, provided that one was along the longitudinal axis as shown in the Figure 4.2. So Poisson's ratio was calculated using these strain values given below as

$$\nu = -\frac{\varepsilon_{lateral}}{\varepsilon_{longitudinal}} \tag{4.1}$$

where ν and ε are Poisson's ratio and strain values, respectively.

Strain gauges were bonded onto the specimens with the help of adhesive. The specimen surface was roughened with sandpaper for good adhesion. Then, strain gauges were placed to the determine the Poisson's ratios.

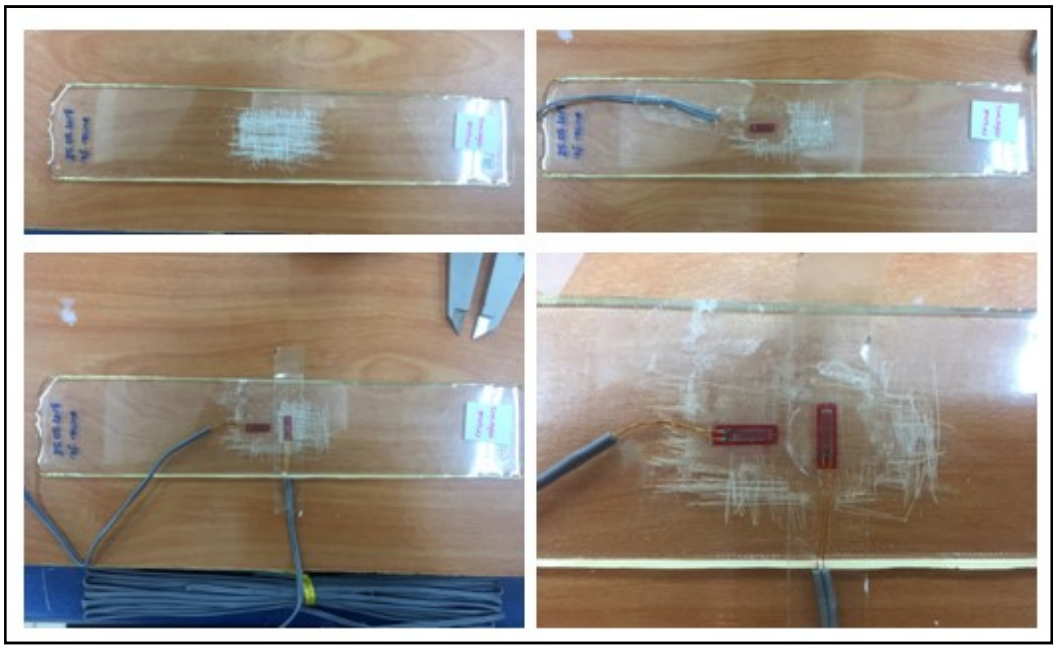

Figure 4.2 Bonding of the strain gauge on the specimens (Personal archive, 2018)

Strain gauge has a sensitivity factor that is called gauge factor (GF) determined by the manufacturer. It provides conformity between deformation and resistance. Gauge factor is given below formula (4.2) :

$$GF = \frac{\Delta R/R}{\varepsilon} \tag{4.2}$$

GF: Gage factor

ΔR: Change of resistance [Ω]

R: Resistance of strain gauge before deformation [Ω]

ε: Strain value [mm/mm]

The gauge factor is an important parameter for converting the resistance to the strain value. In this experiment, general use foil type TML FLA-5-11 strain gauge was used. Its gauge factor is 2.11, shown at data sheet in Figure 4.3. This value was given as an input into the indicator program.

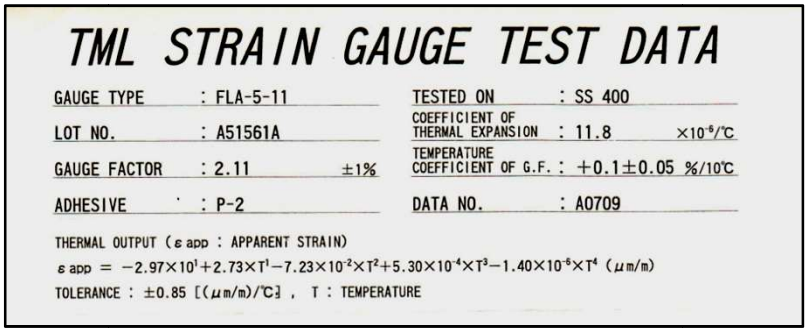

TML STRAIN GAUGE TEST DATA

GAUGE TYPE	: FLA-5-11	TESTED ON	: SS 400
LOT NO.	: A51561A	COEFFICIENT OF THERMAL EXPANSION	: 11.8 ×10⁻⁶/℃
GAUGE FACTOR	: 2.11 ±1%	TEMPERATURE COEFFICIENT OF G.F.	: +0.1±0.05 %/10℃
ADHESIVE	: P-2	DATA NO.	: A0709

THERMAL OUTPUT (ε app : APPARENT STRAIN)

$\varepsilon_{app} = -2.97\times10^{1}+2.73\times T^{1}-7.23\times10^{-2}\times T^{2}+5.30\times10^{-4}\times T^{3}-1.40\times10^{-6}\times T^{4}$ (μm/m)

TOLERANCE : ±0.85 [(μm/m)/℃] , T : TEMPERATURE

Figure 4.3 Data sheet of strain gauge (Personal archive, 2018)

Lateral and axial strain values were read from two different measurement screens via Tokyo Seiki Data Logger TDS-530 indicator and switching box shown in Figure 4.4 and Figure 4.5.

Figure 4.4 Strain gauge indicator (Personal archive, 2018)

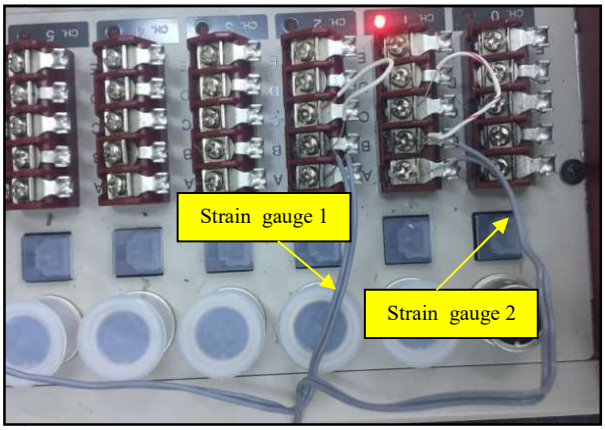

Figure 4.5 Connecting the strain gauges to the switching box (Personal archive, 2018)

4.2 Poisson's Ratio and Modulus of Elasticity

Tensile test was applied to determine the modulus of elasticity at a constant speed of 0.5 mm/min up to the yield point. Stress – strain graphs can be seen in the figures from Figure 4.6 to Figure 4.18.

Modulus of elasticity and Poisson's ratio values were determined thanks to equation of graphs from Figure 4.6 to Figure 4.18 were calculated as linear equation. From these equations, modulus of the elasticity values were obtained with slope of the stress – strain graphs and Poisson's ratios were obtained with slope of lateral – longitudinal strain values. They were given in Table 4.1.

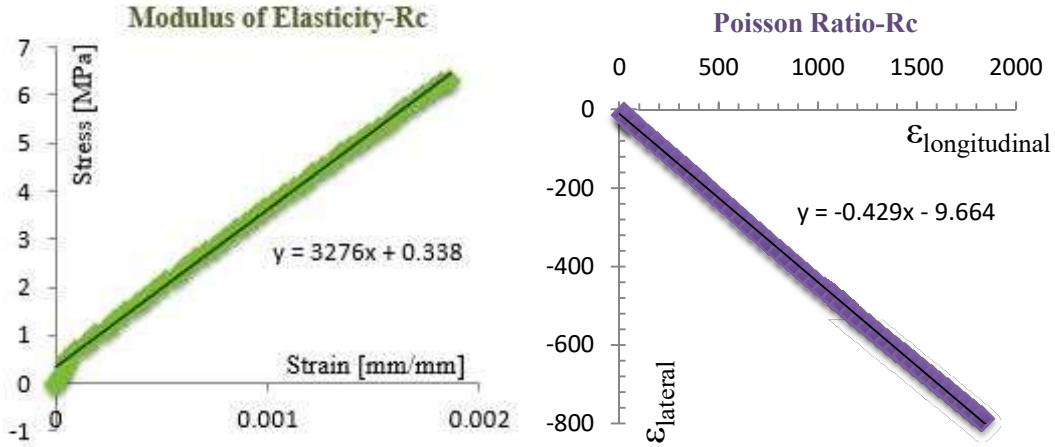

Figure 4.6 Modulus of elasticity and Poisson's ratio value of Rc specimen

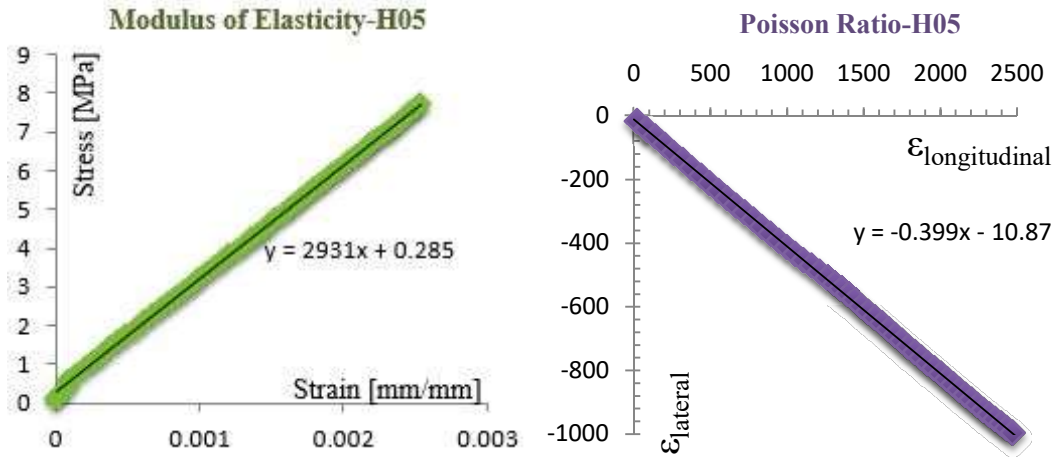

Figure 4.7 Modulus of elasticity and Poisson's ratio value of H05 specimen

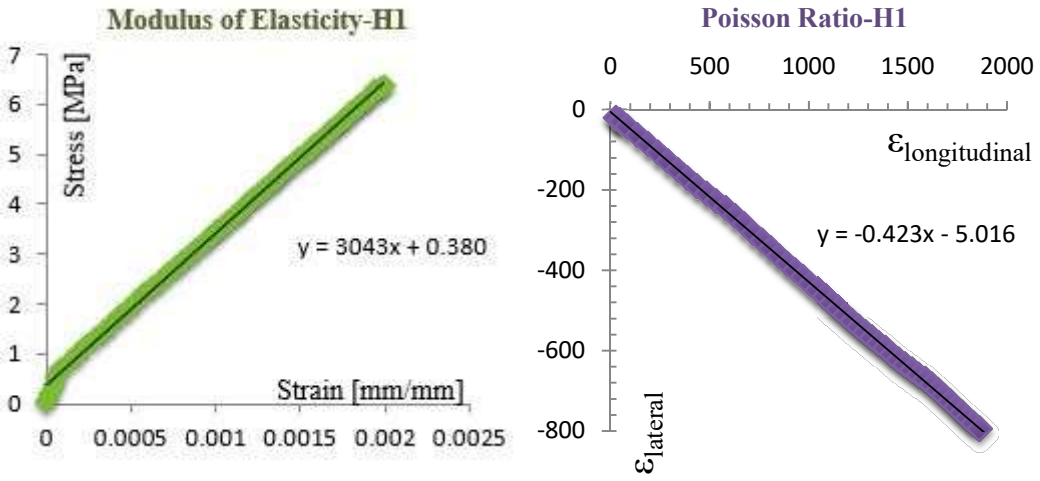

Figure 4.8 Modulus of elasticity and Poisson's ratio value of H1 specimen

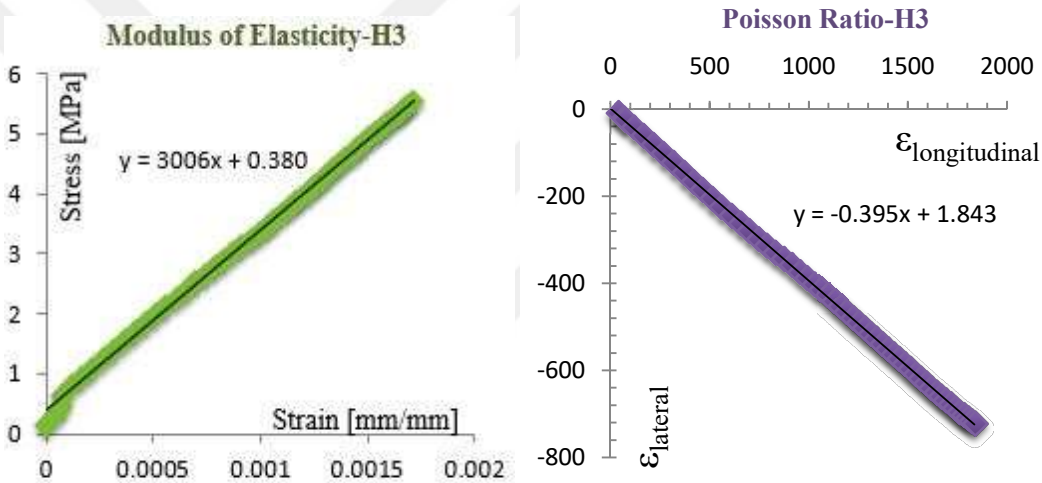

Figure 4.9 Modulus of elasticity and Poisson's ratio value of H3 specimen

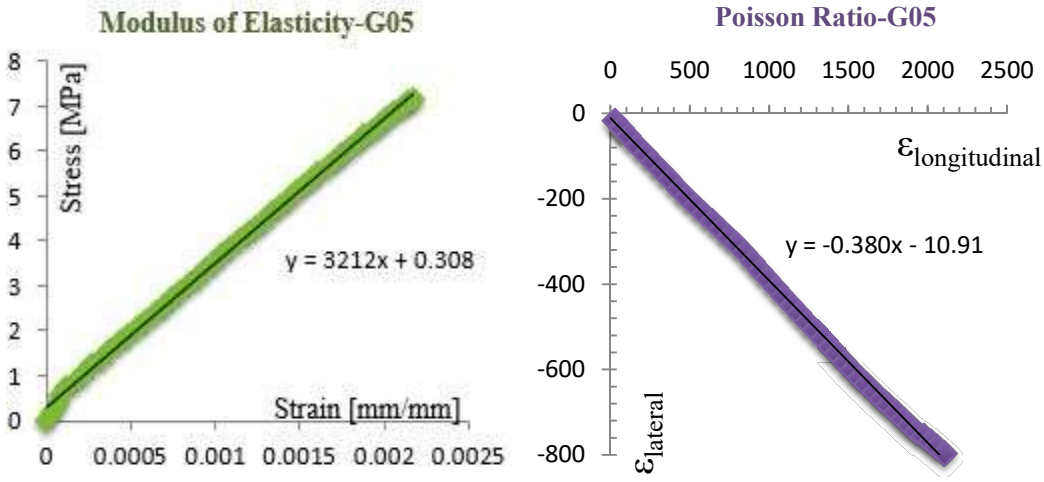

Figure 4.10 Modulus of elasticity and Poisson's ratio value of G05 specimen

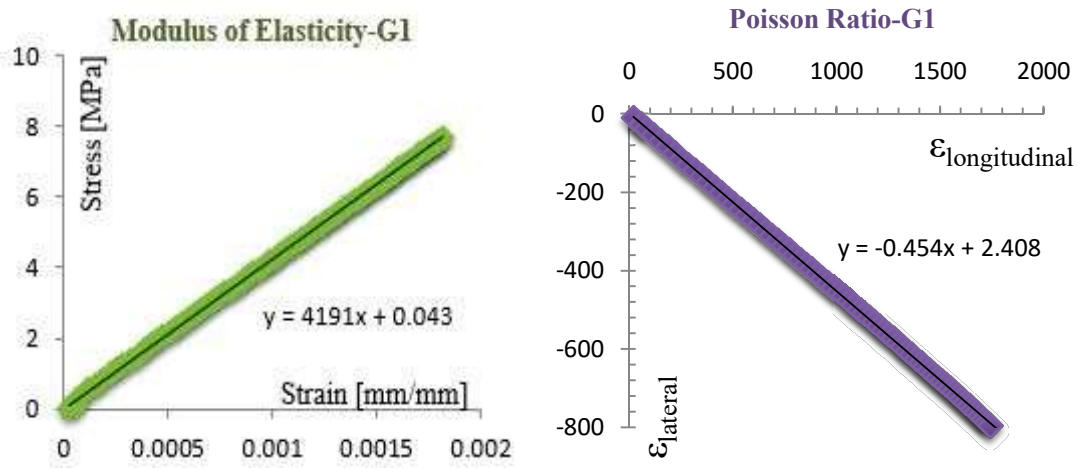

Figure 4.11 Modulus of elasticity and Poisson's ratio value of G1 specimen

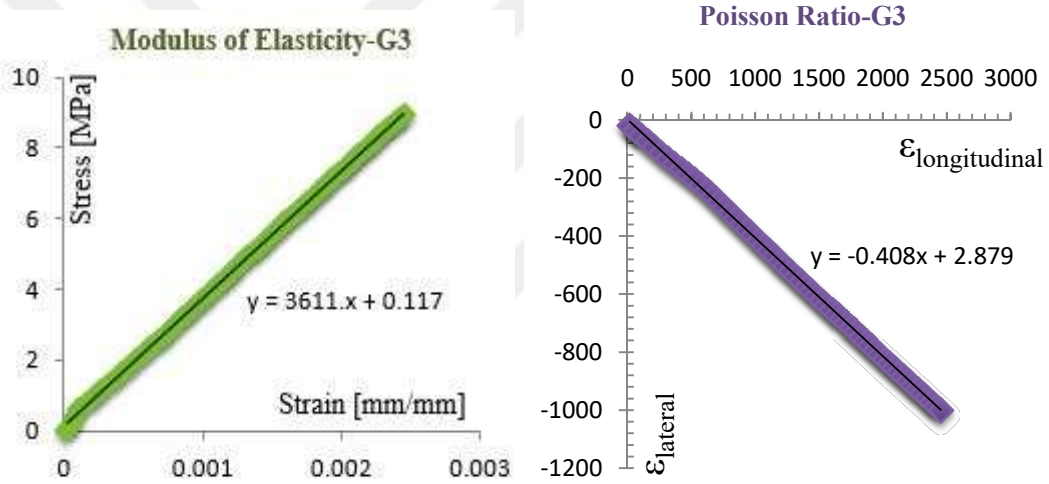

Figure 4.12 Modulus of elasticity and Poisson's ratio value of G3 specimen

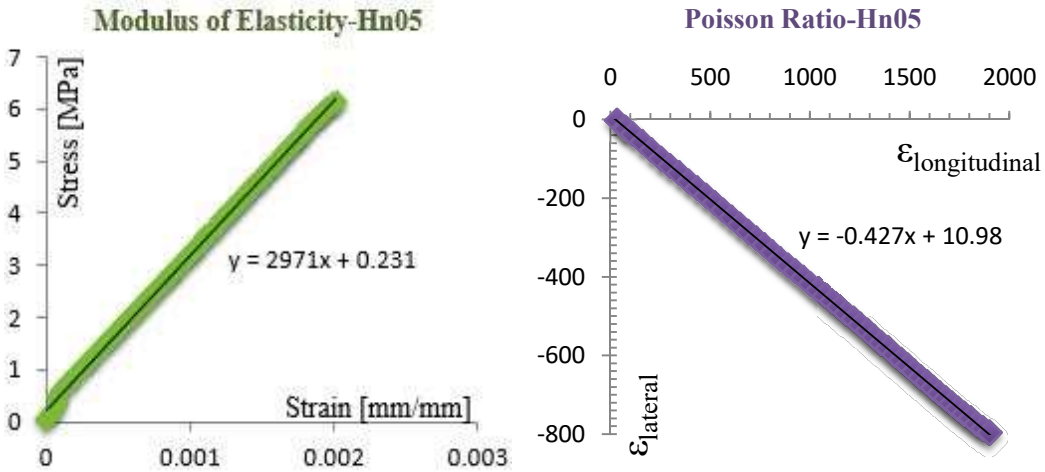

Figure 4.13 Modulus of elasticity and Poisson's ratio value of Hn05 specimen

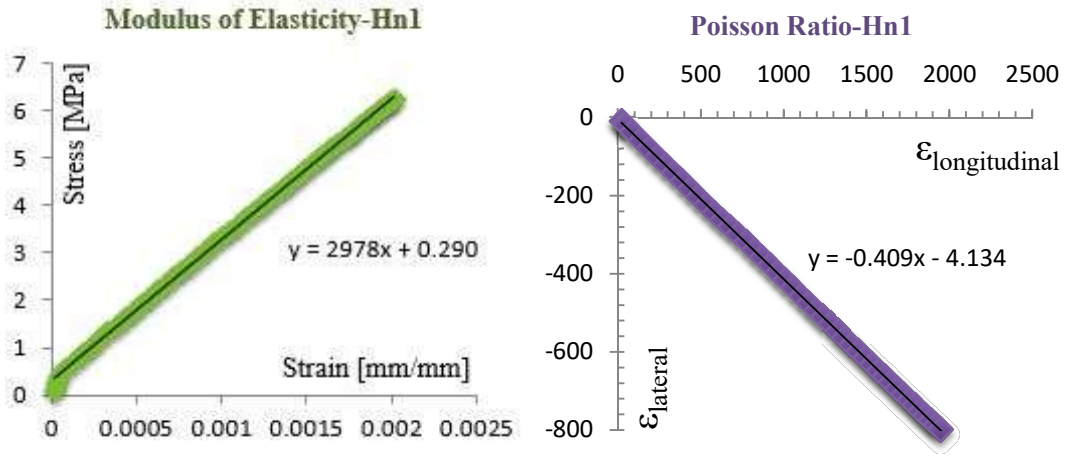

Figure 4.14 Modulus of elasticity and Poisson's ratio value of Hn1 specimen

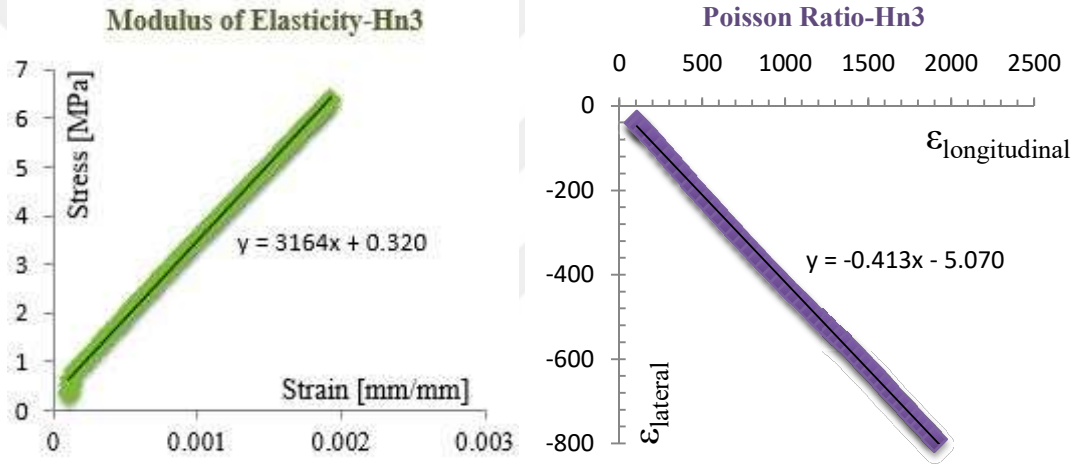

Figure 4.15 Modulus of elasticity and Poisson's ratio value of Hn3 specimen

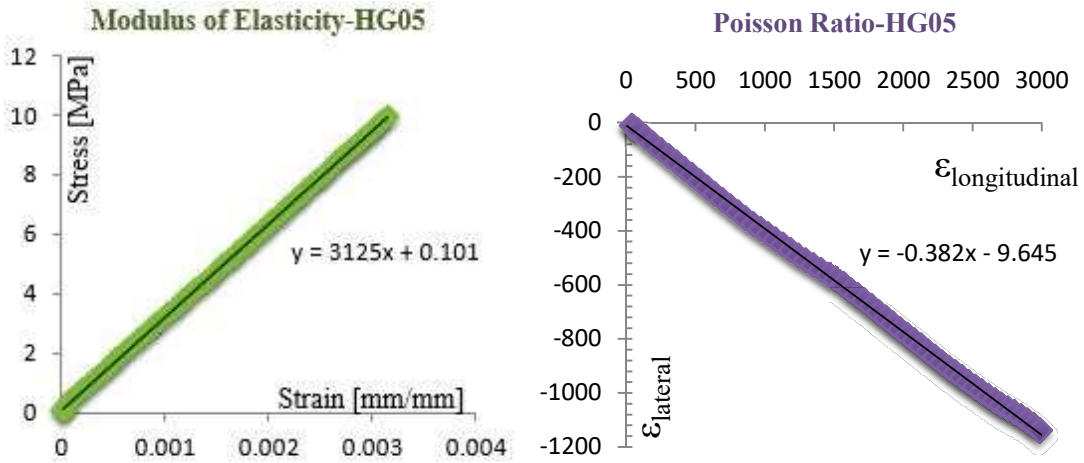

Figure 4.16 Modulus of elasticity and Poisson's ratio value of HG05 specimen

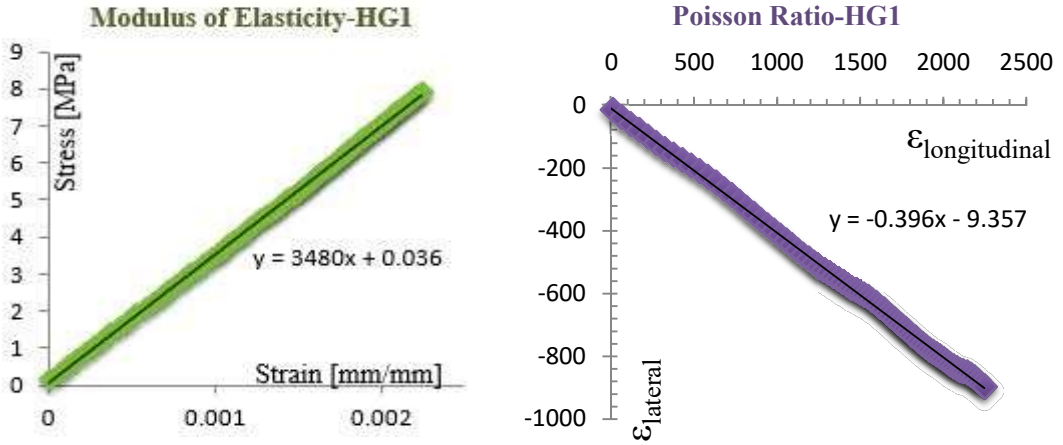

Figure 4.17 Modulus of elasticity and Poisson's ratio value of HG1 specimen

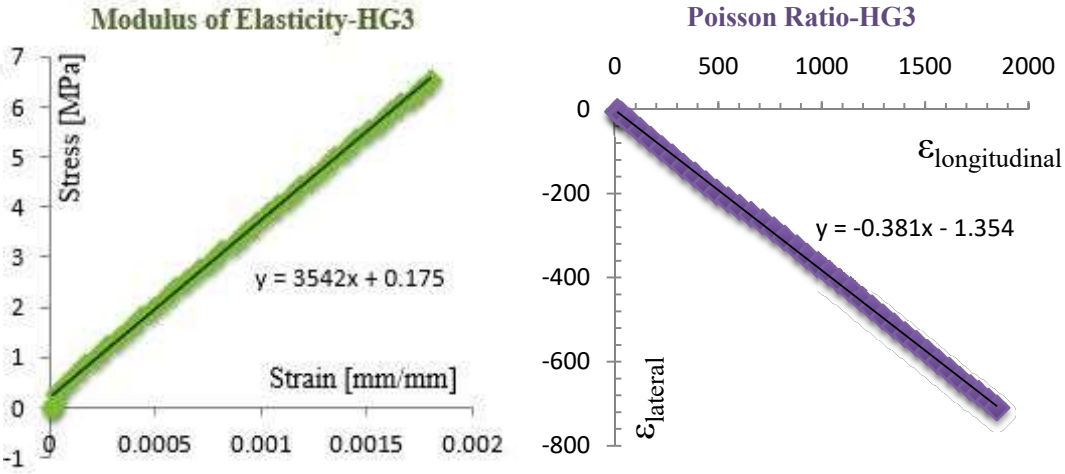

Figure 4.18 Modulus of elasticity and Poisson's ratio value of HG3 specimen

Table 4.1 Obtained values of Poisson's ratio and modulus of elasticity

	Modulus of Elasticity [MPa]	Poisson's Ratio [mm/mm]
Rc	3276	0.429
H05	2931	0.399
H1	3043	0.423
H3	3006	0.395
G05	3212	0.380
G1	4191	0.454
G3	3611	0.408
Hn05	2971	0.427
Hn1	2978	0.409
Hn3	3164	0.413
HG05	3125	0.382
HG1	3480	0.396
HG3	3542	0.381

4.3 Tensile Test

Tensile test is carried out to obtain the stress-strain diagram and to determine the tensile properties and mechanical behavior of the material.

Stress: It refers to the load acting on the unit area and is calculated with equation 4.3 (Gere, 2004).

$$\sigma = \frac{F}{A_o} \tag{4.3}$$

σ: Engineering stress [MPa]

F: Applied force [N]

$A_{0:}$ Cross section area before the experiment [mm^2]

Strain: It is rate of the changed of gauge length of the specimen to the specimen's original gauge length, when force is applied to specimen (Gere, 2004).

$$\varepsilon = \frac{\Delta L}{L_o} \tag{4.4}$$

ε: Engineering strain [mm/mm]

ΔL: Changed length of the specimen [mm]

$L_{0:}$ Length of the specimen before the experiment [mm]

4.4 Experimental Analysis

The influences of mineral types and weight ratios on the mechanical properties like stress value were investigated experimentally. They were fixed with grippers and experimental analysis was carried out at a constant speed of 1 mm/min.

Shimadzu AG-X Tensile Test Equipment was used to determine the stress and strain values of the composite specimens as shown in Figure 4.19.

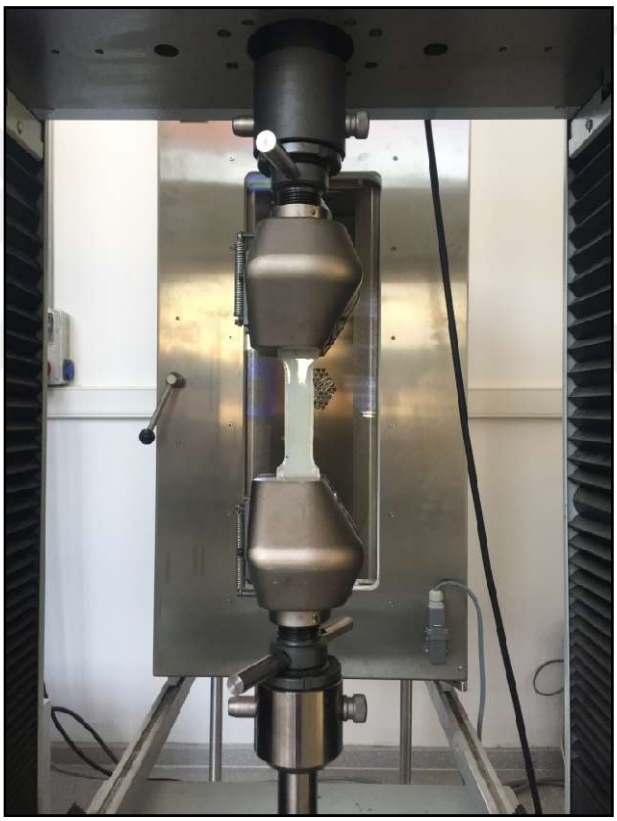

Figure 4.19 Tensile test (Personal archive, 2018)

Mold 2, that was manufactured with additive manufacturing method with using 3D printer, was designed according to ASTM D3039 tensile test standard with SolidWorks 2017 program.

4.5 Results of Tensile Test

The influences of mineral types and weight ratios on the mechanical properties were investigated experimentally and stress-strain graphs were obtained in Figure 4.20.

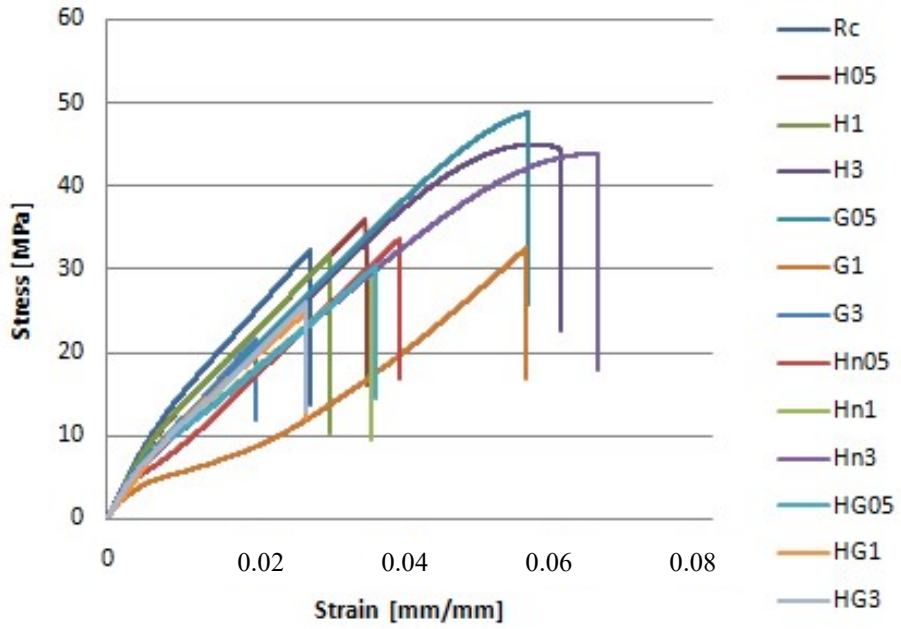

Figure 4.20 Stress-strain diagram

According to stress-strain values obtained by the tensile tests, huntite mineral added specimens were broken with more elongation than graphene mineral added specimens. Namely, it shows that huntite increases the ductility of the materials.

The maximum stress value was observed in the huntite mineral added specimens.

CHAPTER FIVE
BUCKLING ANALYSIS

5.1 Buckling

Buckling is a deformation type, which occurs under the vertical load on columns. Elastic zone limitation of buckling is critical load that is calculated with different support conditions with the help of Euler Formula (Gere, 2004).

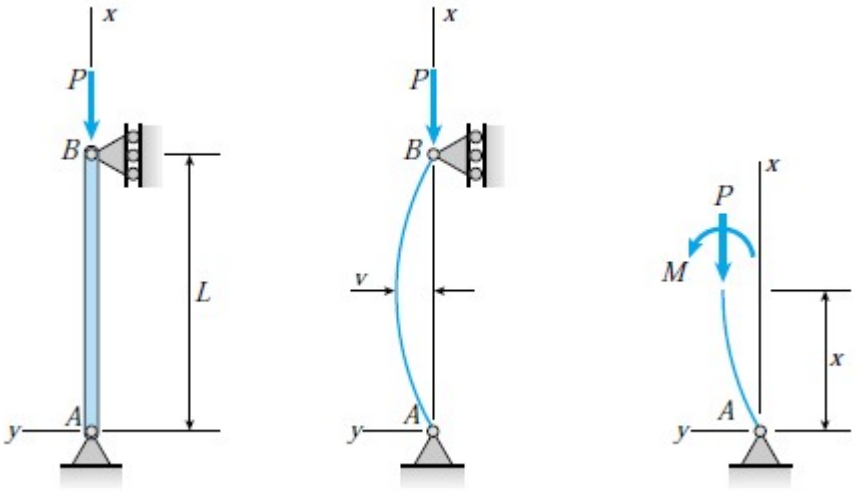

Figure 5.1 Column, buckled shape column, axial force P and bending moment M acting at a cross section with pinned ends column respectively (Gere, 2004)

$$EI\frac{d^2y}{dx^2} = M \tag{5.1}$$

M: bending moment at any cross section,
y: lateral deflection in the y direction,
EI: the flexural rigidity for bending in the xy plane.

The axial force P and bending moment M acting at the cross section are shown in Figure 5.1. From equilibrium of moments about point A,

$$M + Py = 0 \tag{5.2}$$

$$EI\frac{d^2y}{dx^2} + Py = 0 \tag{5.3}$$

Equation 5.3 is a second order homogeneous linear differential equation with constant coefficients. If k is assigned as positive variable, this equation can be solved (Gere, 2004).

$$k^2 = \frac{P}{EI} \tag{5.4}$$

$$y'' + k^2y = 0 \tag{5.5}$$

with general solution in mathematics,

$$y = C_1 \sin kx + C_2 \cos kx \tag{5.6}$$

Buckled column has pinned joints. It means that deflection (y) is zero at x=0 and x=L. Using the first boundary conditions which is y(0) = 0 at equation 5.6, $C_2 = 0$ is calculated. So, Equation 5.6 formed as;

$$y = C_1 \sin kx \tag{5.7}$$

Then using with second boundary conditions which is y(L) = 0 at equation 5.6, equation 5.7 formed as;

$$0 = C_1 \sin kL \tag{5.8}$$

$$\sin kL = 0 \tag{5.9}$$

This equation is available when kL = 0, π, 2 π, .. But, kL = 0 means that P = 0, this solution is not of interest. Therefore, the solutions we will consider are kL = π, 2π, 3 π .. For the critical buckling load, k = π / L is calculated and the square of k

value is equal to equation 5.4. Critical buckling load (P_{cr}) that was described by Euler in 1744 forms as equation 5.10.

$$P_{cr} = \frac{\pi^2 EI}{L^2} \tag{5.10}$$

This equation is derived for pinned joint. For other joint types, critical buckling load related with effective length L_e which is same as the column length for pinned-end column. In general, critical buckling load is written below as Equation 5.11 (Gere, 2004).

$$P_{cr} = \frac{\pi^2 EI}{{L_e}^2} \tag{5.11}$$

The critical loads and effective lengths for different support conditions are demonstrated in Figure 5.2.

(a) Pinned-pinned column	(b) Fixed-free column	(c) Fixed-fixed column	(d) Fixed-pinned column
$P_{cr} = \frac{\pi^2 EI}{L^2}$	$P_{cr} = \frac{\pi^2 EI}{4L^2}$	$P_{cr} = \frac{4\pi^2 EI}{L^2}$	$P_{cr} = \frac{2.046\,\pi^2 EI}{L^2}$
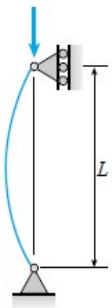	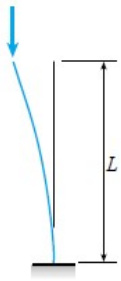	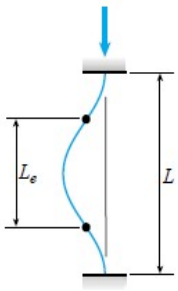	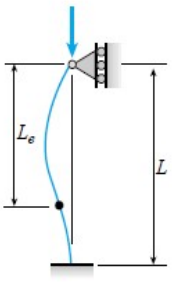
$L_e = L$	$L_e = 2L$	$L_e = 0.5L$	$L_e = 0.699L$
$K = 1$	$K = 2$	$K = 0.5$	$K = 0.699$

Figure 5.2 Critical loads and effective lengths for different support conditions (Gere, 2004)

5.2 Experimental Analysis

The effects of mineral types and weight ratios on the critical buckling loads were investigated experimentally. Shimadzu AG-X Tensile Test Equipment was used to determine the critical buckling load of the composite specimens, as shown in Figure 5.3. The clamped-clamped boundary condition was considered in numerical and experimental analyses.

Figure 5.3 Experimental setup (Personal archive, 2018)

The specimens which have 25 x 5 x 0.3 cm^3 dimensions were formed with big cavity of Mold 1. They were fixed to the grippers to prevent movement of the specimen under the clamped boundary condition. Experimental analysis was carried out at a constant speed of 0.1 mm/min.

5.3 Numerical Analysis

In the numerical analysis, the critical buckling load was obtained using ANSYS Mechanical APDL 17.0 finite element software for the clamped-clamped boundary condition. Modulus of elasticity and Poisson's ratio which were obtained from tensile test with strain gauge, were used as an input. Beam188 element type having two nodes was chosen and the finite element model was divided into a hundred finite elements. Block Lanczos – Eigen Buckling method was used in the buckling analysis. First five mode buckling loads were investigated with software. Mode shapes associated with buckling shapes are shown in figures from Figure 5.5 to Figure 5.9 for pure resin specimen.

The finite element model length was designed as 190 mm to compare results with experimental analysis. Because in experimental analysis, each test gripper holds the specimens 30 mm from the end of them. Figure 5.4 shows the finite element model created by ANSYS Mechanical APDL 17.0 finite element software.

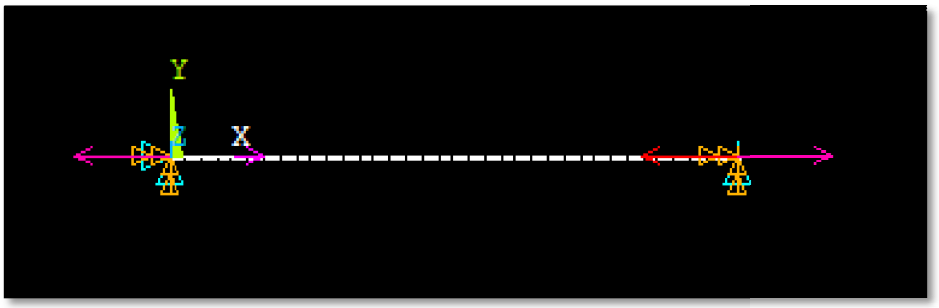

Figure 5.4 Finite element model (Personal archive, 2018)

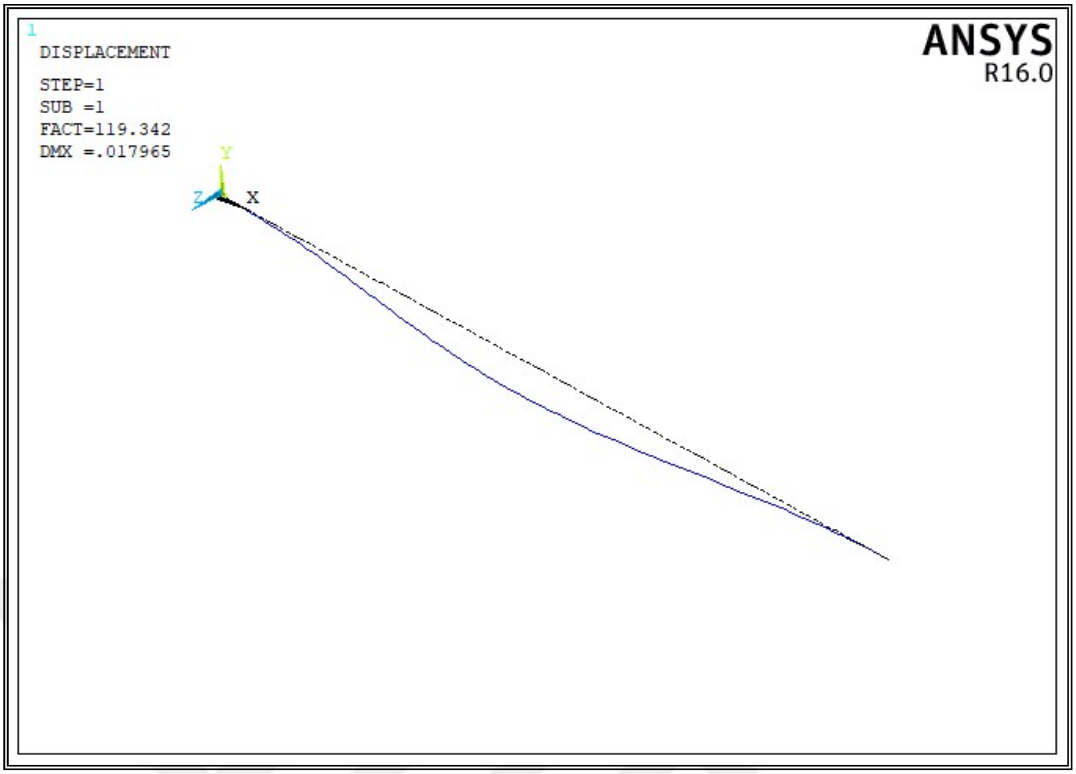

Figure 5.5 Buckling shape for pure resin associated with first mode (Personal archive, 2019)

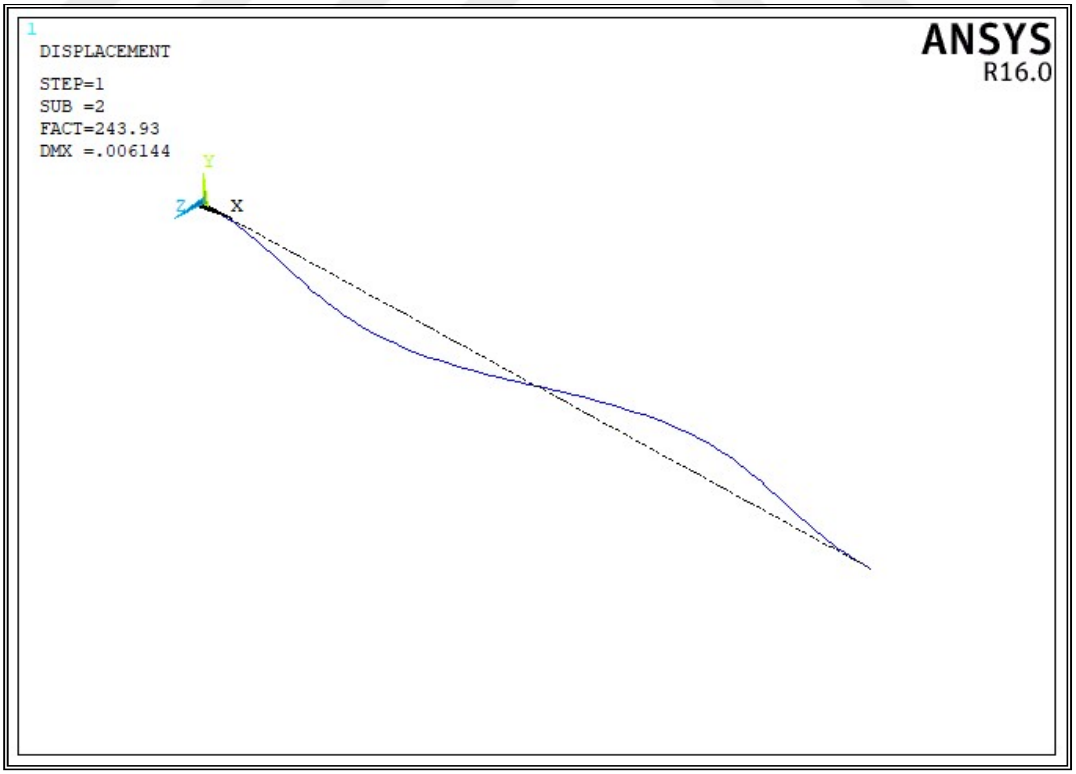

Figure 5.6 Buckling shape for pure resin associated with second mode (Personal archive, 2019)

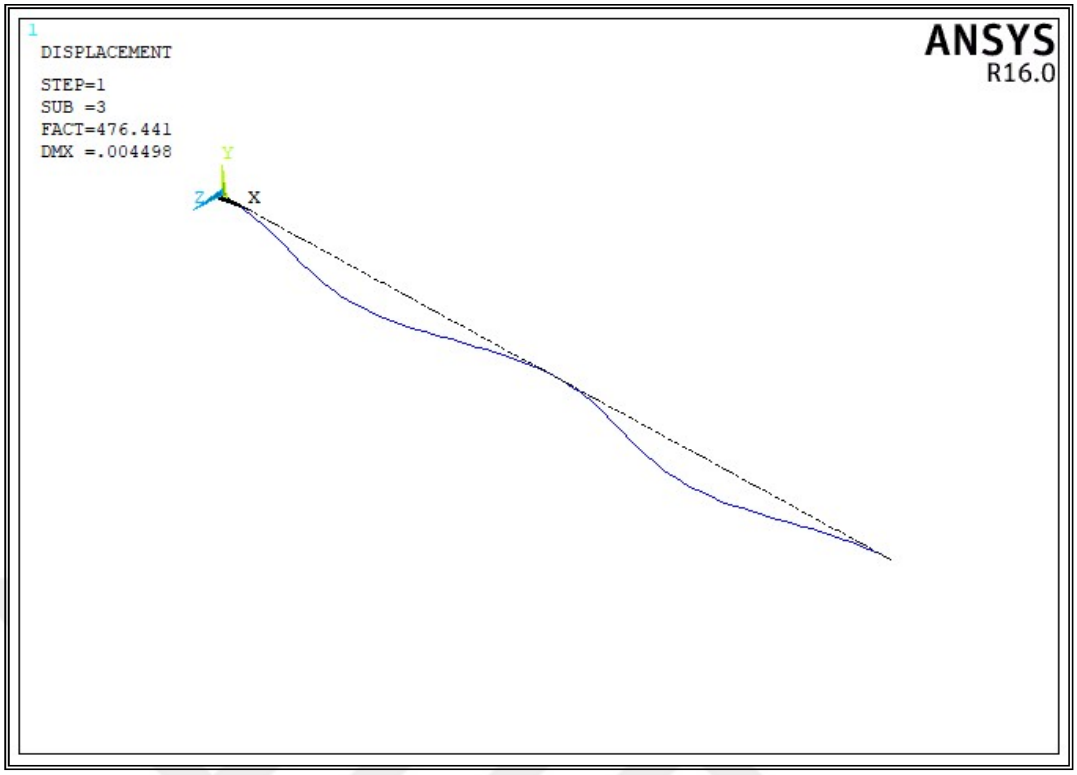

Figure 5.7 Buckling shape for pure resin associated with third mode (Personal archive, 2019)

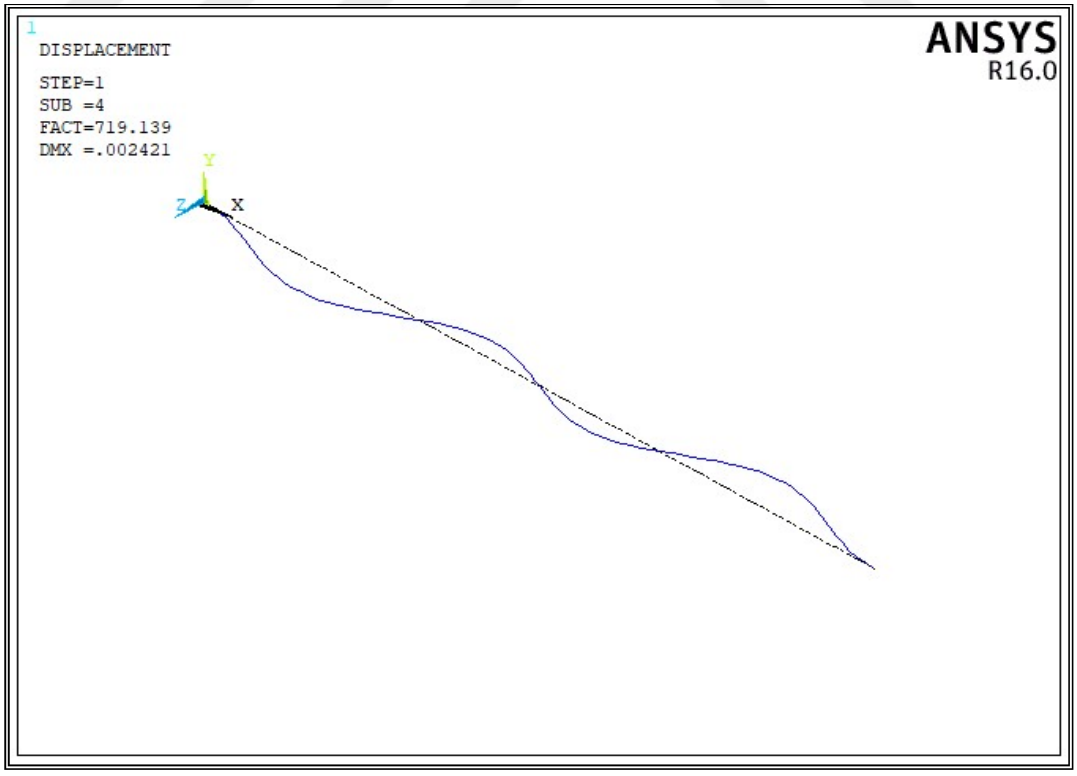

Figure 5.8 Buckling shape for pure resin associated with fourth mode (Personal archive, 2019)

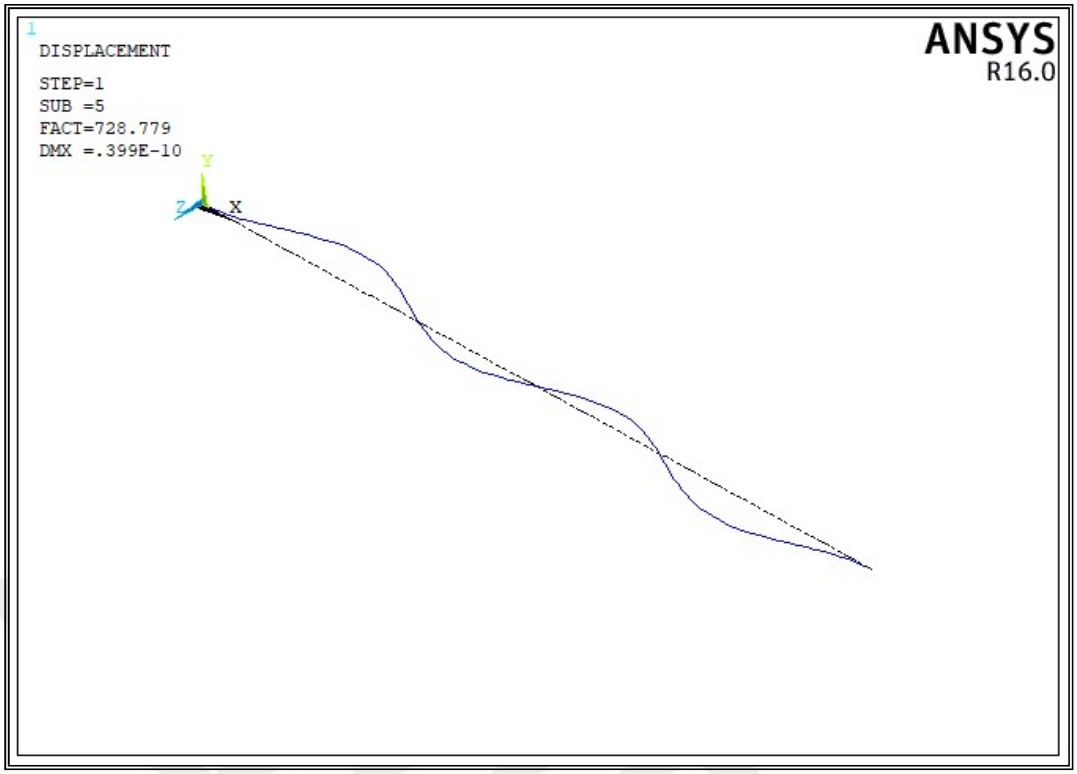

Figure 5.9 Buckling shape for pure resin associated with fifth mode (Personal archive, 2019)

5.4 Results of Buckling Analysis

5.4.1 Buckling Loads Obtained from Numerical Analysis

The effects of mineral types and weight ratios on the buckling loads according to mode shapes were examined using ANSYS finite element software. First five mode buckling load values are given in Table 5.1 and Figure 5.10 for pure resin, huntite, graphene, nano sized huntite and mix of huntite-graphene specimens.

As shown in the Figure 5.10, differences between mode 4 and mode 5 buckling load values are small. In general, huntite mineral showed better results on the buckling load compared to graphene specimens. Between mixture of huntite and graphene mineral specimens, buckling load of the maximum graphene amount (HG3) is minimum for five mode loads.

Table 5.1 Five mode buckling load values [N]

	Rc	H05	H1	H3	G05	G1	G3
Mode 1	119.34	359.83	337.5	369.04	356.27	203.15	152.26
Mode 2	243.93	734.11	688.67	752.91	727.05	415.08	311.18
Mode 3	476.44	1430.2	1341.9	1466.8	1416.9	810.33	607.68
Mode 4	719.14	2151.6	2019.5	2206.8	2132.7	1217.9	917.02
Mode 5	728.78	2229.7	2057.7	2293.3	2239.7	1217.9	943.16

	Rc	Hn05	Hn1	Hn3	HG05	HG1	HG3
Mode 1	119.34	364.72	443.52	388.42	383.66	427.23	222.86
Mode 2	243.93	744.04	904.42	792.42	782.76	871.63	455.24
Mode 3	476.44	1449.4	1760.7	1543.7	1525	1698.1	888.43
Mode 4	719.14	2180.2	2646.6	2322.2	2294.5	2554.7	1339.6
Mode 5	728.78	2215.8	2724.6	2383.1	2406.6	2653.1	1404.9

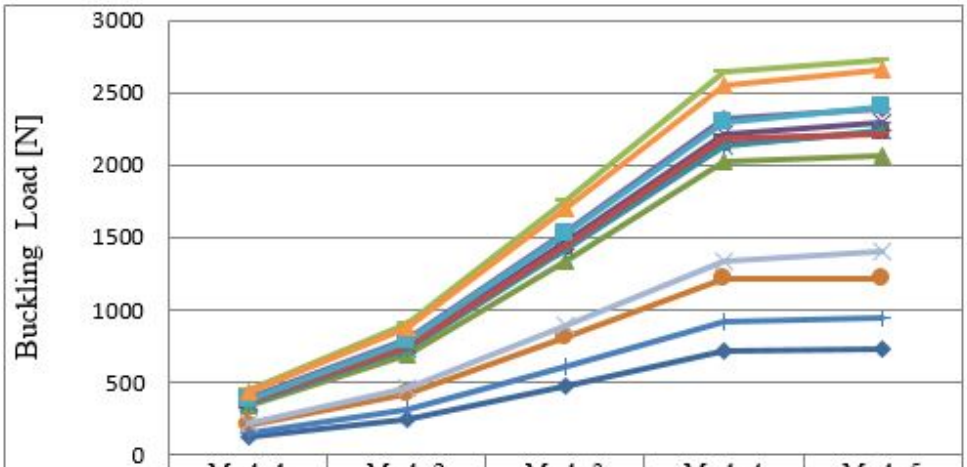

	Mode 1	Mode 2	Mode 3	Mode 4	Mode 5
Rc	119.34	243.93	476.44	719.14	728.78
H05	359.83	734.11	1430.2	2151.6	2229.7
H1	337.5	688.67	1341.9	2019.5	2057.7
H3	369.04	752.91	1466.8	2206.8	2293.3
G05	356.27	727.05	1416.9	2132.7	2239.7
G1	203.15	415.08	810.33	1217.9	1217.9
G3	152.26	311.18	607.68	917.02	943.16
Hn05	364.72	744.04	1449.4	2180.2	2215.8
Hn1	443.52	904.42	1760.7	2646.6	2724.6
Hn3	388.42	792.42	1543.7	2322.2	2383.1
HG05	383.66	782.76	1525	2294.5	2406.6
HG1	427.23	871.63	1698.1	2554.7	2653.1
HG3	222.86	455.24	888.43	1339.6	1404.9

Figure 5.10 Five mode buckling load values obtained from ANSYS

5.4.2 Comparing Experimental and Numerical Analyses

The effects of mineral types and weight ratios on the critical buckling loads between numerical and experimental analyses were given in Table 5.2 and Figure 5.11. In addition, differences between numerical and experimental analyses were calculated. As shown in Table 5.2, results obtained by the numerical and experimental analyses are so close to each other.

Table 5.2 Critical buckling load values obtained by the numerical and experimental analyses

	Specimens	Numeric Critical Buckling Load [N]	Experimental Critical Buckling Load [N]	Difference %
Pure resin	Rc	119.34	112.500	6.080
Huntite	H05	359.83	336.438	6.953
	H1	337.50	335.281	0.662
	H3	369.04	371.500	-0.662
Graphene	G05	356.27	333.875	6.708
	G1	203.15	205.625	-1.204
	G3	152.26	139.906	8.830
Huntite nano size	Hn05	364.72	365.719	-0.273
	Hn1	443.52	435.688	1.798
	Hn3	388.42	408.500	-4.916
Huntite and Graphene mixture	HG05	383.66	374.281	2.506
	HG1	427.23	433.156	-1.368
	HG3	222.86	207.656	7.322

For all specimens reinforced by the minerals, the critical buckling load values obtained by both numerical and experimental analyses are higher than the pure resin, as shown in Figure 5.11. Especially, the nano-sized particle structure of huntite minerals show significant increase in critical buckling load values compared to the other specimens. The critical buckling load value of Hn1 specimen which determined by both numerical and experimental analyses reaches the highest buckling load value. However, there is negative effect on the critical buckling load by increasing the weight ratio of graphene amount.

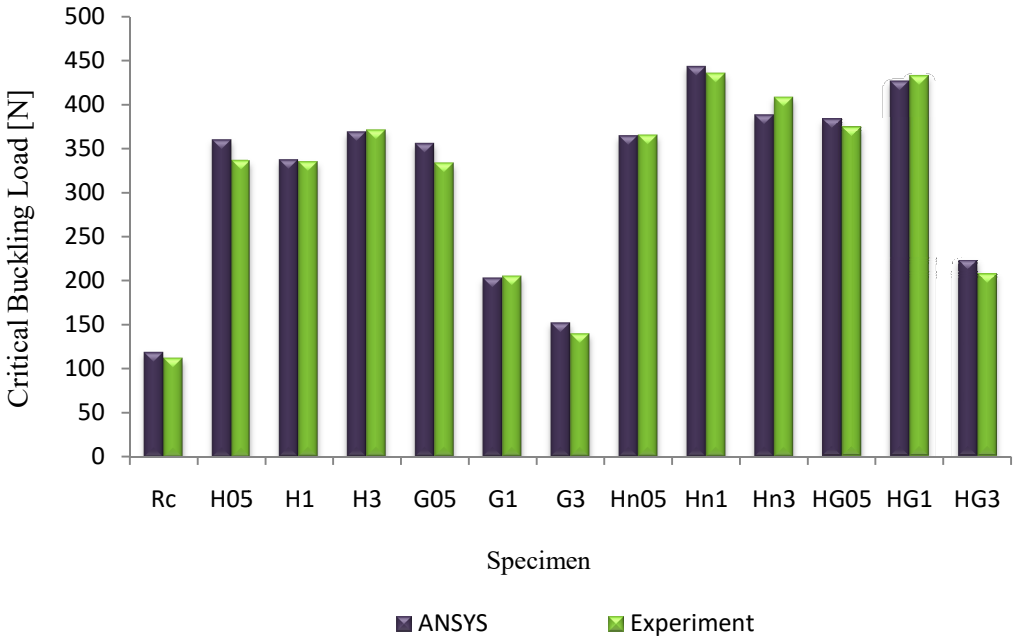

Figure 5.11 Critical buckling load values obtained from numerical and experimental analyses

CHAPTER SIX
DYNAMIC MECHANICAL ANALYSIS

6.1 Dynamic Mechanical Analysis

Dynamic mechanical analysis (DMA) is the test method with increasing temperature and applying an oscillating force causing sinusoidal stress. This test method is used to determine the viscoelastic characterization of materials like the modulus, the viscosity, and the damping. Sinusoidal stress and strain are calculated by using formulas as follows (Menard, 2008; Sepe, 1998).

$$\sigma(t) = \sigma_0 \sin \omega t \tag{6.1}$$

$$\varepsilon(t) = E\, \sigma_0 \sin \omega t \tag{6.2}$$

σ: The stress value at time t [MPa]

σ_0: The maximum stress [MPa]

ε : The strain value at time t [mm/mm]

ω: The frequency of oscillation [rad/s]

E: Modulus of elasticity [MPa]

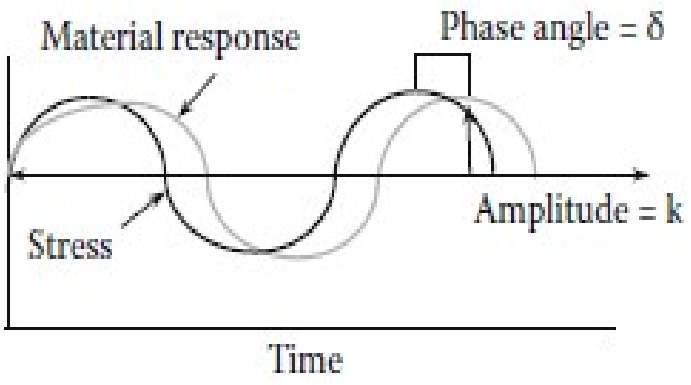

Figure 6.1 Sinusoidal stress, material response and phase angle of these effect (Menard, 2008)

While in tensile test, modulus of elasticity is found at a constant temperature, in dynamic mechanical analysis, modulus of elasticity is found as a function of temperature. Namely, the modulus measured in DMA is not same modulus of the stress–strain curve that is obtained by tensile test. In DMA, complex modulus (E*), elastic modulus or storage modulus (E′) and loss modulus (E″) are obtained results of the sinusoidal force (Menard, 2008; Sepe, 1998).

Storage modulus is related to the amount of energy absorb during the sinusoidal force. As a result, storage modulus is connected with stiffness of the material. It is calculated with Equation 6.3 (Menard, 2008; Sepe, 1998).

$$E' = (\sigma/\varepsilon)\cos\delta \tag{6.3}$$

Loss modulus is related to missing energy and the phase lag between the two sine waves. It is related with damping as shown in Figure 6.1 (Menard, 2008; Sepe, 1998).

$$E'' = (\sigma/\varepsilon)\sin\delta \tag{6.4}$$

The ratio of loss modulus (E″) and elastic modulus (E′) called damping ratio. Material energy loses and internal friction are related with damping ratio. Damping ratio is the tangent value of phase angle (Menard, 2008; Sepe, 1998).

$$\tan\delta = \frac{E''}{E'} \tag{6.5}$$

Another stractural feature that is found with DMA is glass transition temparature (T_g). Storage modulus changes little from the initial temperature to glass transition temparature. However, storage modulus drops abruptly and material becomes inadequate above glass transition temparature because of molecular internal motions (Menard, 2008; Sepe, 1998).

According to ASTM D7028 standart, glass transition temperature is determined with storage modulus - temperature graphic. In that method, first tangent line is drawn from temperature before the transition and the second tangent line which is approximately the midpoint of the storage modulus drop is drawn. The intersection of the these, two tangent line gives the glass transition temperature (ASTM D7028).

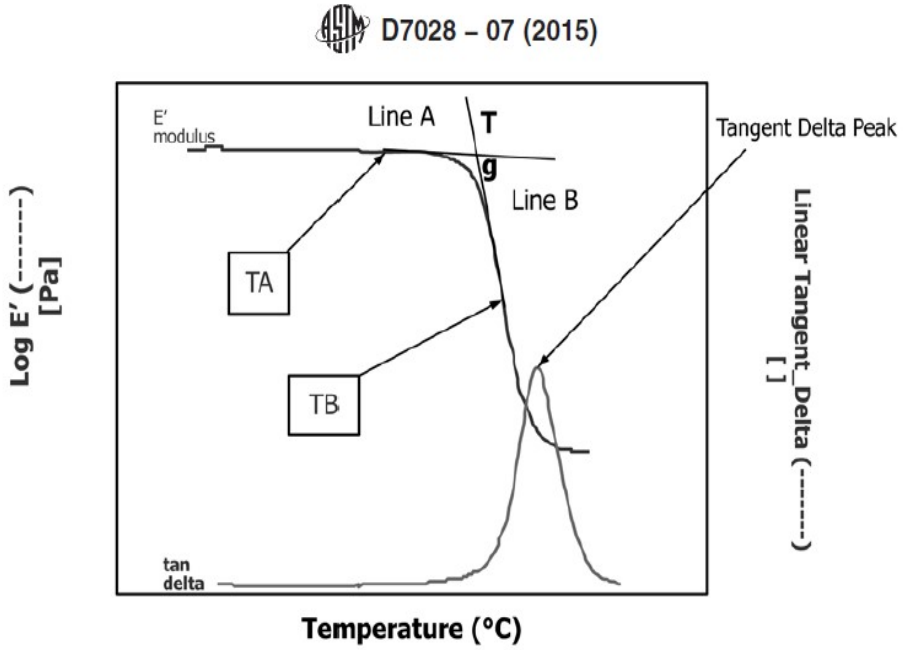

Figure 6.2 Determination of glass transition temperature according to ASTM D7028

Due to the ambiguity of the drawing, an another method is using maximum value of the tan δ. However, polimers have glass transition temperature range. So using tan δ for determination of glass transition temperature may be little different from the real value. In that reason, glass transition temperature determined with the loss modulus - temperature graphic. The peak of the loss modulus is identified as the glass transition temperature (T_g). Namely, maximum loss modulus temperature gives the glass transition temperature because loss modulus is related with the deforming shape, absorbing energy and damping. When tan δ and loss modulus are compared, glass transition temperature which is obtained from maximum value of loss modulus - temperature gives more accurate results (Chee, Jawaid, & Sultan, 2017; Dunson, 2017; Tang, & et al., 2013).

6.2 Three Point Bending Test Fixture

Three point bending test fixture is shown in Figure 6.3. Specimen is placed longitudinal in test fixture and its length are 10% greater than the length between fixing point of the fixture. Middle clamp of the fixture can move up and down to make sinusoidal force. After the specimen is placed in the apparatus, it should be tightened with the torque wrench (Menard, 2008).

Two types of cantilever which are dual cantilever and single cantilever can be used in experiments. Using dual cantilever create small differences in the modulus of elasticity due to shearing strain at the ends and center, also the specimens are more difficult to deform. However, in order to rely on the results using single cantilever, it requires continuous calibration with a known specimen. In that reason dual cantilever was used in experiment (Menard, 2008).

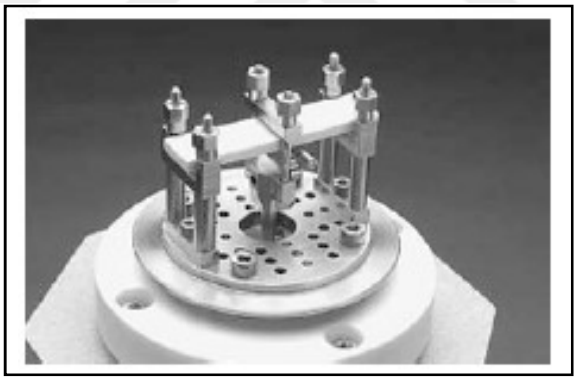

Figure 6.3 Three point bending test aparatus – dual cantilever (Menard, 2008)

6.3 Experimental Setup

Dynamic Mechanical Analysis was applied according to ASTM D7028. For the reasons described above, dual cantilever three point bending test fixture was used with TA Instruments Q800 dynamic mechanical analyzer shown in Figure 6.4. The standard 1 Hz frequency was used in this experiment and the instrument was operated in constant strain mode. Temperature was increased from 35 ºC to 150 ºC at a heating rate of 5 ºC/min.

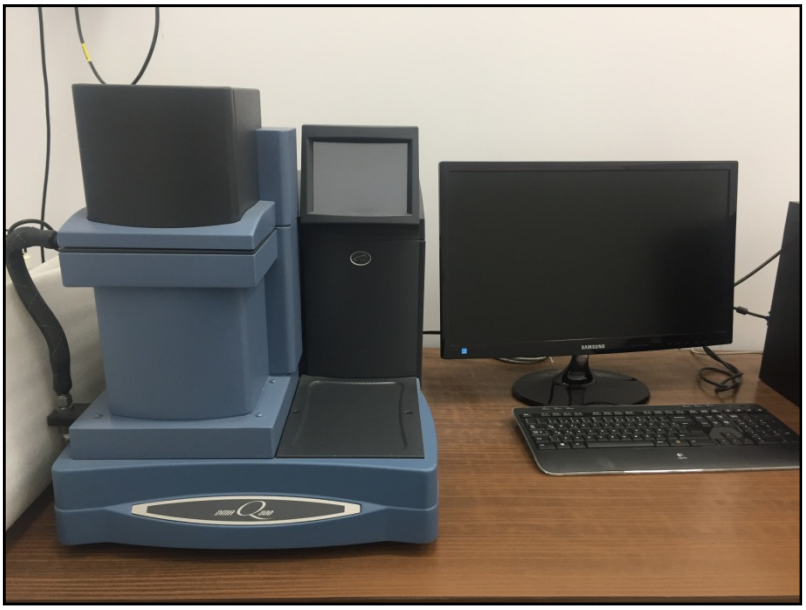

Figure 6.4 Dynamic mechanical analyzer (Personal archive, 2018)

Specimens are shown in Figure 6.5 were formed with Mold 3 and they were shaped according to ASTM D7028 test standard.

Figure 6.5 Specimens formed with mold 3 (Personal archive, 2018)

As a result of the DMA, graphs given in from Figure 6.6 to Figure 6.18 were created for all specimens with the help of Matlab codes. In adition, storage modulus, loss modulus and tan δ graphs are shown Figure 6.19, Figure 6.20 and Figure 6.21 for all specimens. From these graphs, thermo - mechanical properties like storage modulus, loss modulus, tan δ and glass transition temparature are determined and shown in Table 6.1.

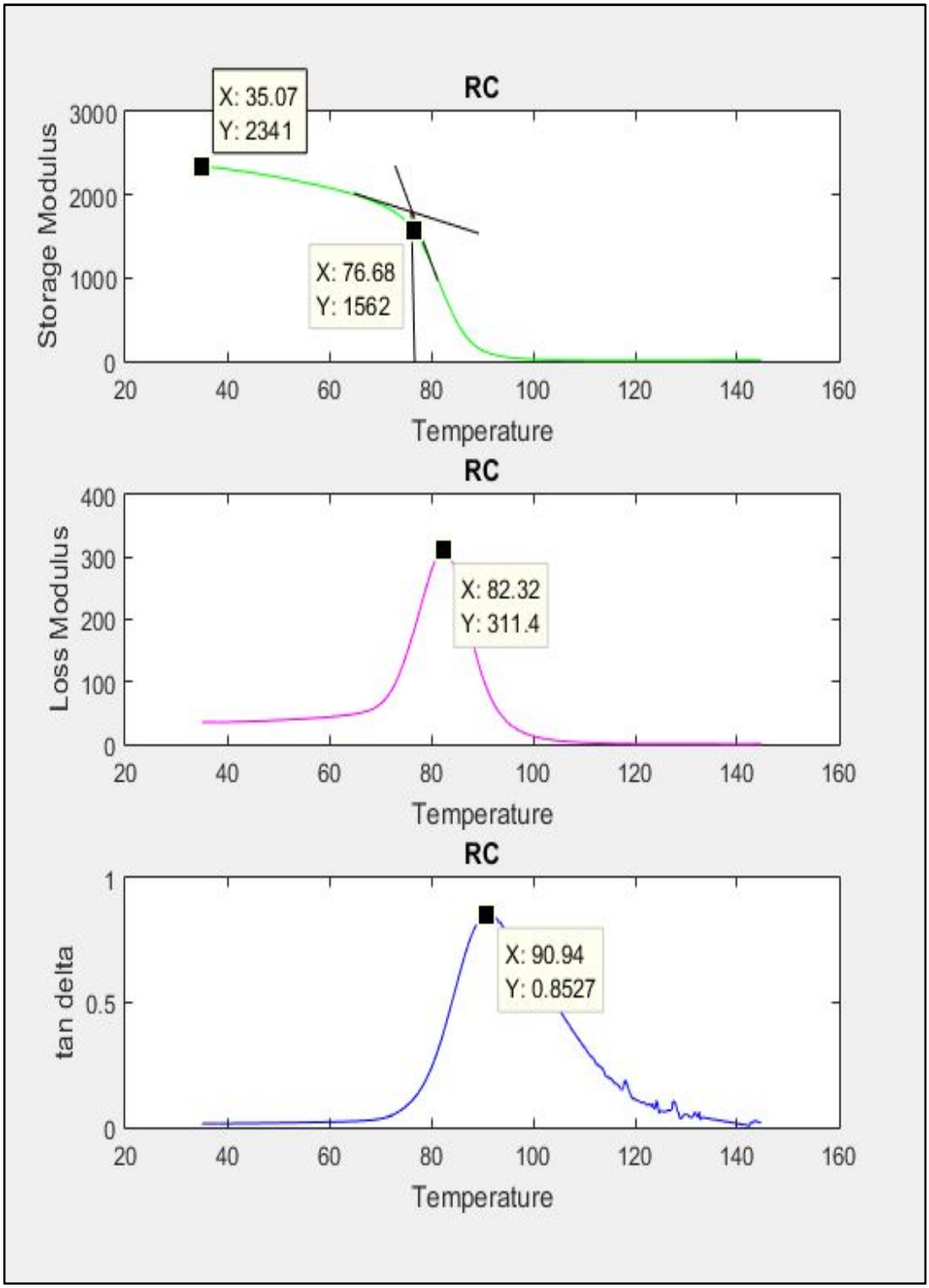

Figure 6.6 Storage modulus, loss modulus and tan δ values of Rc

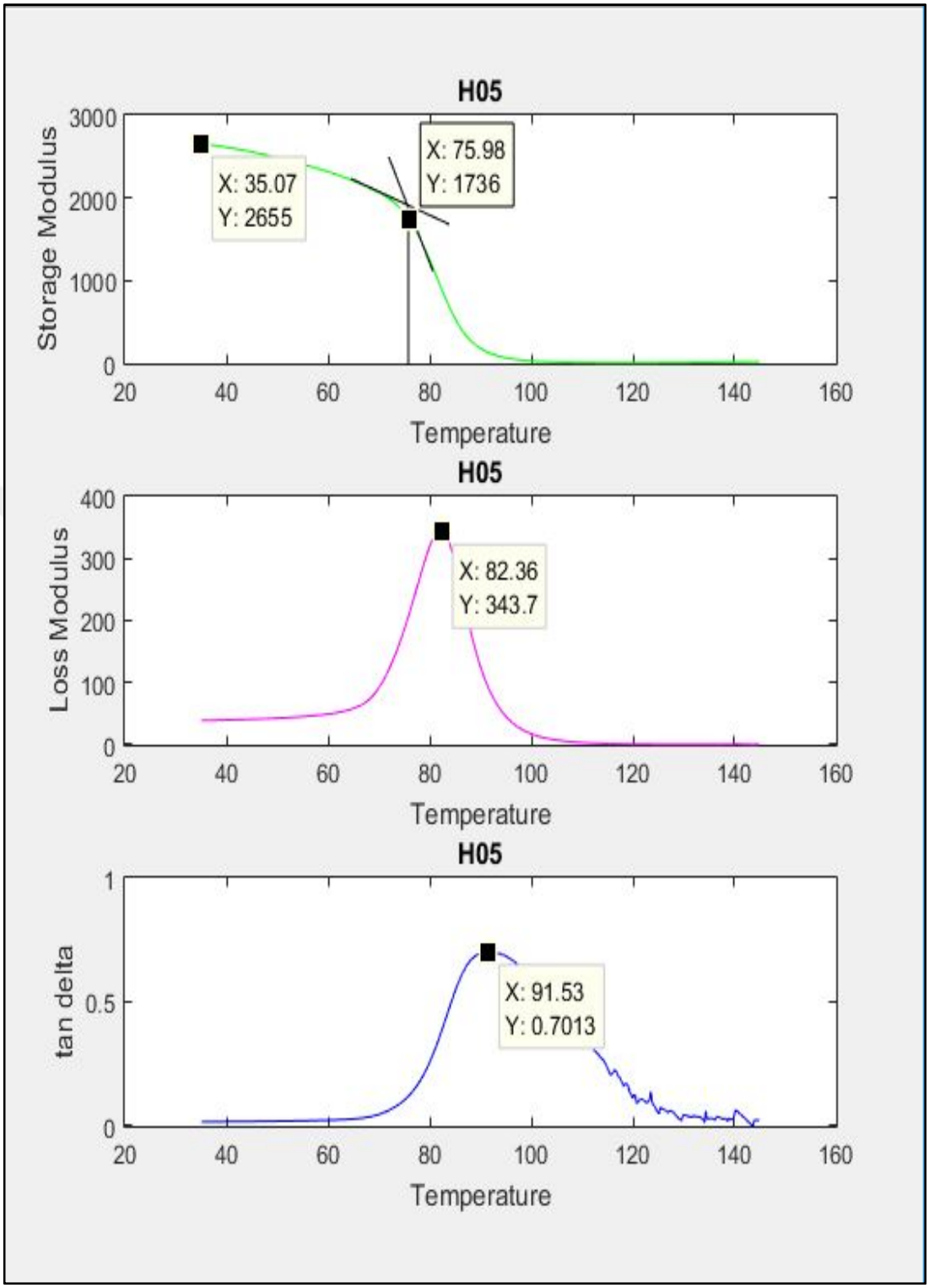

Figure 6.7 Storage modulus, loss modulus and tan δ values of H05

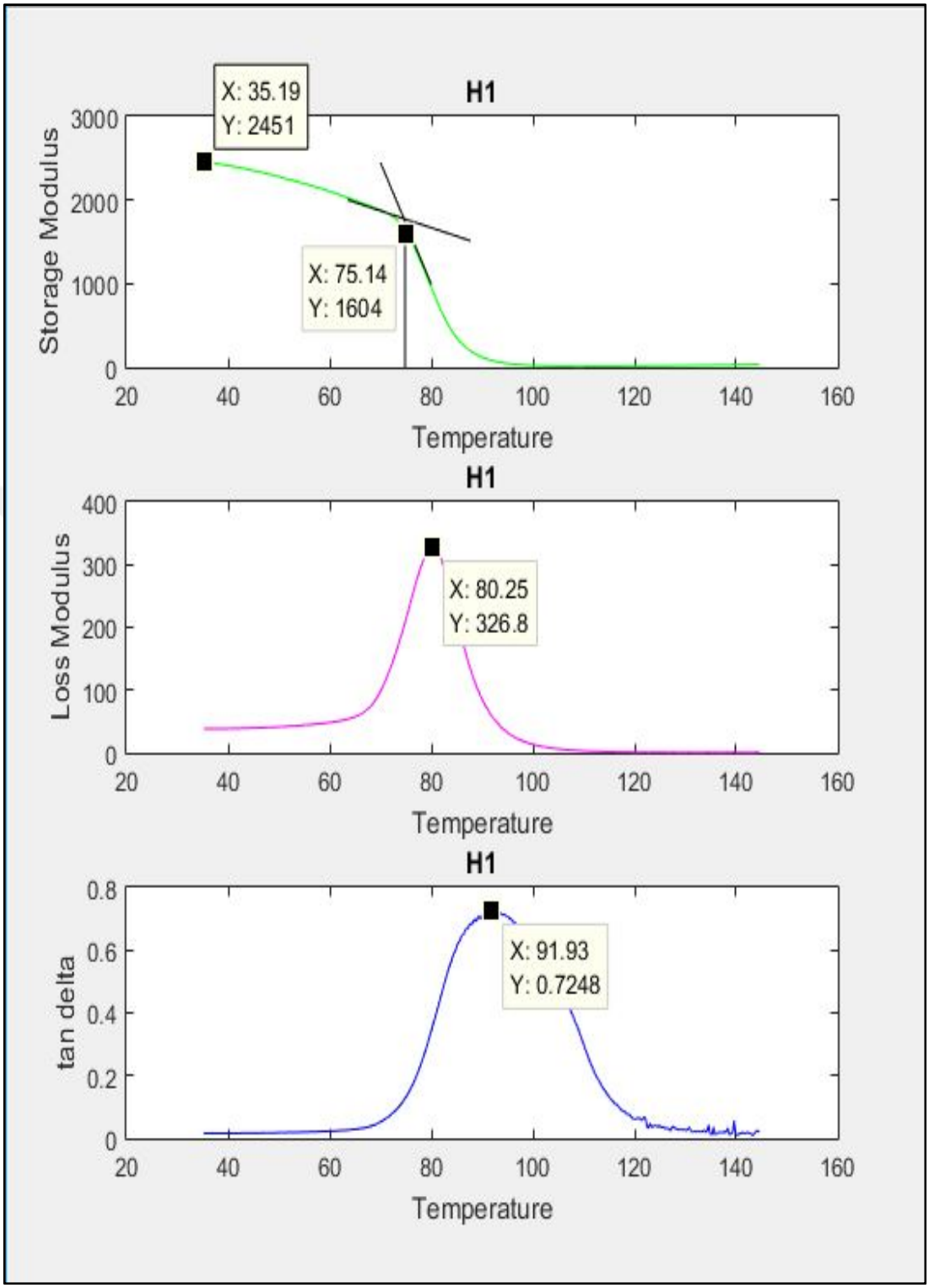

Figure 6.8 Storage modulus, loss modulus and tan δ values of H1

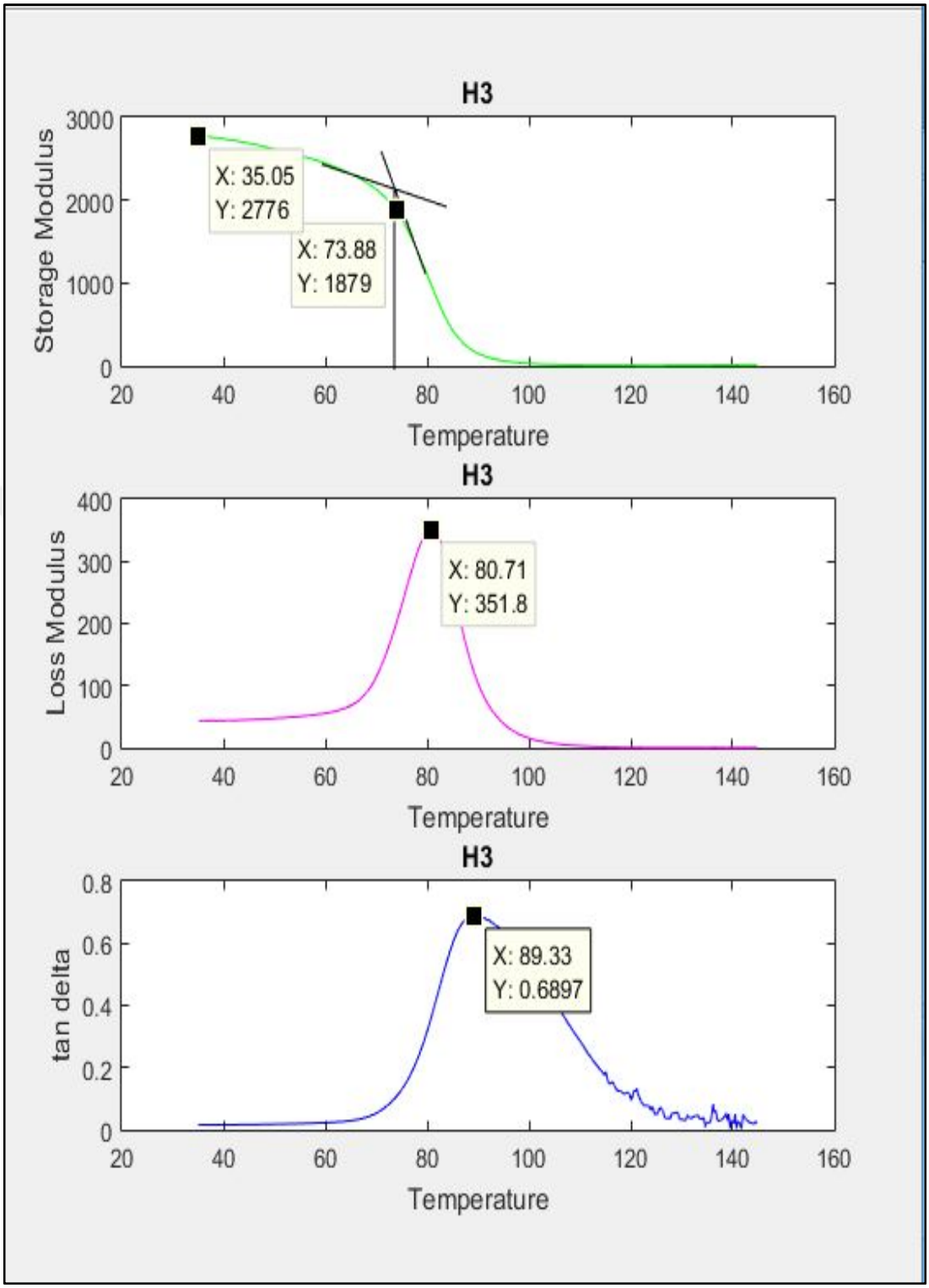

Figure 6.9 Storage modulus, loss modulus and tan δ values of H3

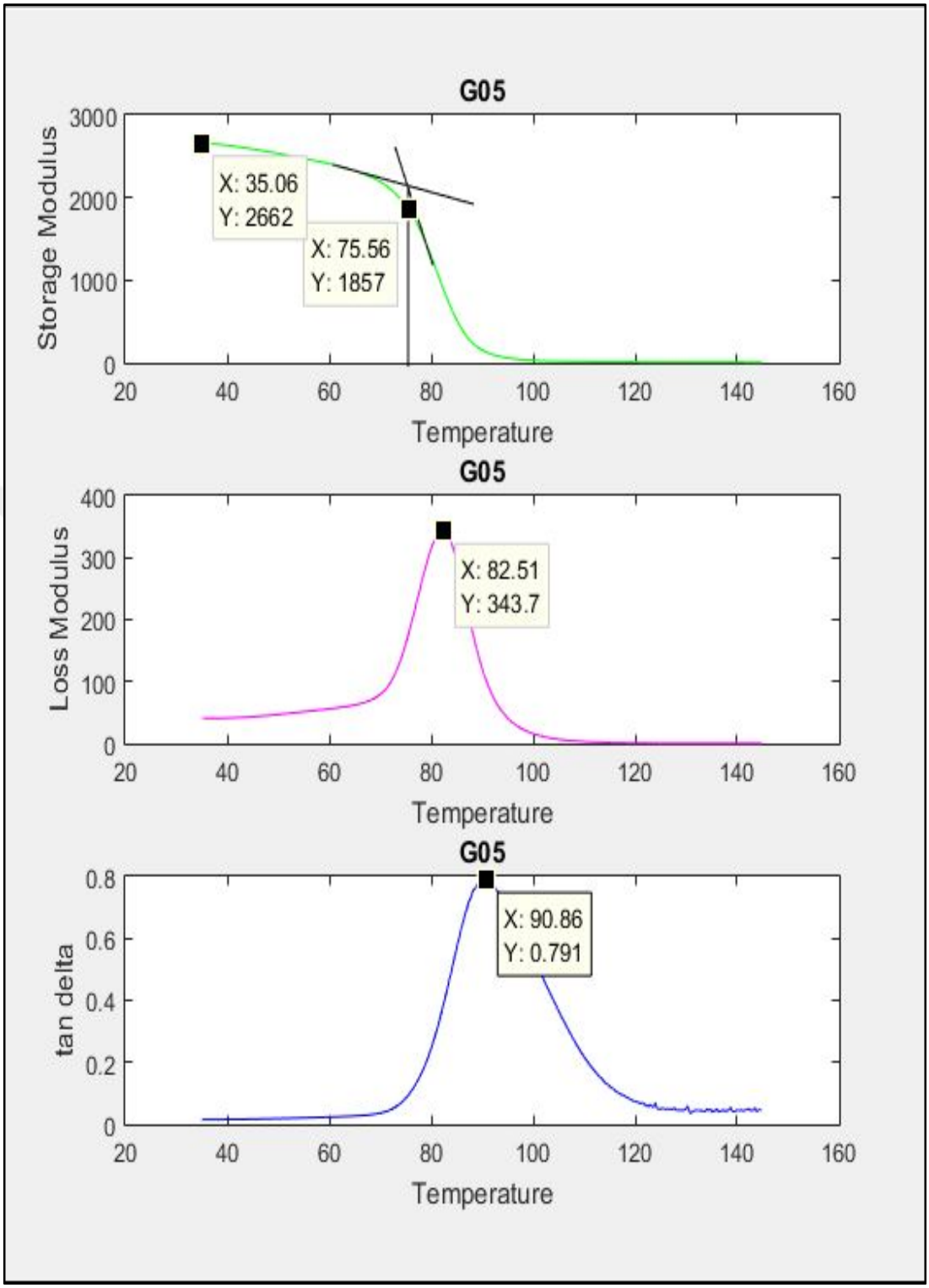

Figure 6.10 Storage modulus, loss modulus and tan δ values of G05

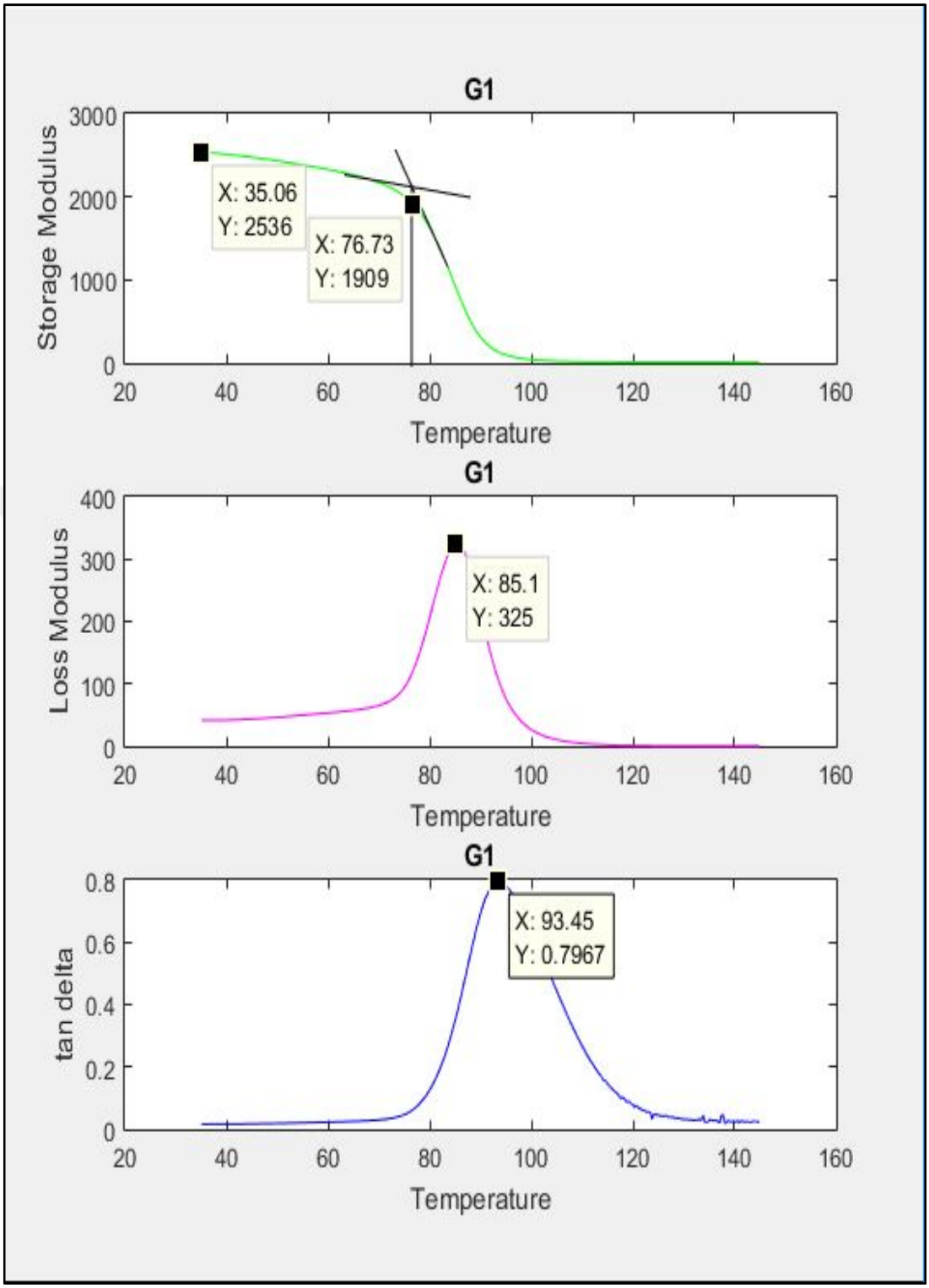

Figure 6.11 Storage modulus, loss modulus and tan δ values of G1

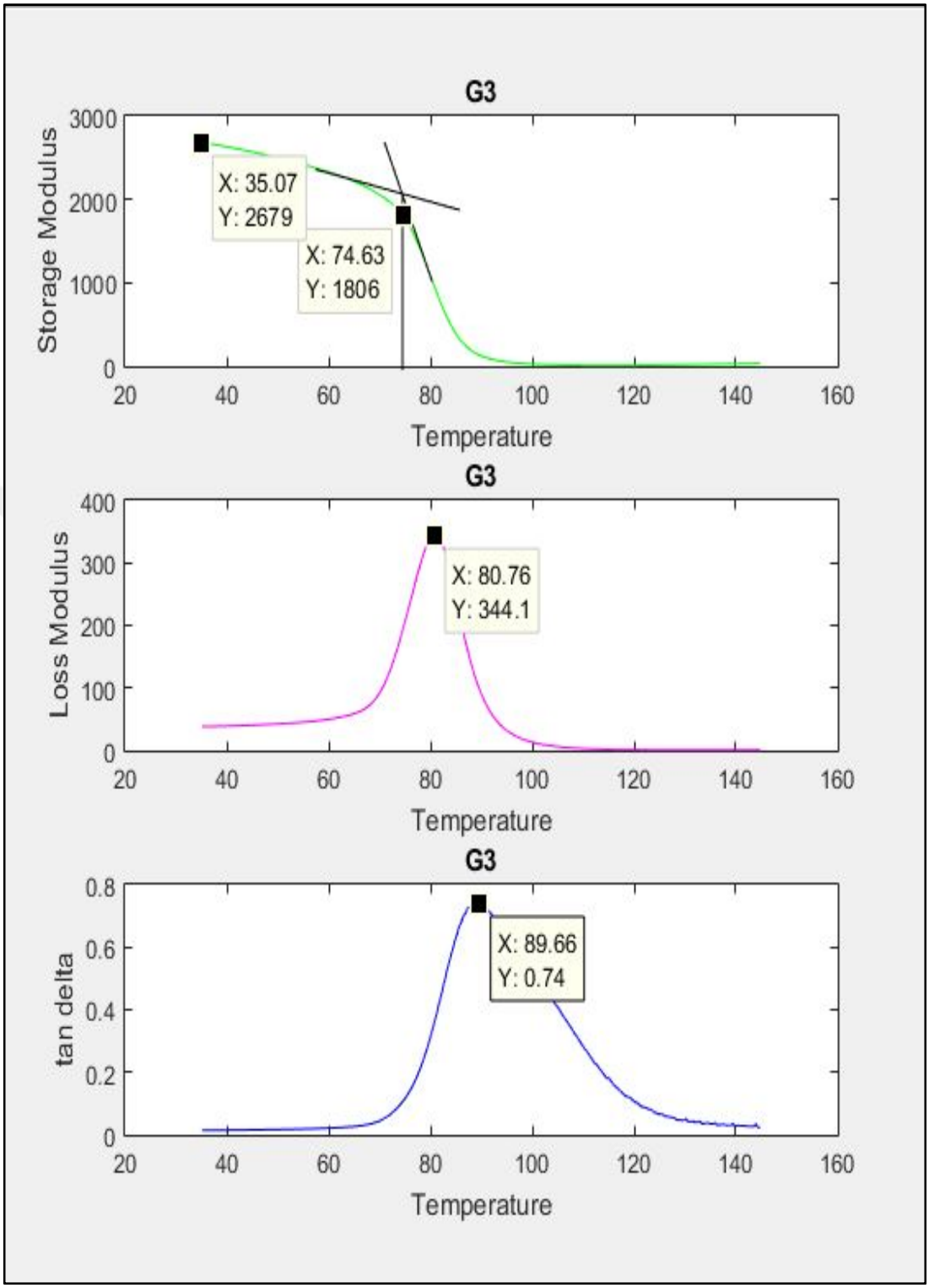

Figure 6.12 Storage modulus, loss modulus and tan δ values of G3

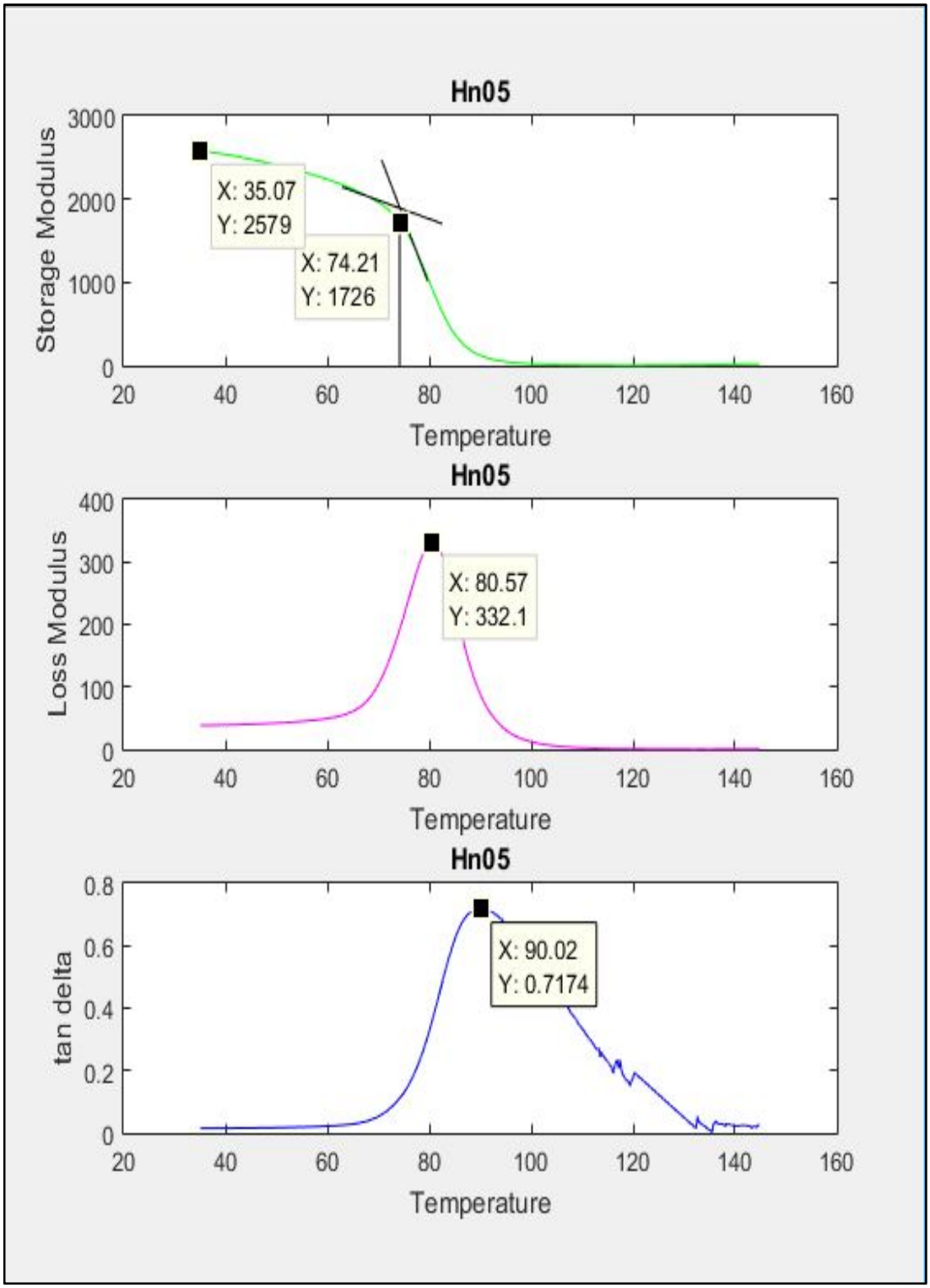

Figure 6.13 Storage modulus, loss modulus and tan δ values of Hn05

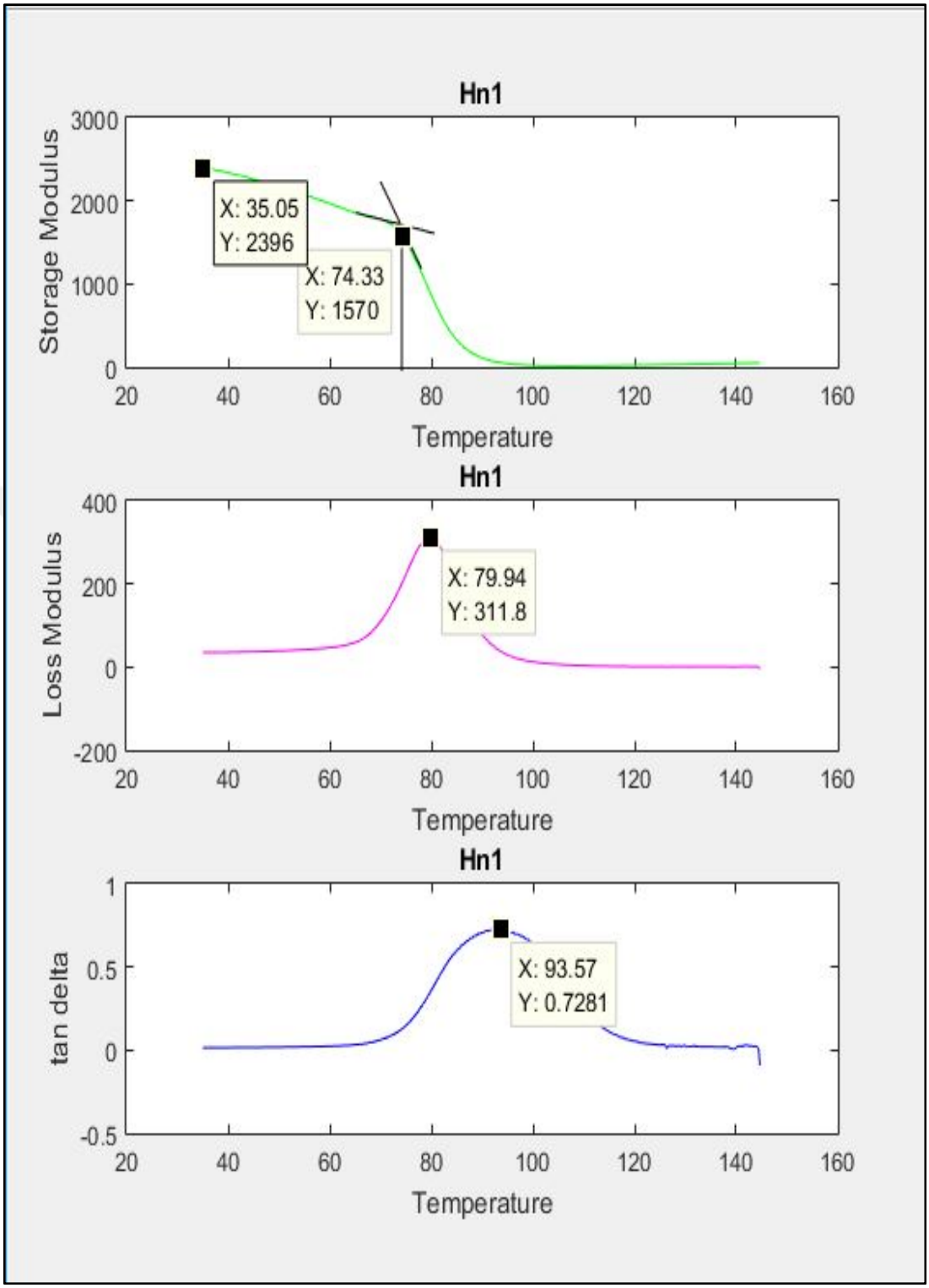

Figure 6.14 Storage modulus, loss modulus and tan δ values of Hn1

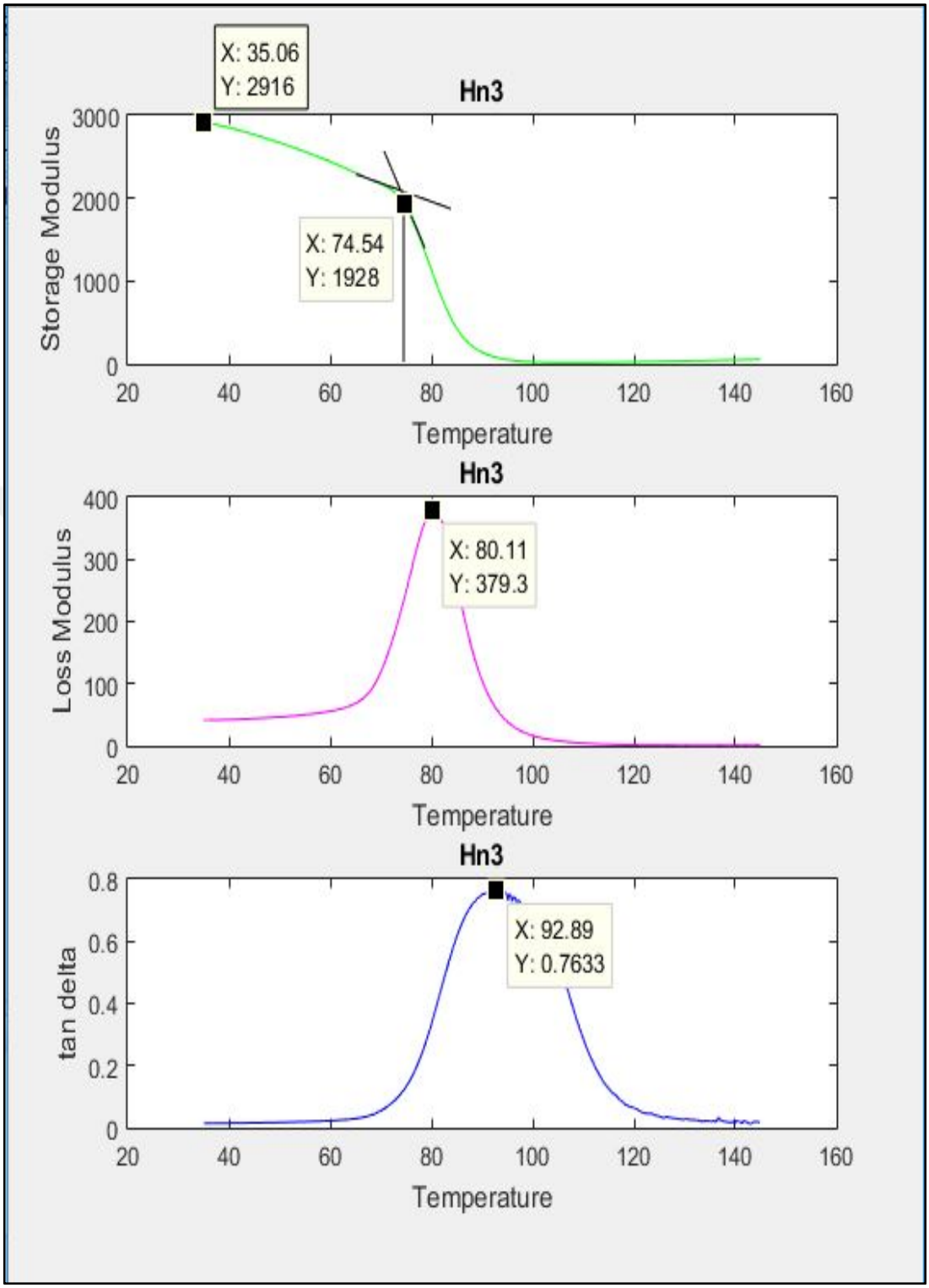

Figure 6.15 Storage modulus, loss modulus and tan δ values of Hn3

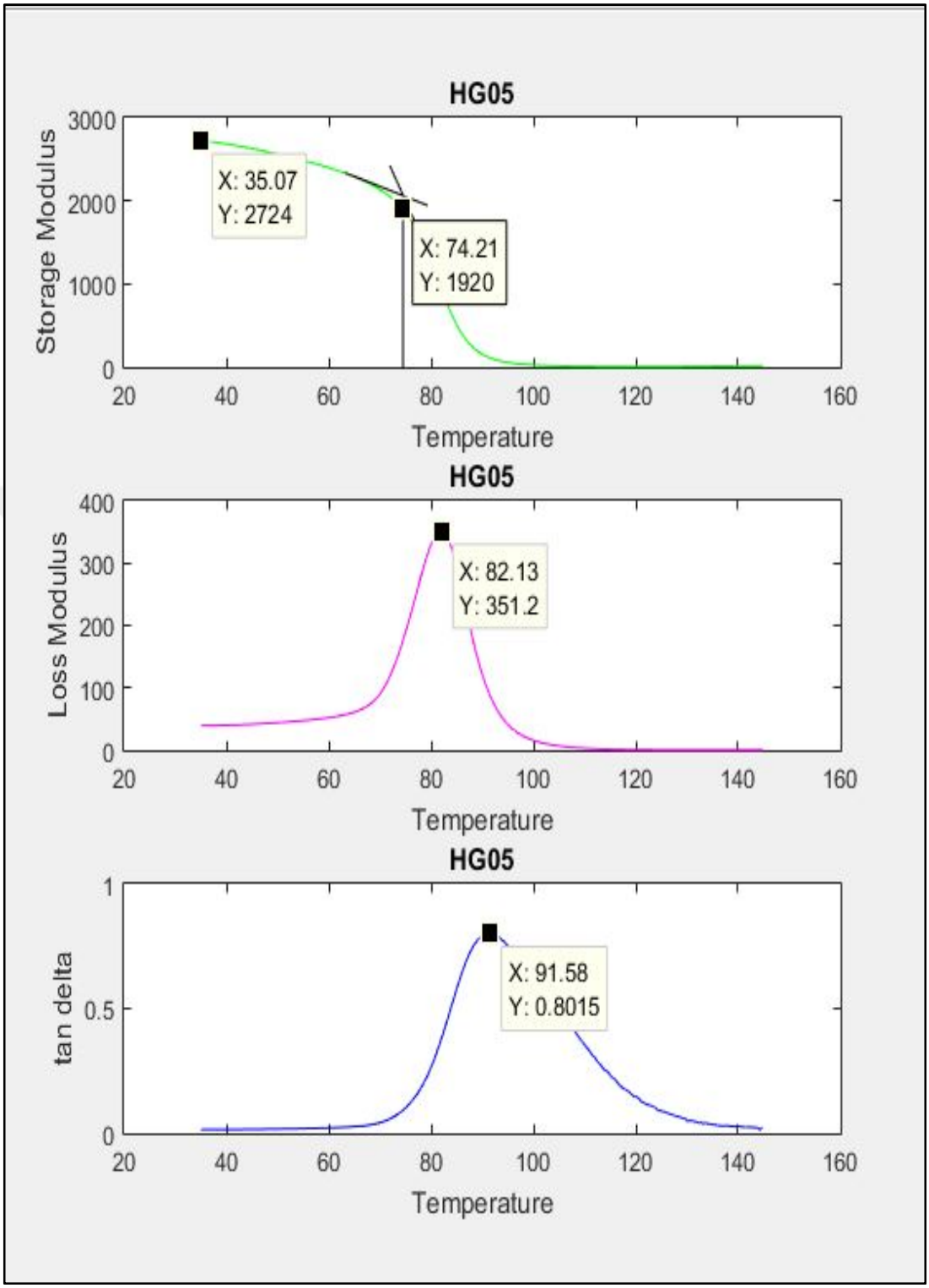

Figure 6.16 Storage modulus, loss modulus and tan δ values of HG05

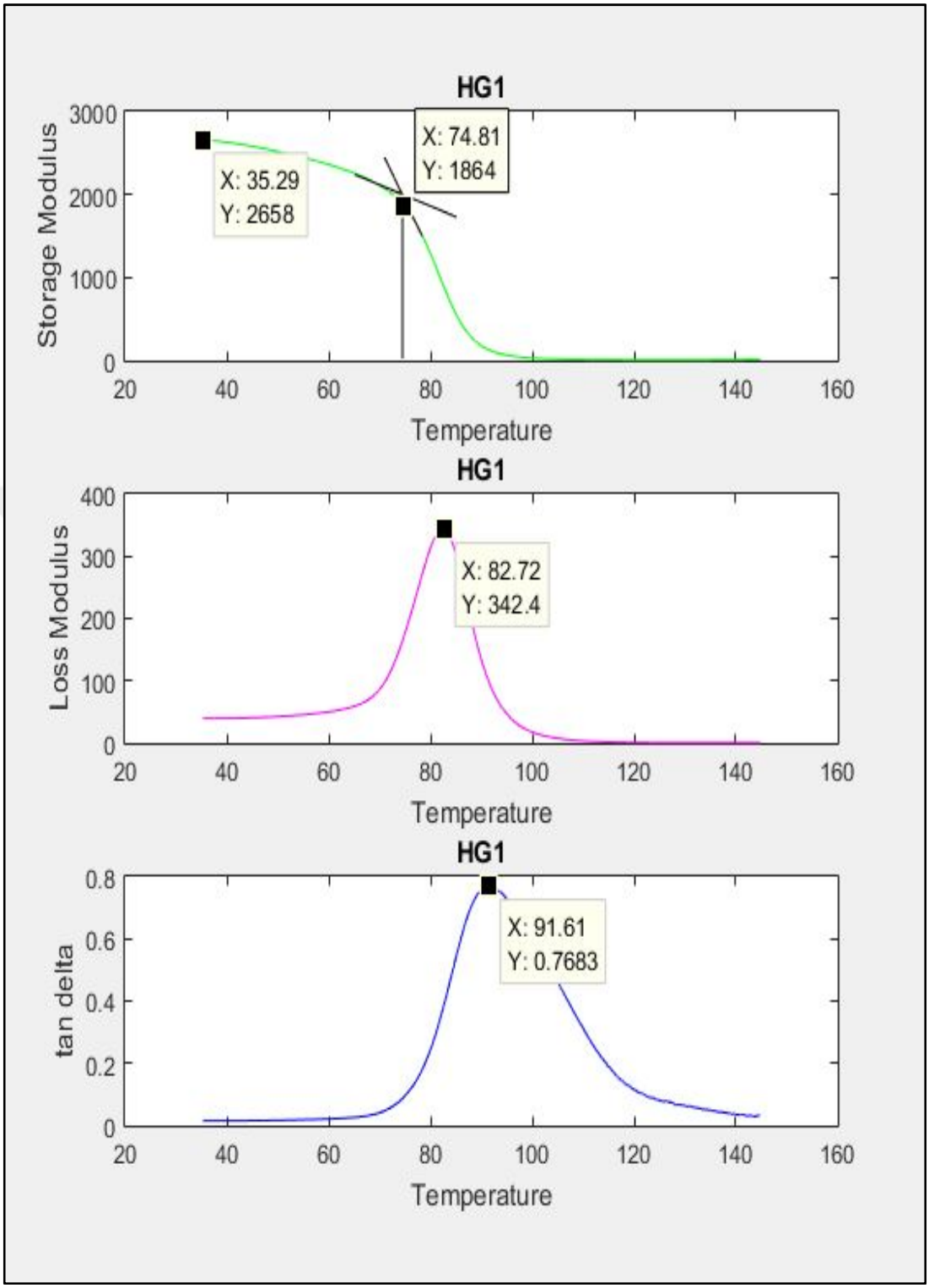

Figure 6.17 Storage modulus, loss modulus and tan δ values of HG1

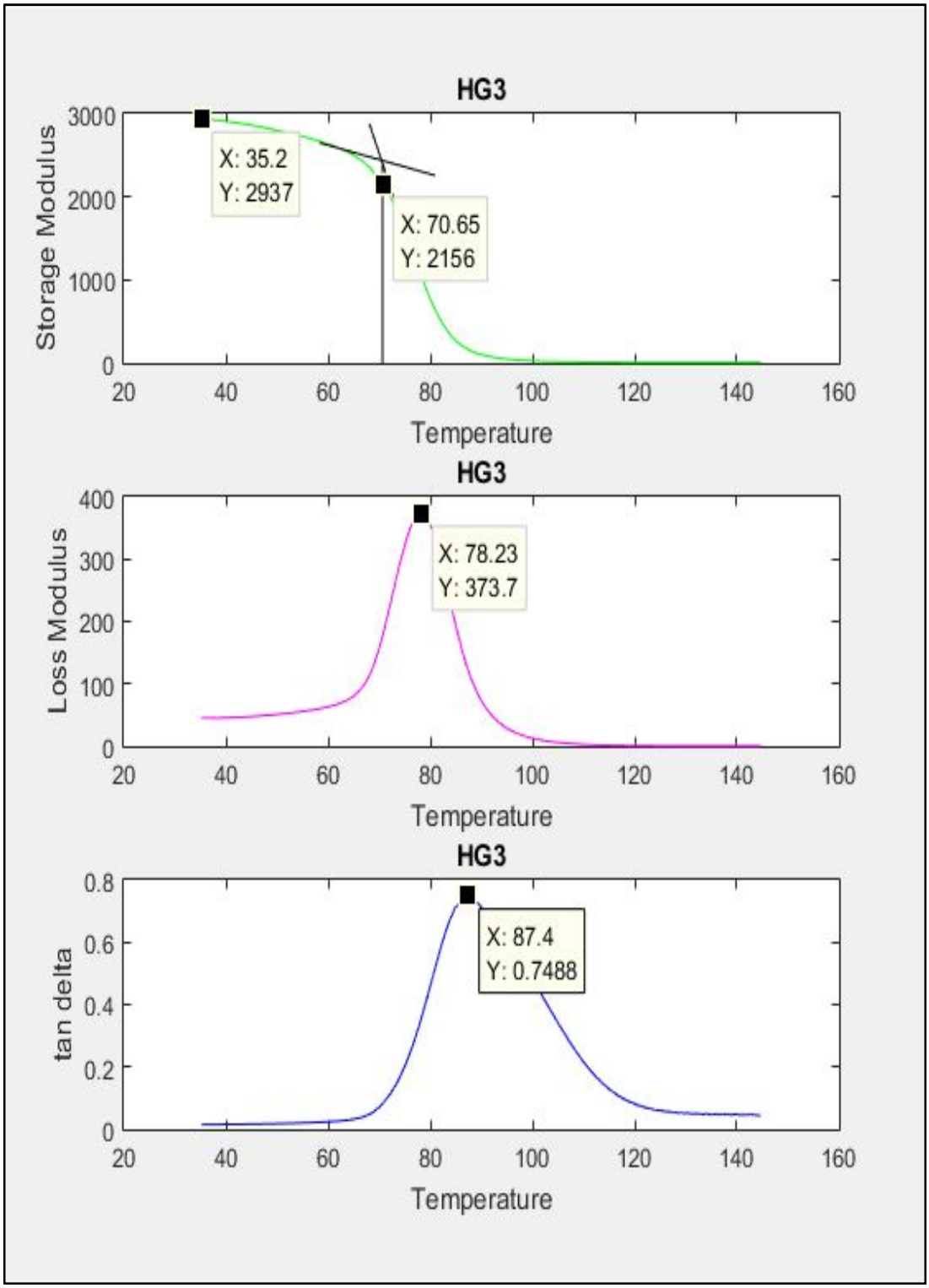

Figure 6.18 Storage modulus, loss modulus and tan δ values of HG3

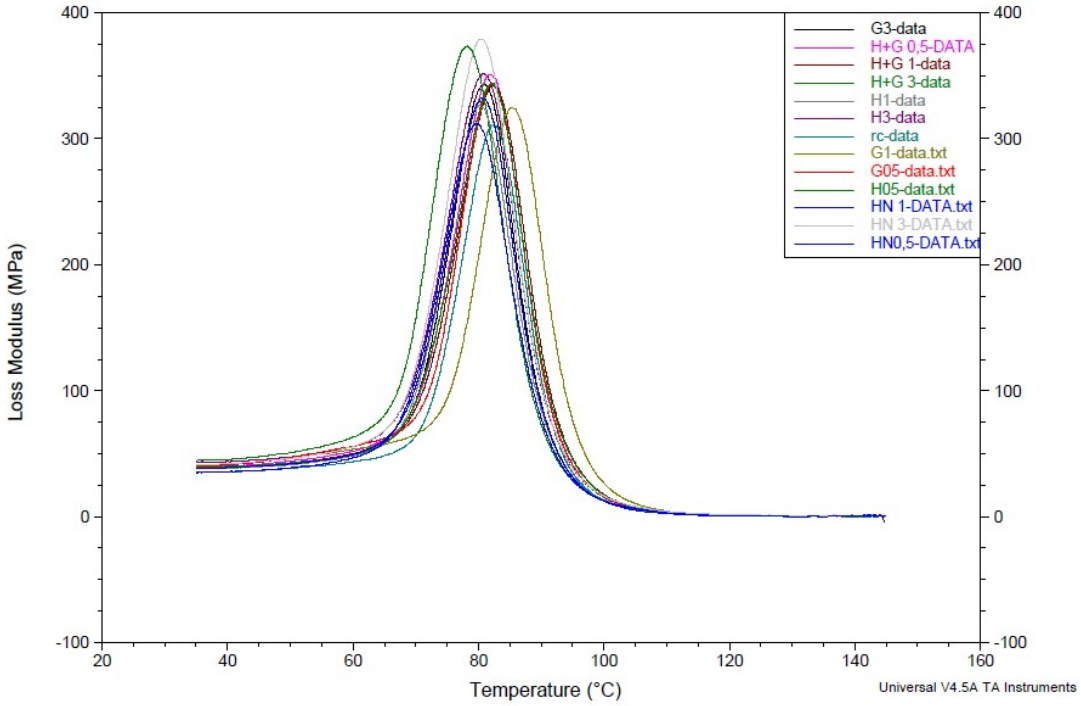

Figure 6.19 Loss modulus values for all specimens

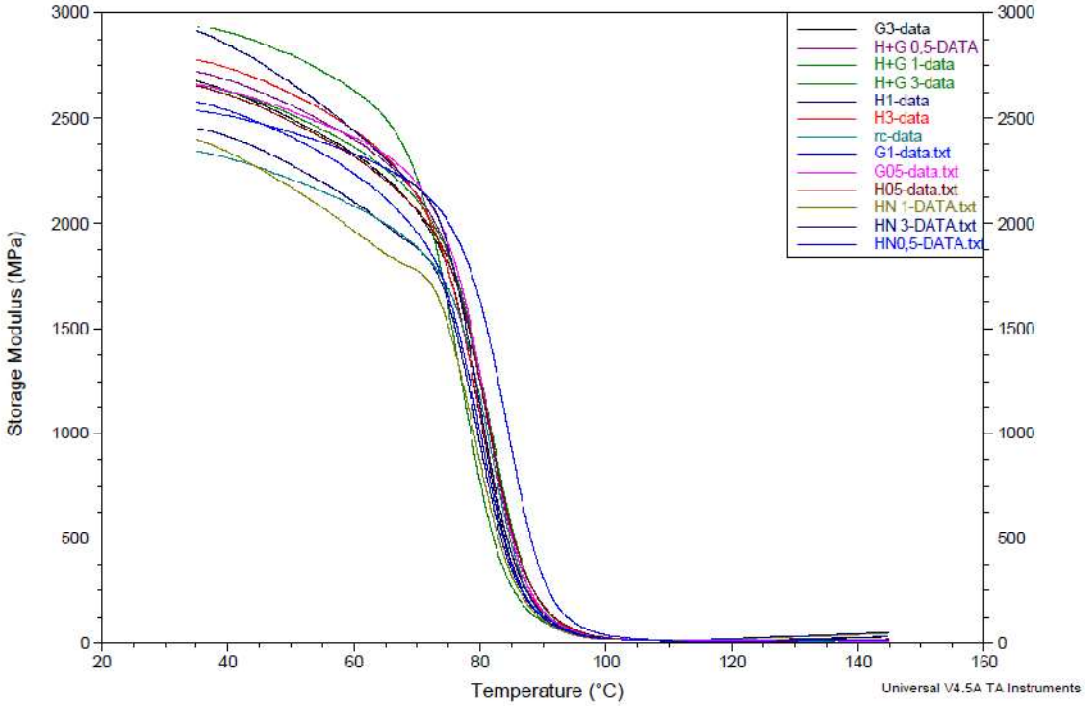

Figure 6.20 Storage modulus values for all specimens

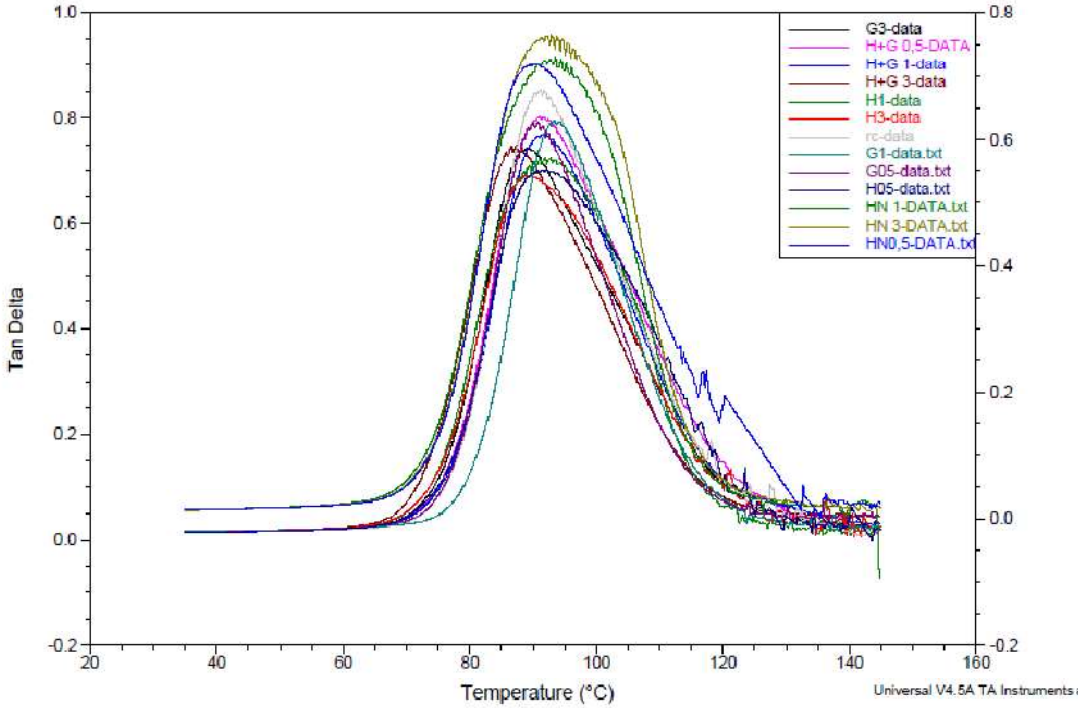

Figure 6.21 Tan δ values for all specimens

6.4 Results of Dynamic Mechanical Analysis

6.4.1 Glass Transition Temperature

Glass transition temperatures were obtained from three different graphics which were storage modulus, loss modulus and tan δ graphics are shown in Figure 19, Figure 20 and Figure 21 for all specimens.

Firstly, glass transition temperatures were determined from Storage modulus – Temperature graphics according to ASTM D7028 standard with intersection method. Due to ambiguity of the drawing lines of intersection, other methods which were maximum value of the tan δ and loss modulus were used. As shown in Table 6.1, glass transition temperature which is obtained from loss modulus - temperature gives more accurate results.

Table 6.1 Glass transition temperature obtained from storage modulus, loss modulus and tan δ graphs

	Glass Transition Temperature (T_g) [°C]		
Specimen	**E'**	**E''**	**tanδ**
RC	76.68	82.32	90.94
H05	75.98	82.36	91.53
H1	75.14	80.25	91.93
H3	73.88	80.71	89.33
G05	75.56	82.51	90.86
G1	76.73	85.10	93.45
G3	74.63	80.76	89.66
Hn05	74.21	80.57	90.02
Hn1	74.33	79.94	93.57
Hn3	74.54	80.11	92.89
HG05	74.21	82.13	91.58
HG1	74.81	82.72	91.61
HG3	70.65	78.23	87.40

The temperature of the resin was found as 82.32 °C that was obtained from the maximum point of loss modulus in DMA analysis. When the specimens catalog is examined, it is seen that the glass transition temperature for the resin is 80-85 °C. This data shows the compatibility of the results between real value and DMA analysis for the resin.

Glass transition temperatures of the specimens are close to each other. But, if the temperature is increased, it will be seen that the graphene mineral that has 1% weight ratio will pass to the rubber zone at last according to other specimens.

The glass transition temperature was also investigated according to mineral weight ratios given in Figure 6.22. There is almost no difference between transition temperatures of the resin and the others at 0.5 wt%. When the investigation of 1 wt%, graphene and mixture of huntite and graphene mineral increased the transition temperature while huntite and huntite nano sized mineral decreased it. Lastly, adding 3 wt% of mineral decresed the glass transition temperature, comparison with pure resin.

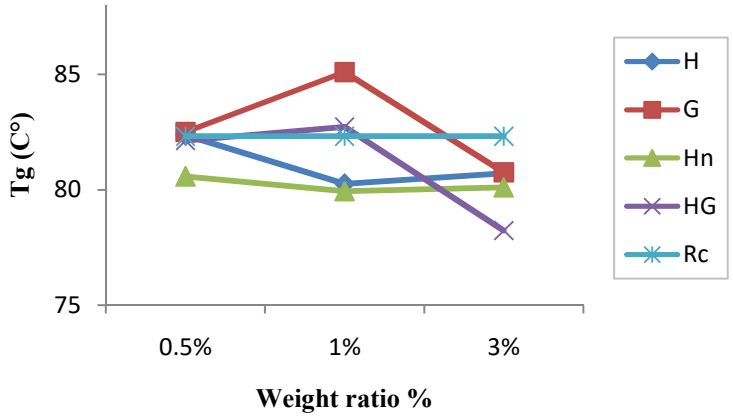

Figure 6.22 Glass transition temperature values according to weight ratios

6.4.2 Storage Modulus and Loss Modulus

Storage modulus and loss modulus values were determined under the 1 Hz frequency. The maximum values of storage modulus and loss modulus is at initial temperature and glass transition temperature, respectively. Loss modulus is related with viscous response and energy dissipated are given for all specimens in Figure 6.23 versus glass transition temperature. According to graphic, pure resin has minimum loss modulus. The reason increased loss modulus with adding mineral is internal friction force between mineral particles and resin. Because this friction force causes internal heat and loss.

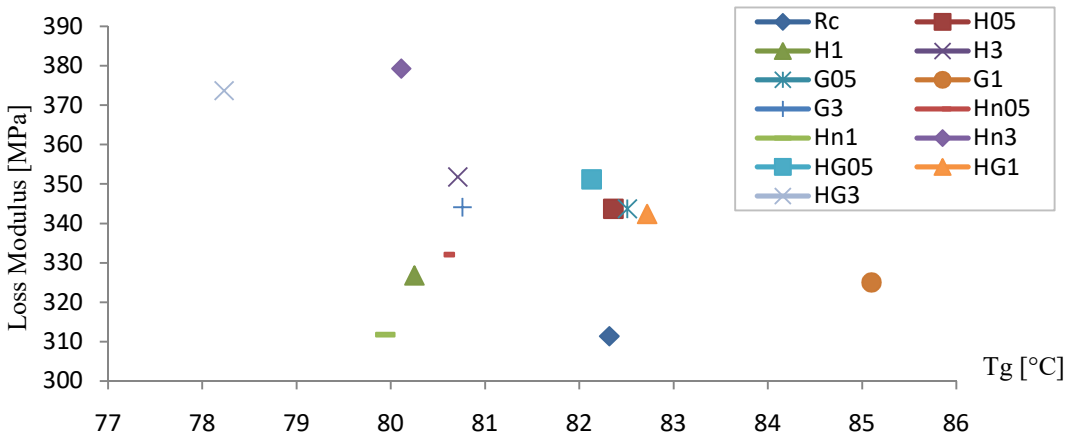

Figure 6.23 Loss modulus and glass transition temperature

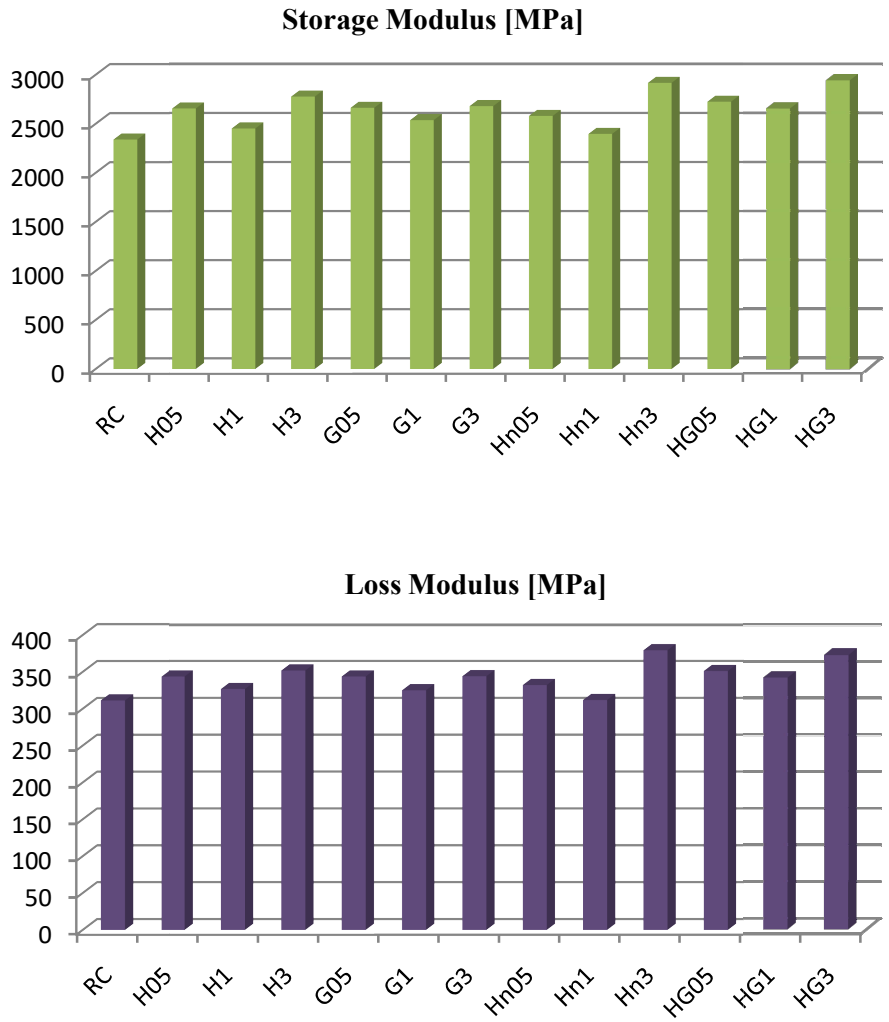

Figure 6.24 (a)Storage modulus and (b)loss modulus values

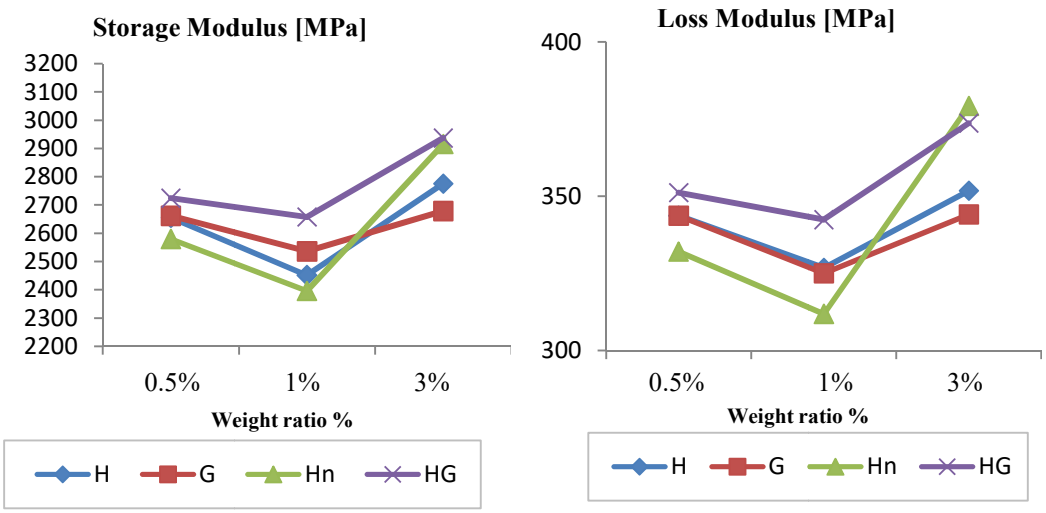

Figure 6.25 Storage modulus and loss modulus values according to weight ratios

When the storage modulus is examined, maximum value occurs at initial temperature (35°C). When the temperature getting increased, stiffness decrease with approaching the rubber field after the transition region. In other words, material has higher stiffness at initial temperature.

Comparison of storage modulus and loss modulus is given in Figure 6.24 and Figure 6.25. Graphs of them are so similar. Minimum value is shown at pure resin at storage modulus and loss modulus. They reach the maximum values at 3% weight ratio where as they reach minimum values at 1% weight ratio.

6.4.3 Tan δ Values

Tan δ is the ratio of loss modulus to storage modulus. Pure epoxy has maximum tan δ value because of molecular mobility. Tan δ values of resin and other specimens at transition temperature are given in Figure 6.26.

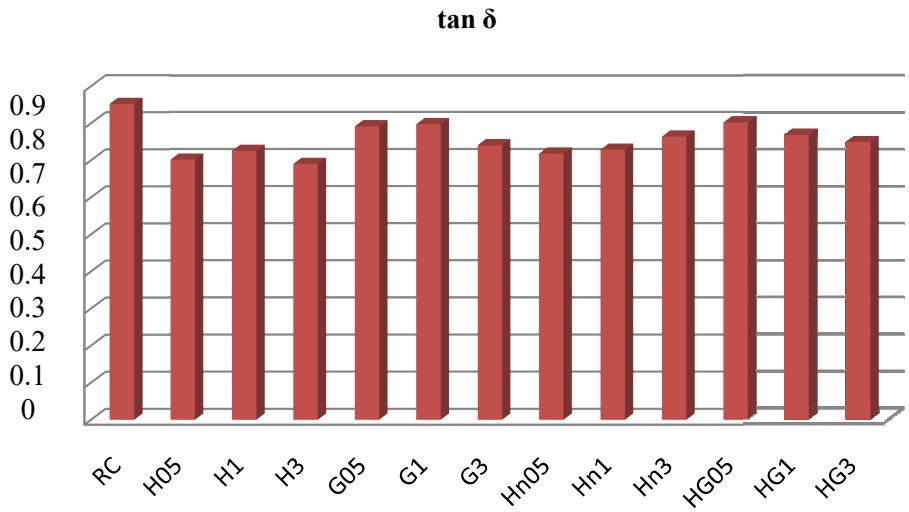

Figure 6.26 Tan δ values

Storage modulus, loss modulus, tan δ and glass transition temperatures were determined for all mineral types and weight ratios. These values were presented in Table 6.2

Table 6.2 Glass transition temperature, storage modulus, loss modulus and tan δ values

	T_g [°C]	Storage Modulus[MPa]	Loss Modulus[MPa]	tan δ
RC	82.32	2341	311.4	0.8527
H05	82.36	2655	343.7	0.7013
H1	80.25	2451	326.8	0.7248
H3	80.71	2776	351.8	0.6897
G05	82.51	2662	343.7	0.7910
G1	85.10	2536	325.0	0.7967
G3	80.76	2679	344.1	0.7400
Hn05	80.57	2579	332.1	0.7174
Hn1	79.94	2396	311.8	0.7281
Hn3	80.11	2916	379.3	0.7633
HG05	82.13	2724	351.2	0.8015
HG1	82.72	2658	342.4	0.7683
HG3	78.23	2937	373.7	0.7488

CHAPTER SEVEN
VIBRATION ANALYSIS

7.1 Vibration

Vibration is related with the repeated movement or oscillatory motions of bodies relative to a equilibrium position. Figure 7.1 shows the oscillatory motion (Rao, 2011).

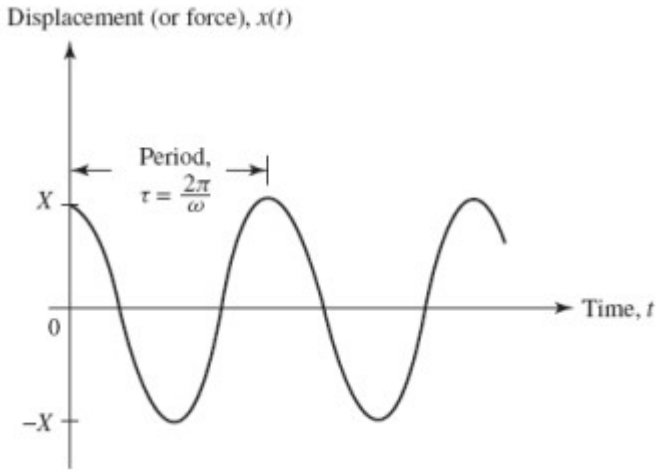

Figure 7.1 Oscillatory motion (Rao, 2011)

Vibration can be classified differently and main classification is given below.

7.1.1 Free and Forced Vibration

Free vibration is self vibration without external force at a system after the first disturbance. As opposed to the free vibration, in forced vibration, the external force acts on the system and causes vibration. When the frequency of vibration is equal with the natural frequencies of the system, resonance occurs and big failures emerge at the system (Rao, 2011).

7.1.2 Undamped and Damped Vibration

Vibration is known as undamped vibration if there is no energy loss during oscillation. If the system loses the energy, it is called damped vibration. In the analysis of vibrating systems close to the resonance, consideration of the damping is extremely important (Rao, 2011).

7.1.3 Linear and Nonlinear Vibration

When vibration elements such as mass, spring, damper act linear behavior, they are caused vibrations that are called linear vibrations. While vibration elements behave nonlinearly, the vibration is called nonlinear vibration (Rao, 2011).

7.2 Building a Beam Model

There are various elements that provide potential and kinetic energy storing and energy damping in damped systems. Structural elements in vibrating mechanical systems often act as spring elements. Beam type elements are examples of this type of structural elements. In Figure 7.2, beam subjected to bending was modeled as a spring. Spring constant was formulized in Equation 7.3 (Rao, 2011).

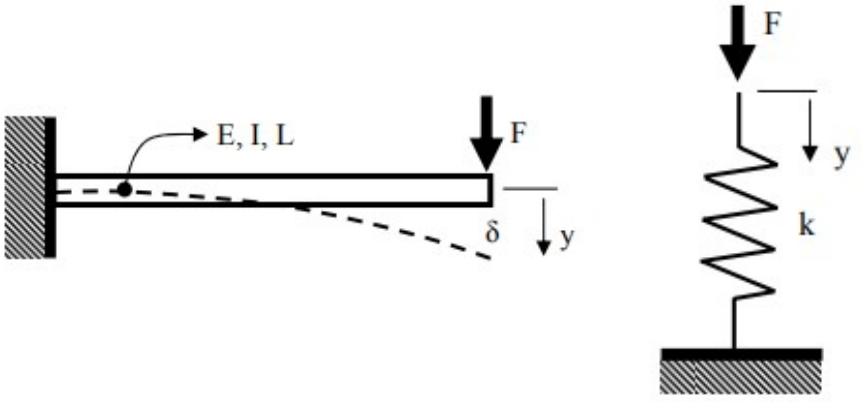

Figure 7.2 Beam subjected to bending is modeled as a spring (Rao, 2011)

$$EI\frac{\partial^2 y}{\partial x^2}M(x) \tag{7.1}$$

$$\delta = \frac{FL^3}{3EI} \tag{7.2}$$

$$\mathrm{k} = \frac{F}{\delta} = \frac{L^3}{3E} \tag{7.3}$$

7.3 Undamped System

7.3.1 Harmonic Motion

Periodic motion might repeat itself regularly at equal time intervals. The undamped and simpliest type of periodic motion is harmonic motion which is shown in Figure 7.3 (Rao, 2011).

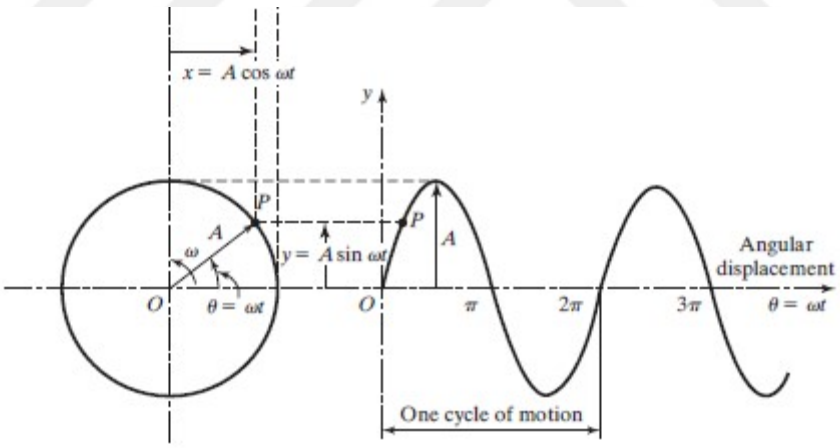

Figure 7.3 Harmonic motion (Rao, 2011)

For harmonic motion; displacement, velocity and acceleration were expressed as equations 7.4, 7.5 and 7.6 respectively (Rao, 2011).

$$X = A\sin\theta = A\sin\omega t \tag{7.4}$$

$$Y = A\cos\theta = A\cos\omega t \tag{7.5}$$

$$V = \frac{dX}{dt} = A\cos\theta = \omega A\cos\omega t \tag{7.6}$$

$$a = \frac{d^2X}{dt^2} = -\omega^2 A\sin\omega t = -\omega^2 x \tag{7.7}$$

Thus Equation (7.4 and 7.5) can be expressed as;

$$\overrightarrow{X} = A(\cos\theta + i\sin\theta) = Ae^{i\theta} \tag{7.8}$$

$$\overrightarrow{X} = A(\cos\omega t + i\sin\omega t) = Ae^{i\omega t} \tag{7.9}$$

7.3.1.1 Definitions

Amplitude: Displacement of a vibrating system between the peak point and equilibrium positions is called the amplitude of vibration.

Period of oscillation: The time taken to complete one cycle of motion is known as the period of oscillation or time period. It is indicated by T.

$$T = \frac{2\pi}{\omega} \tag{7.10}$$

Frequency of oscillation: The number of cycles per unit time is called the frequency of oscillation. It is indicated by f. ω is the circular frequency (Rao, 2011).

$$f = \frac{1}{T} = \frac{\omega}{2\pi} \tag{7.11}$$

7.3.1.2 Harmonic Motion Analysis and Fourier Series

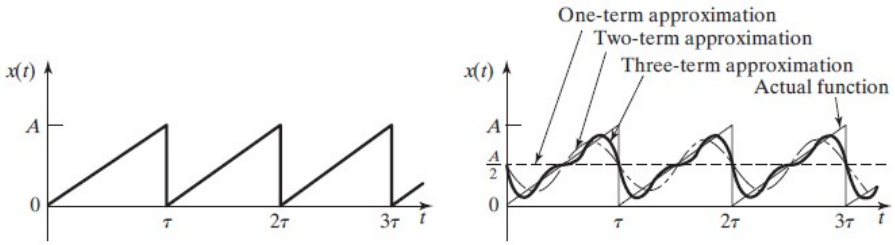

Figure 7.4 Periodic function (Rao, 2011)

Some systems may behave as periodic function response not harmonic response. In that case, periodic functions may be denoted by sum of the harmonic functions using Fourier series represented as Figure 7.4 (Rao, 2011).

$$X(t) = \frac{a_0}{2} + \sum_{n=1}^{\infty}(a_n \cos n\omega t + b_n \sin n\omega t) \tag{7.12}$$

$$a_0 = \frac{2}{T} + \int_0^T x(t)dt \tag{7.13}$$

$$a_n = \frac{2}{T} + \int_0^T x(t)\cos n\omega t\, dt \tag{7.14}$$

$$b_n = \frac{2}{T} + \int_0^T x(t)\sin n\omega t\, dt \tag{7.15}$$

In complex notation;

$$X(t) = \sum_{-\infty}^{\infty} c_n e^{in\omega t} \tag{7.16}$$

$$c_n = \frac{1}{T} + \int_0^T x(t)\, e^{-in\omega t}\, dt \tag{7.17}$$

7.4 Damped System

Assumption: $$x(t) = Ce^{st} \tag{7.18}$$

$$m\ddot{x} + c\dot{x} + kx = 0 \tag{7.19}$$

$$ms^2 + cs + k = 0 \tag{7.20}$$

Roots of the Equation 7.20:

$$s_{1,2} = \frac{-c \pm \sqrt{c^2-4mk}}{2m} = \frac{-c}{2m} \pm \pm \sqrt{(\frac{c}{2m})^2 - \frac{k}{m}} \tag{7.21}$$

$$x(t) = C_1 e^{s_1 t} + C_2 e^{s_2 t} \tag{7.22}$$

$$x(t) = C_1 e^{\frac{-c}{2m} \pm \pm \sqrt{(\frac{c}{2m})^2 - \frac{k}{m}}} + C_2 e^{\frac{-c}{2m} \pm \pm \sqrt{(\frac{c}{2m})^2 - \frac{k}{m}}} \tag{7.23}$$

$$(\frac{c_c}{2m})^2 - \frac{k}{m} = 0 \tag{7.24}$$

$$c_c = 2m\sqrt{\frac{k}{m}} = 2m\,\omega_n \tag{7.25}$$

$$\frac{c}{c_c} = \xi \tag{7.26}$$

$$\frac{c}{2m} = \frac{c}{c_c} \cdot \frac{c_c}{2m} = \xi\,\omega_n \tag{7.27}$$

$$s_{1,2} = (-\xi \pm \sqrt{\xi^2 - 1})\,\omega \tag{7.28}$$

$$x(t) = C_1 e^{(-\xi + \sqrt{\xi^2-1})\omega t} + C_2 e^{(-\xi - \sqrt{\xi^2-1})\omega t} \tag{7.29}$$

7.4.1 Logarithmic Decrement

The logarithmic decrement method is used to determine the damping ratio of a mechanical system. It is measured the reduction rate of the oscillation amplitudes in the free vibrations of the system (Rao, 2011).

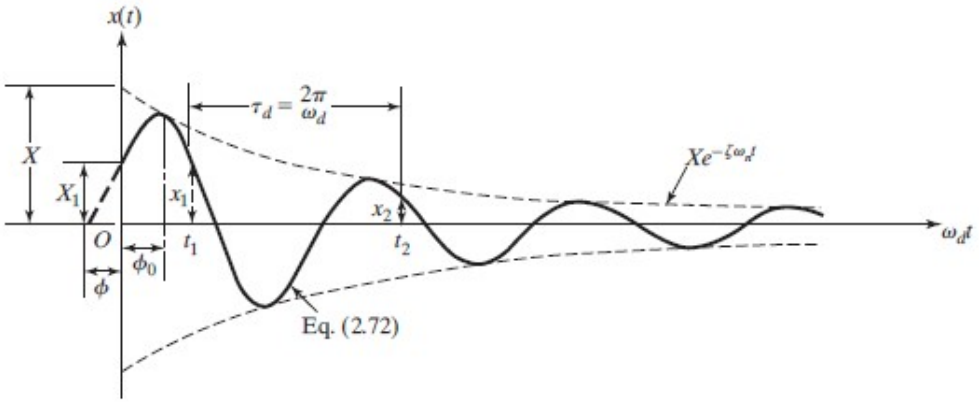

Figure 7.5 Damped solution

For underdamped system ($\xi < 1$) vibration response is:

$$x(t) = Ae^{-\xi\omega_n t}\sin(\omega_d t) \tag{7.30}$$

$$\delta = \ln\frac{x_1}{x_2} = \ln\frac{Ae^{-\xi\omega_n t_1}cos\,(\omega_d t_{\,1} - \varphi)}{Ae^{-\xi\omega_n t_2}cos\,(\omega_d t_{\,2} - \varphi)} \tag{7.31}$$

$$t_2 = t_1 + T \tag{7.32}$$

$$T = \frac{2\pi}{\omega_d} \tag{7.33}$$

$$\omega_d = \sqrt{1-\xi^2}\,\omega_n \tag{7.34}$$

$$\frac{x_1}{x_2} = \frac{e^{-\xi\omega_n t_1}}{e^{-\xi\omega_n(t_1+T)}} = e^{\xi\omega_n T} \tag{7.35}$$

$$\delta = \ln\frac{x_1}{x_2} = \xi\omega_n T = \frac{2\pi\xi}{\sqrt{1-\xi^2}} \quad (7.36)$$

7.5 Experimental Analysis

The effects of mineral types and weight ratios on damping ratios and natural frequencies were investigated experimentally. National Instruments NI PXI-1031 Data Logger was used to collect data of the composite specimens, as shown in Figure 7.6. The specimens which have 25 x 5 x 0.3 cm^3 dimension were formed with Mold 1 having big cavity were used for analysis. Firstly, specimens were marked as 30 mm from the bottom line for fixig the clamp. The specimens were schematized in Figure 7.7. Shaded area refers to the fixed part. Then, two accelerometer were bonded on the marked line.

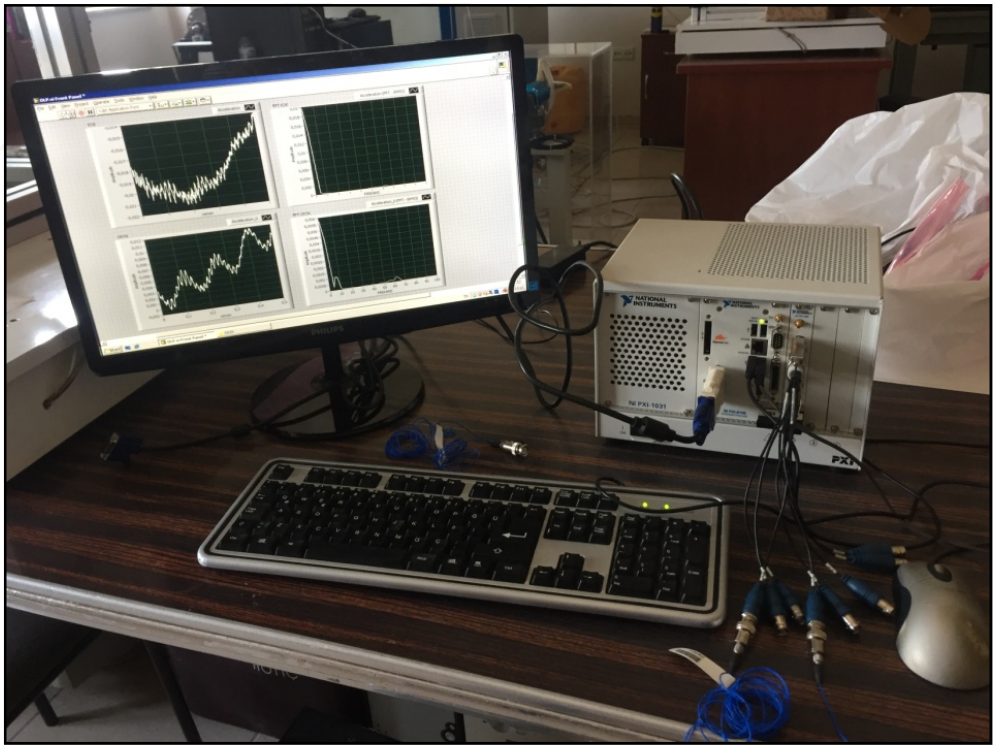

Figure 7.6 Experimental setup (Personal archive, 2018)

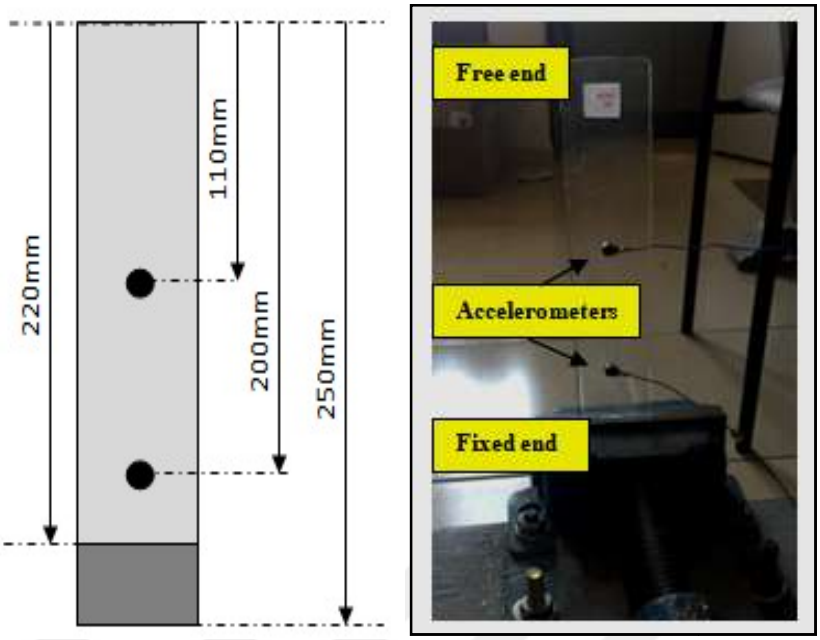

Figure 7.7 Specimen dimensions (Personal archive, 2018)

In order to determine the damping ratios and natural frequencies of the specimens, both impact and free vibration were implemented. Then, response data were processed using Matlab 2015 with function of Fast Fourier Transform (FFT) method. Number of sampling frequency (Fs) was taken as 2000 and length of signal was taken as data length for each specimens. Next, graphs were created so the effects of mineral types and weight ratios on damping ratios and natural frequency values were obtained experimentally. Natural frequency responses of all specimens can be seen in figures graphically from Figure 7.10 to Figure 7.22. Experimental test setup is shown in Figure 7.8 and Figure 7.9.

Figure 7.8 Free vibration (Personal archive, 2018)

Figure 7.9 Application of impulse (Personal archive, 2018)

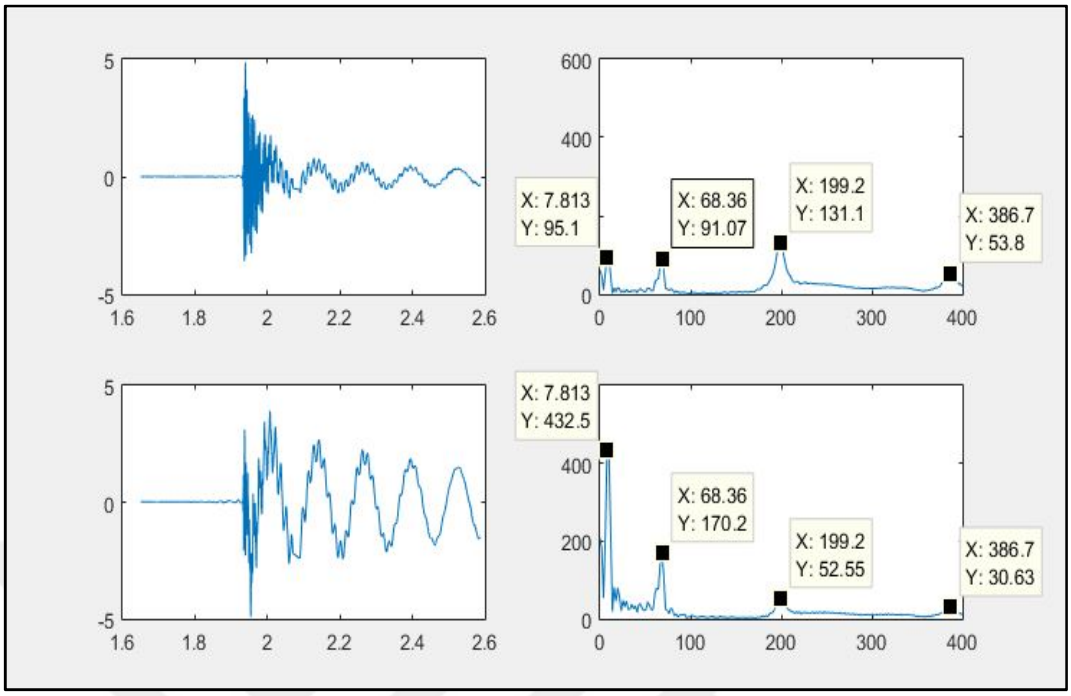

Figure 7.10 Frequency values of Rc specimen (Personal archive, 2018)

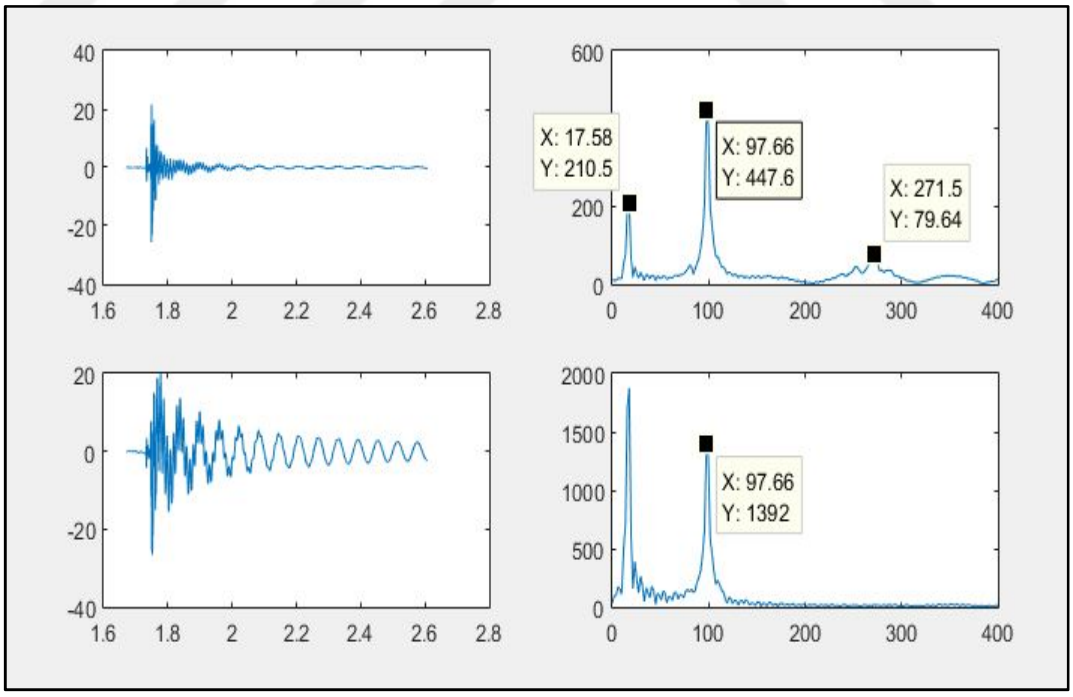

Figure 7.11 Frequency values of H05 specimen (Personal archive, 2018)

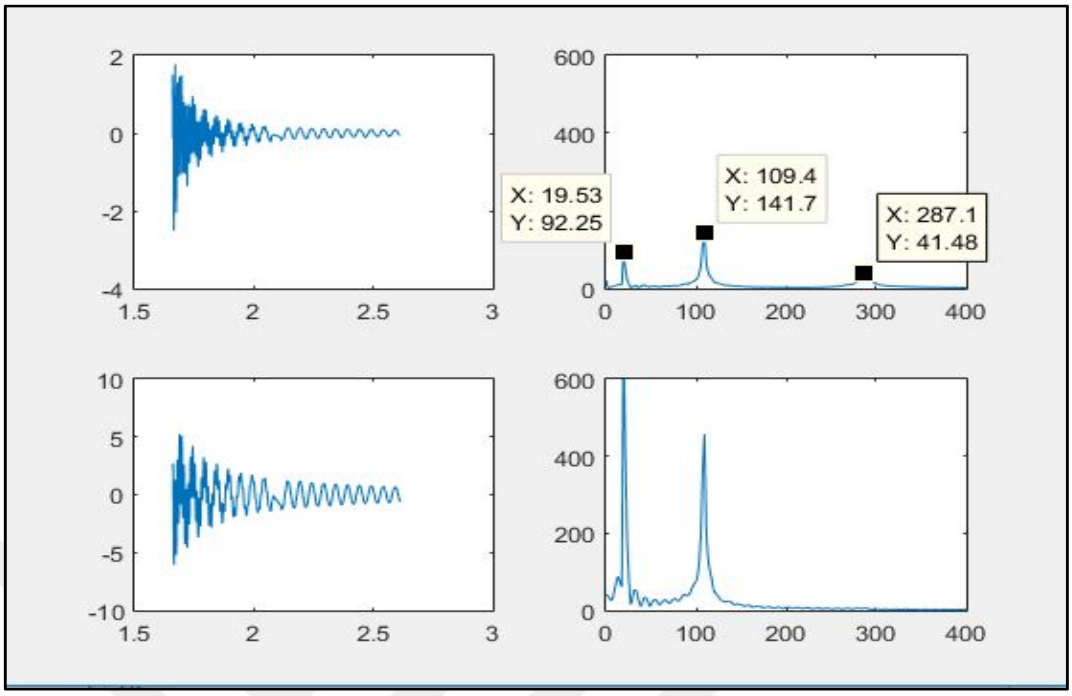

Figure 7.12 Frequency values of H1 specimen (Personal archive, 2018)

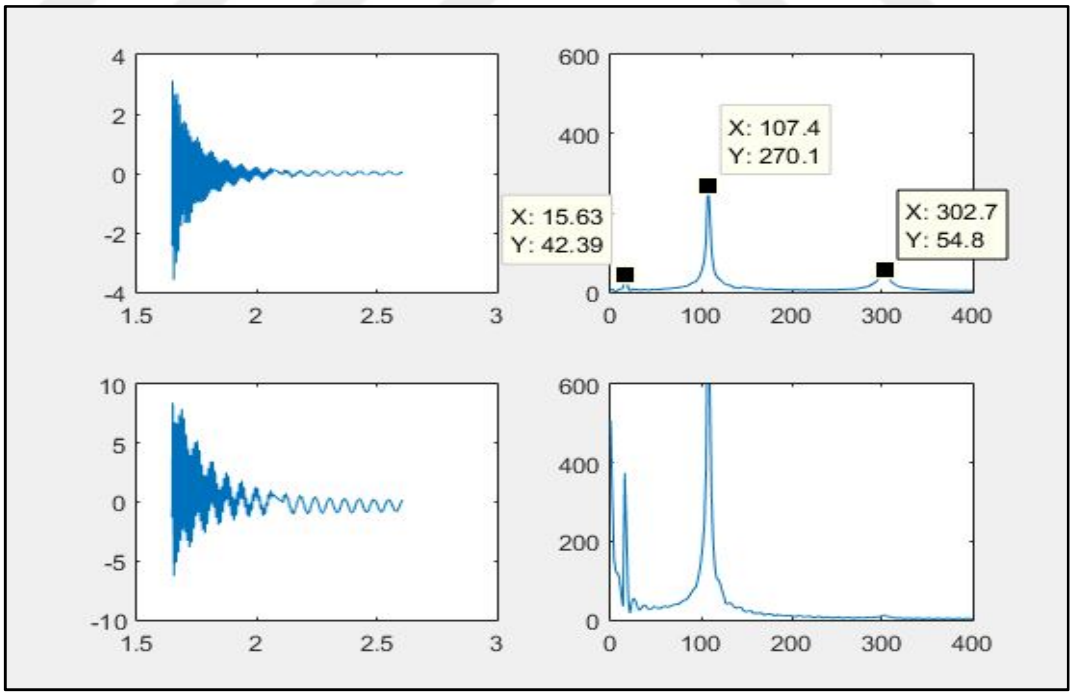

Figure 7.13 Frequency values of H3 specimen (Personal archive, 2018)

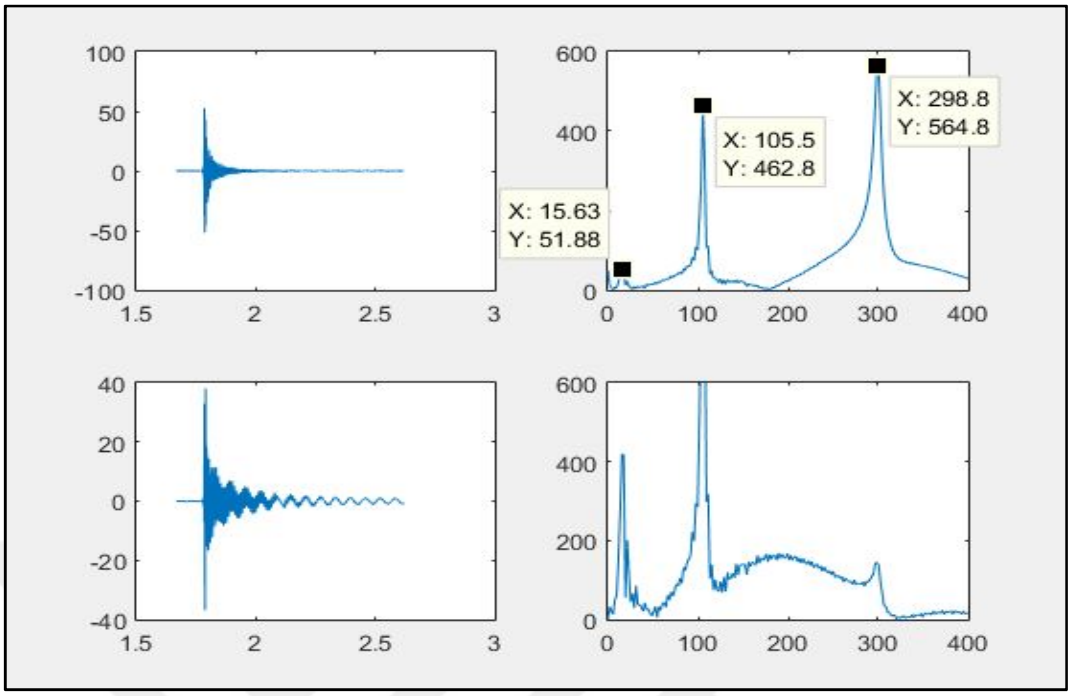

Figure 7.14 Frequency values of G05 specimen (Personal archive, 2018)

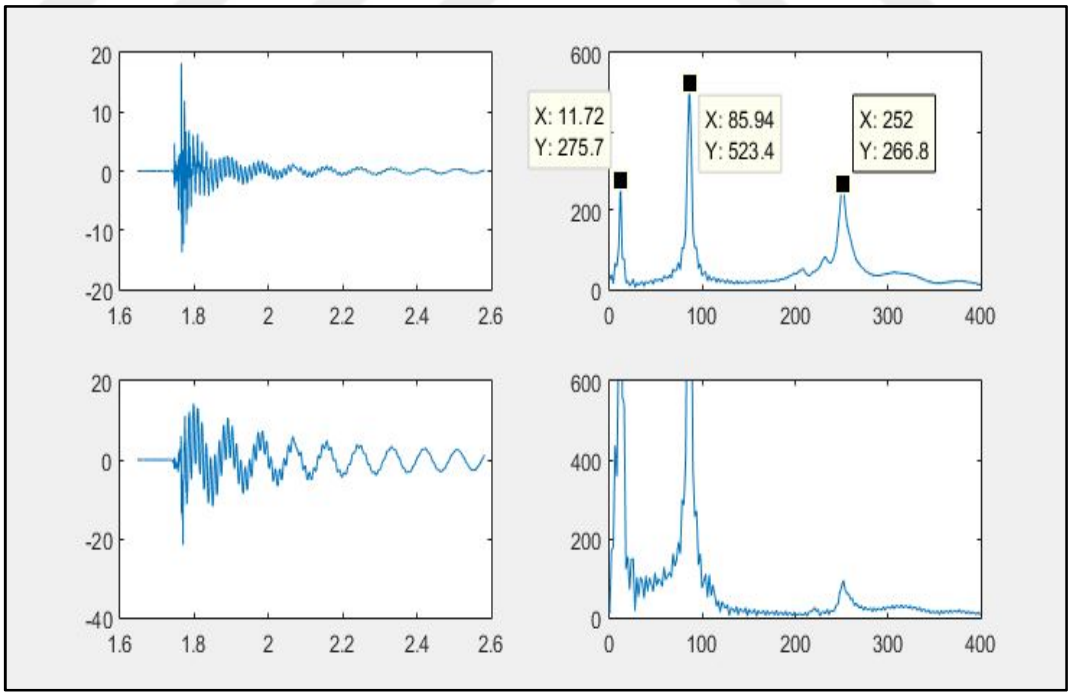

Figure 7.15 Frequency values of G1 specimen (Personal archive, 2018)

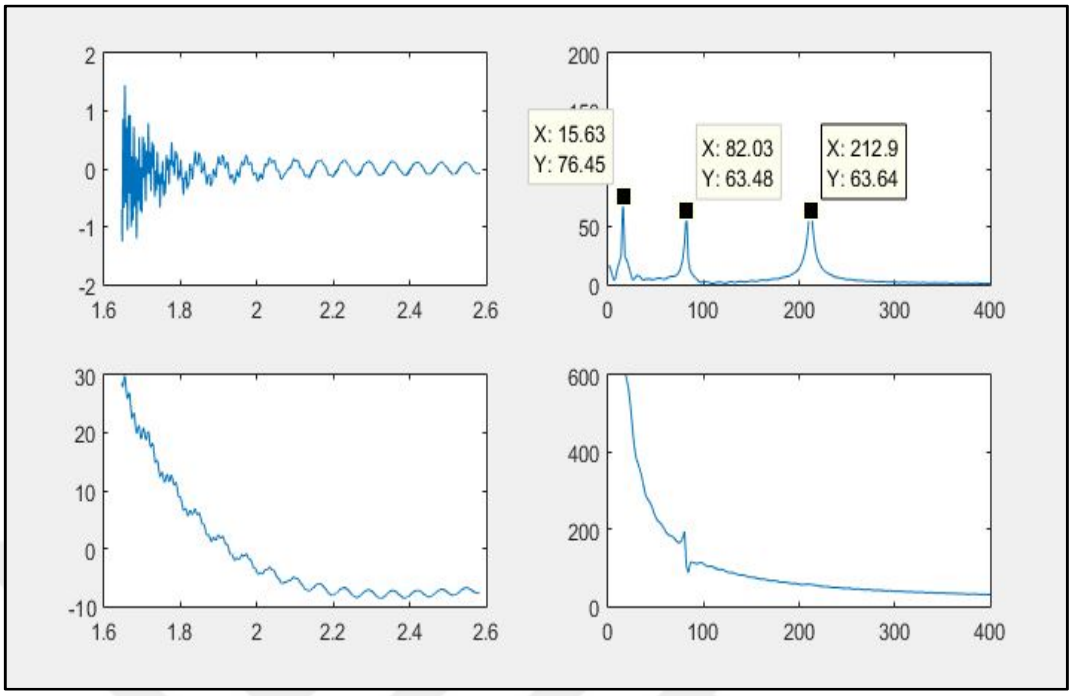

Figure 7.16 Frequency values of G3 specimen (Personal archive, 2018)

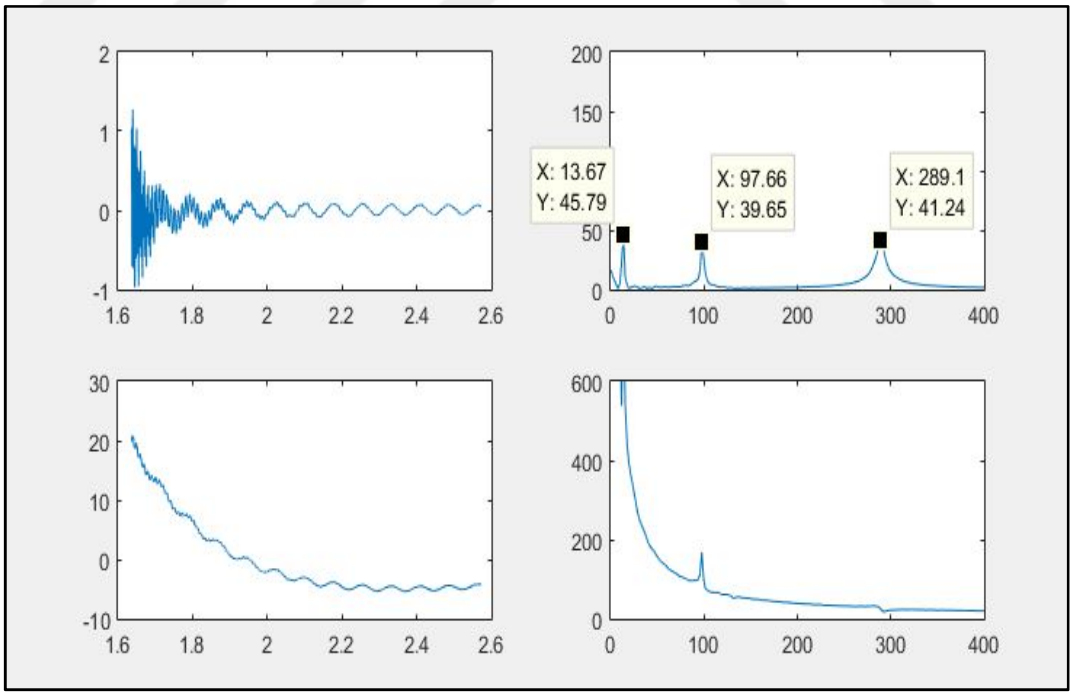

Figure 7.17 Frequency values of Hn05 specimen (Personal archive, 2018)

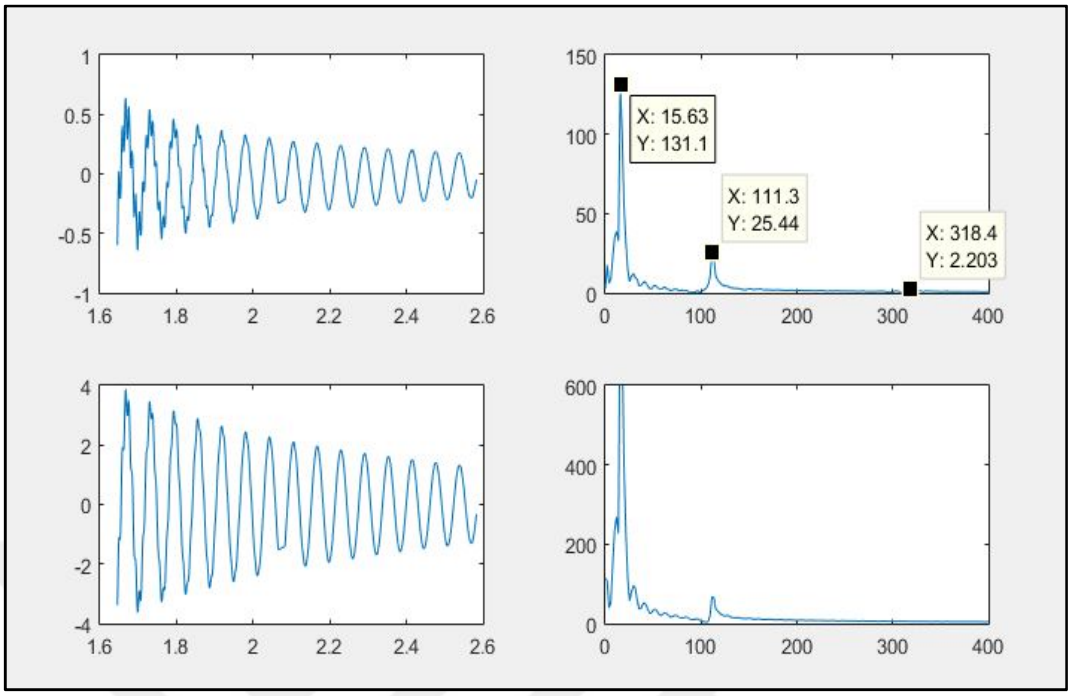

Figure 7.18 Frequency values of Hn1 specimen (Personal archive, 2018)

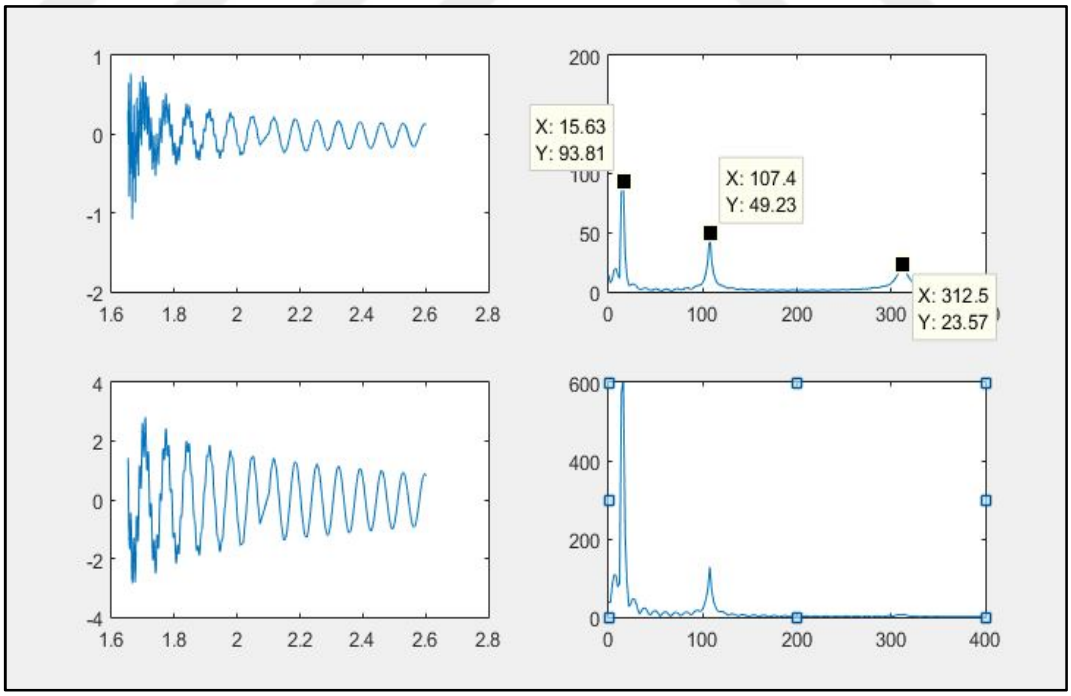

Figure 7.19 Frequency values of Hn3 specimen (Personal archive, 2018)

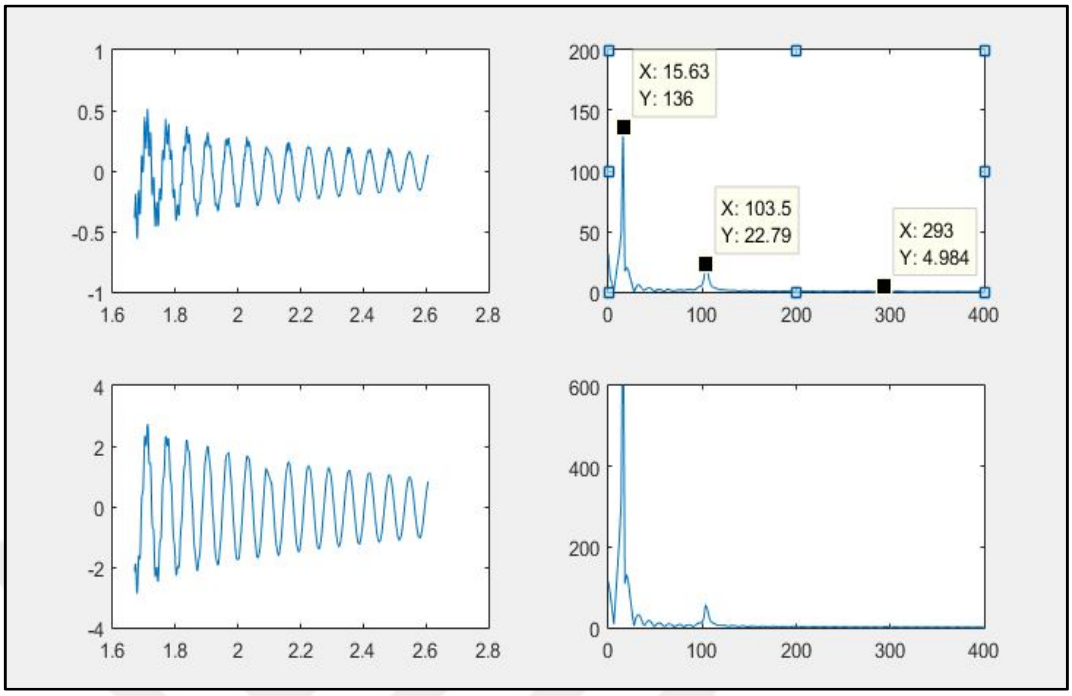

Figure 7.20 Frequency values of HG05 specimen (Personal archive, 2018)

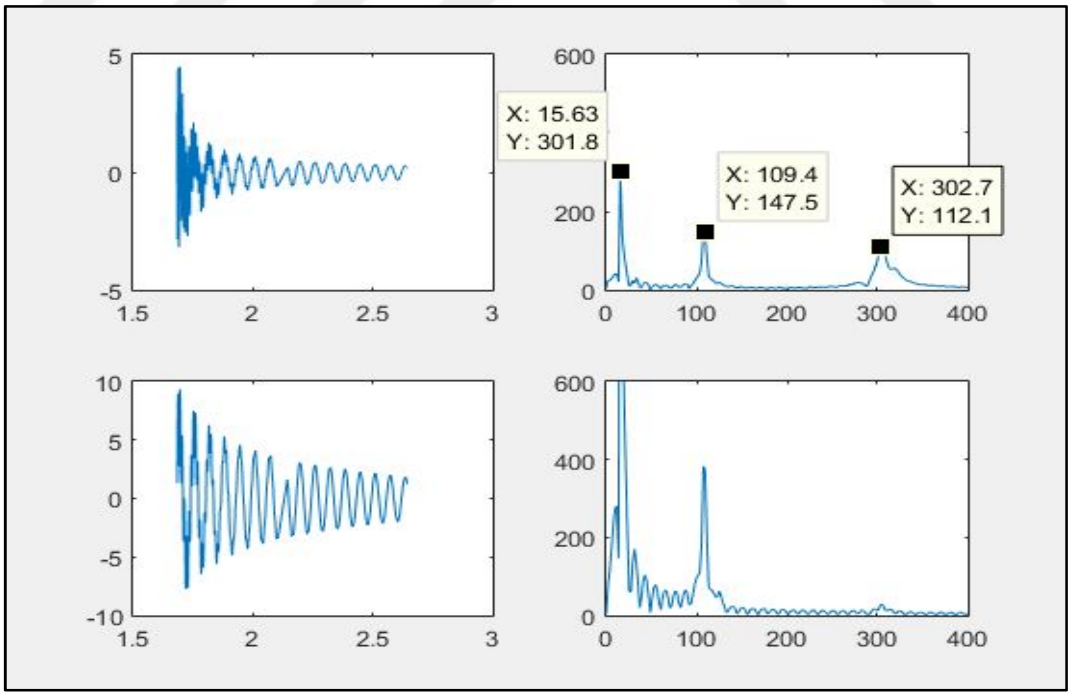

Figure 7.21 Frequency values of HG1 specimen (Personal archive, 2018)

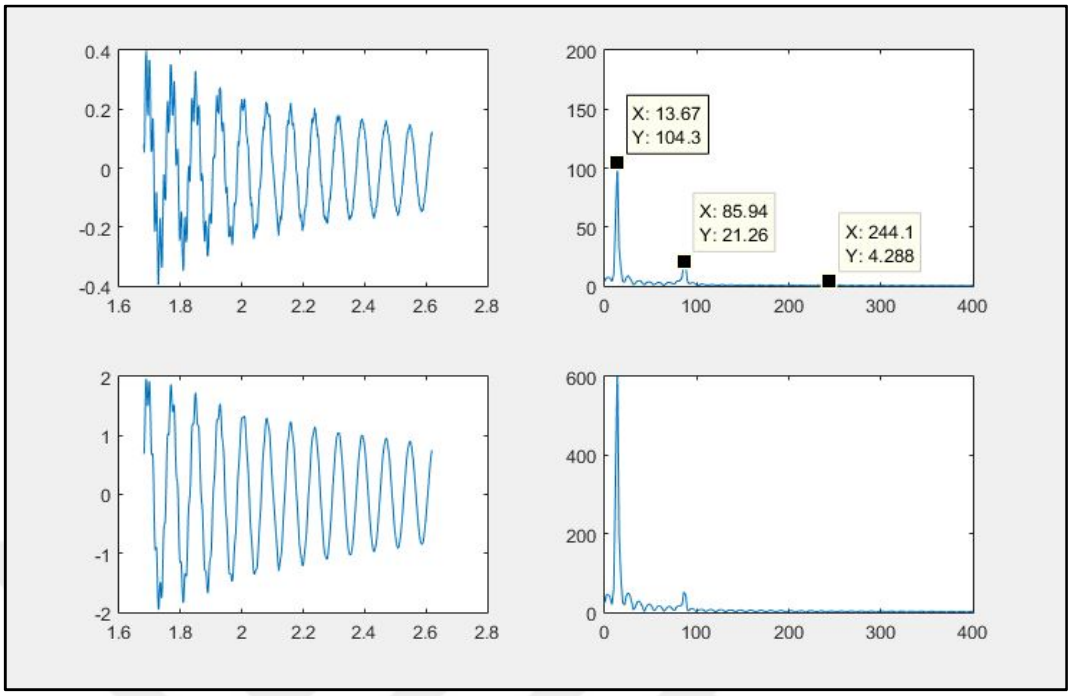

Figure 7.22 Frequency values of HG3 specimen (Personal archive, 2018)

7.6 Numerical Analysis

In the numerical analysis, the natural frequency values were obtained using ANSYS Mechanical APDL 16.0 finite element software for the clamped-free boundary condition. Modulus of elasticity and Poisson's ratio which were obtained from tensile test with strain gauge, were used as an input in the numerical analyses. Beam188 element type was chosen and the finite element model has hundred elements. First ten mode natural frequency values were obtained by ANSYS finite element software. Mode shapes of natural frequencies are shown in figures from Figure 7.11 to Figure 7.20 for pure resin specimen.

Figure 7.23 Finite element model (Personal archive, 2018)

The finite element model length was designed as 220 mm to compare results with experimental analysis. Because in experimental analysis, each test gripper holds the specimens at 30 mm from the end of them. Figure 7.23 shows the finite element model created by ANSYS Mechanical APDL 16.0 finite element software.

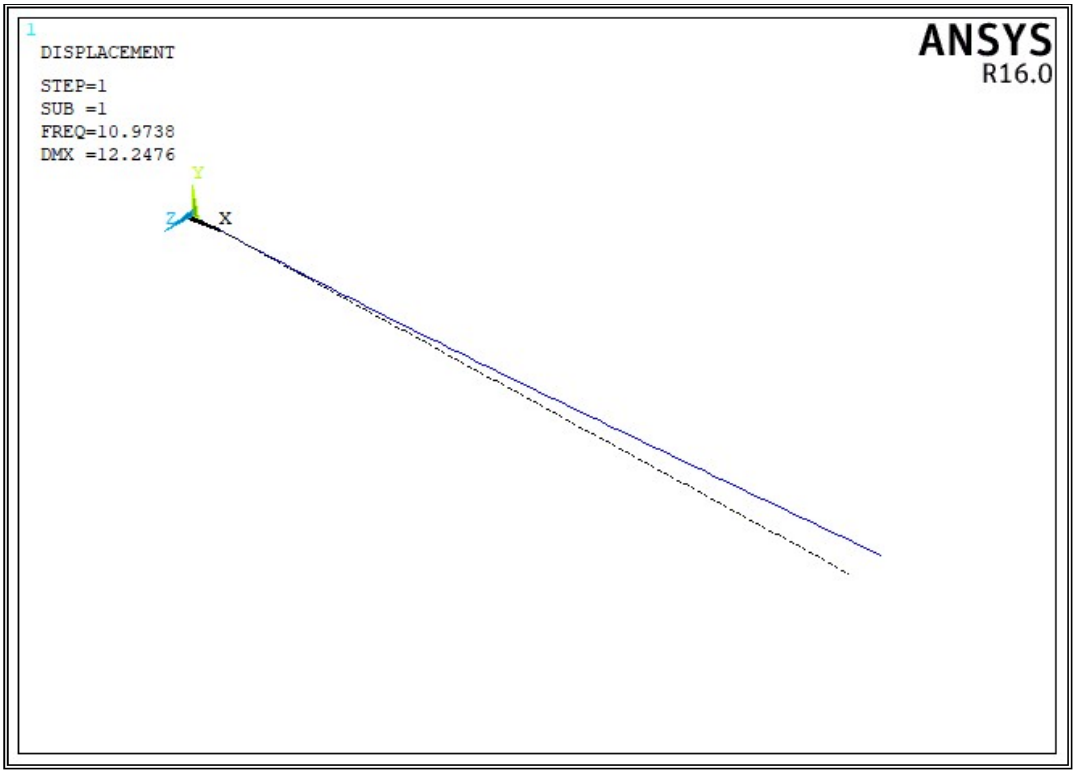

Figure 7.24 Vibration response for pure resin associated with first mode (Personal archive, 2019)

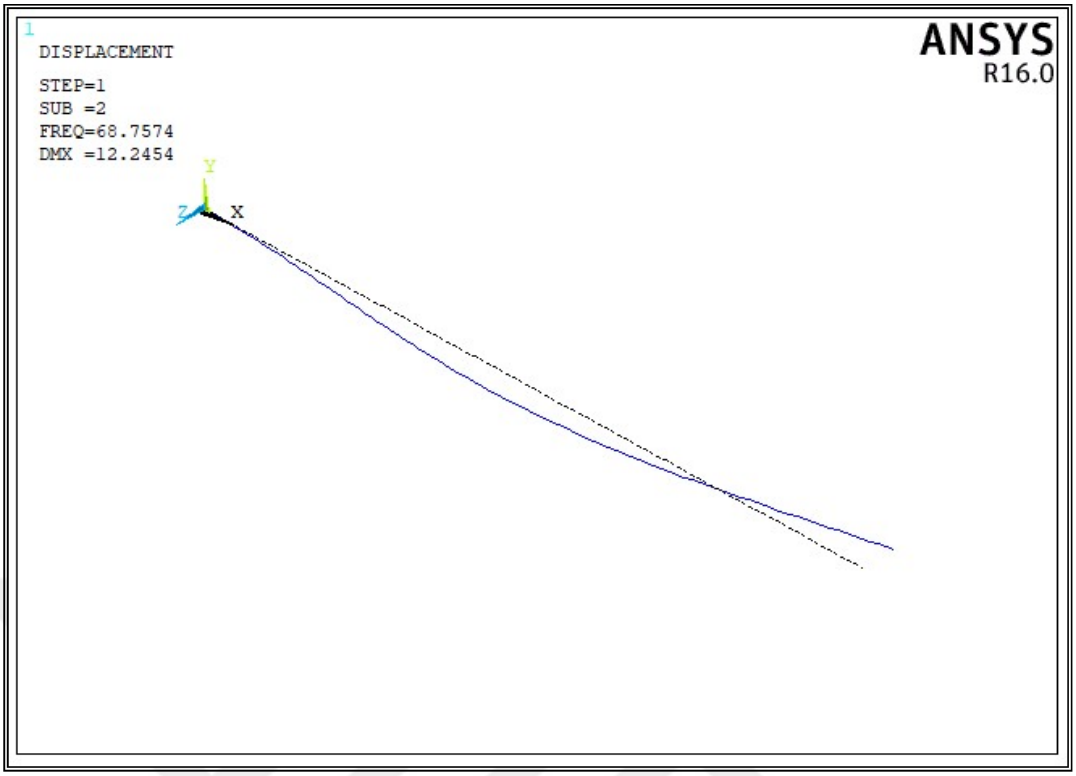

Figure 7.25 Vibration response for pure resin associated with second mode (Personal archive, 2019)

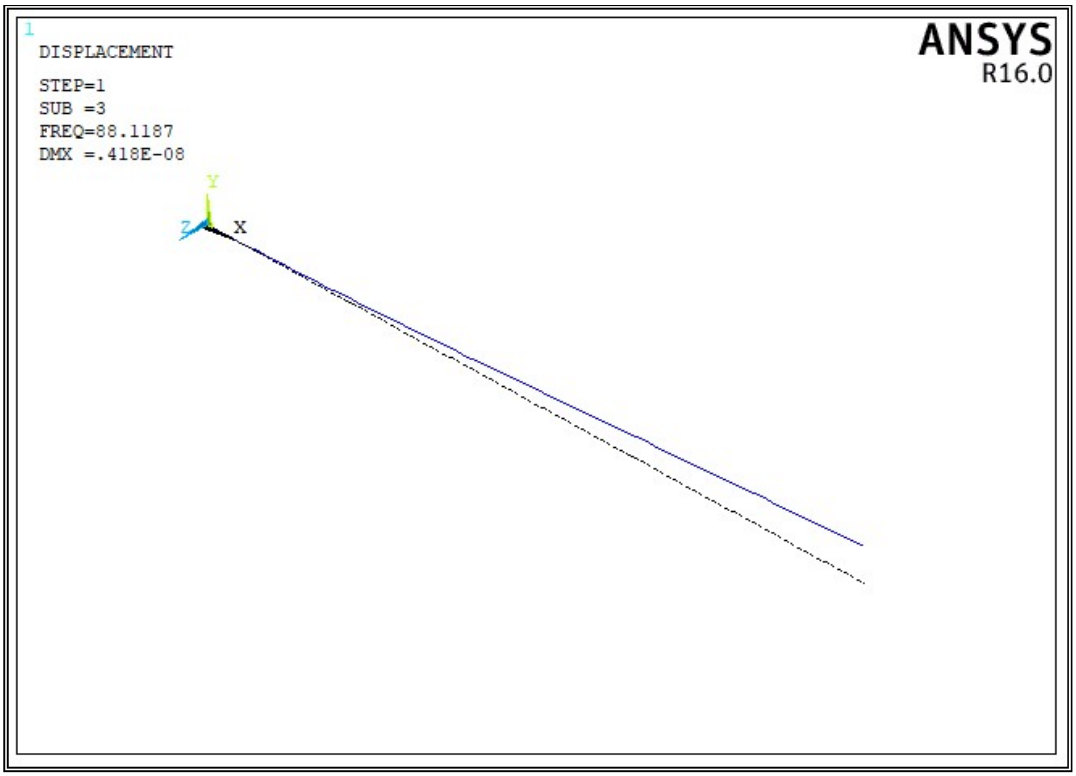

Figure 7.26 Vibration response for pure resin associated with third mode (Personal archive, 2019)

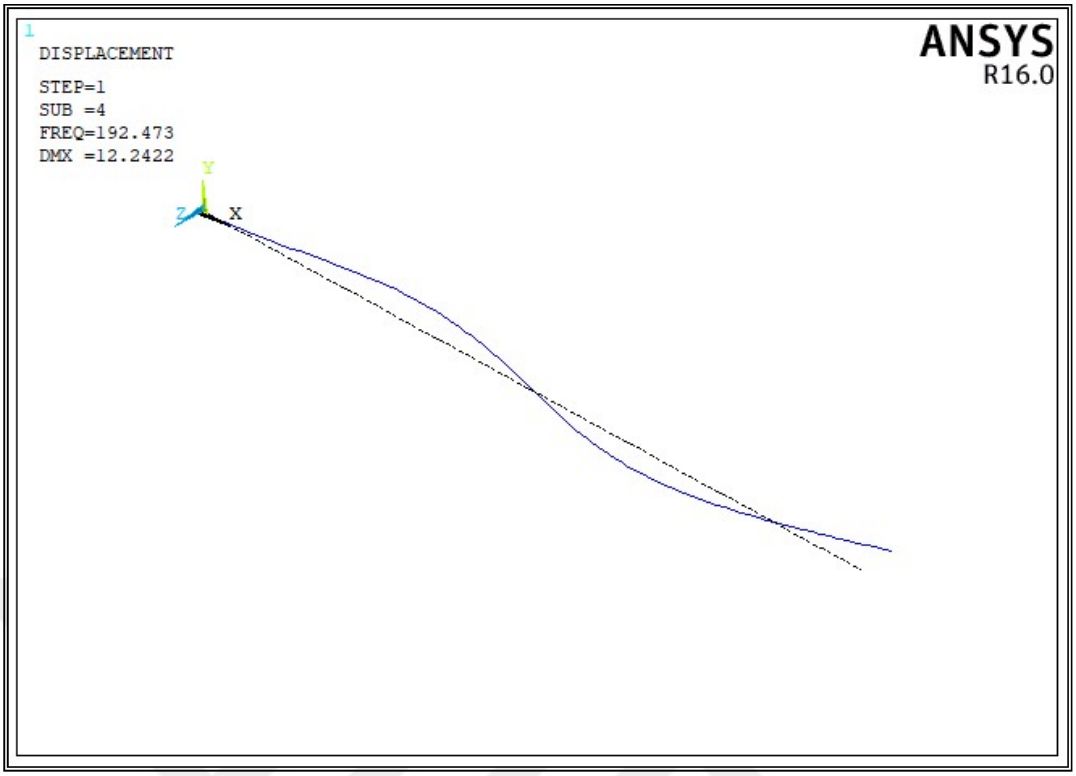

Figure 7.27 Vibration response for pure resin associated with fourth mode (Personal archive, 2019)

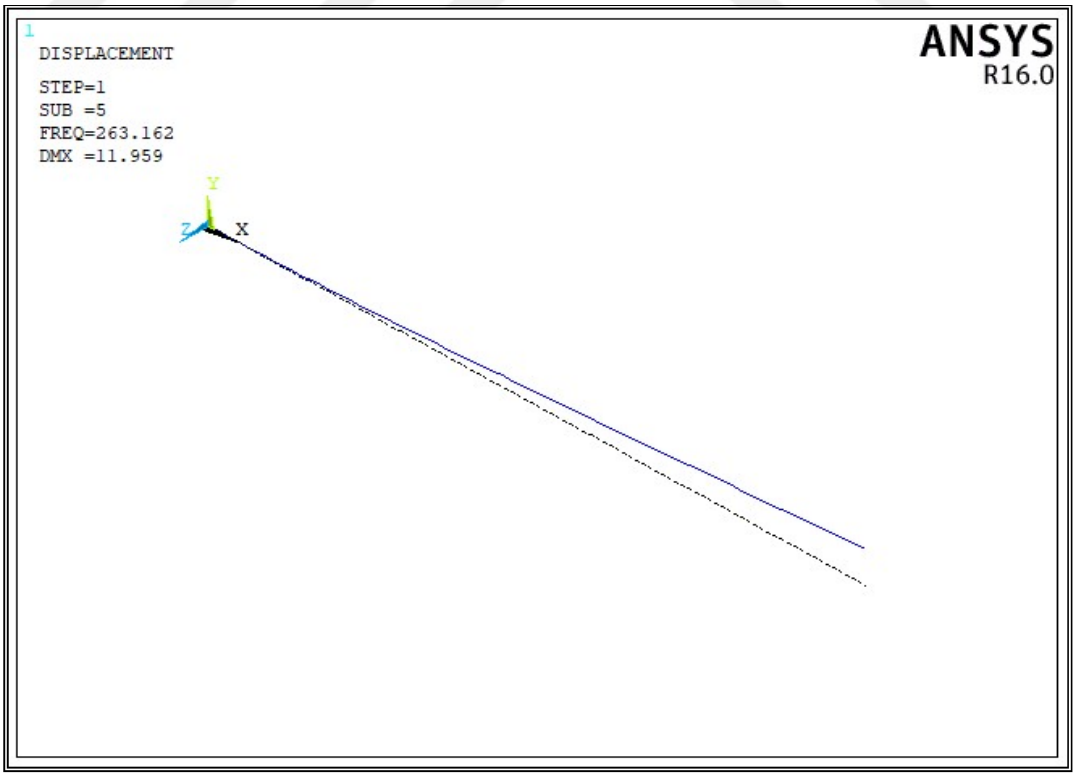

Figure 7.28 Vibration response for pure resin associated with fifth mode (Personal archive, 2019)

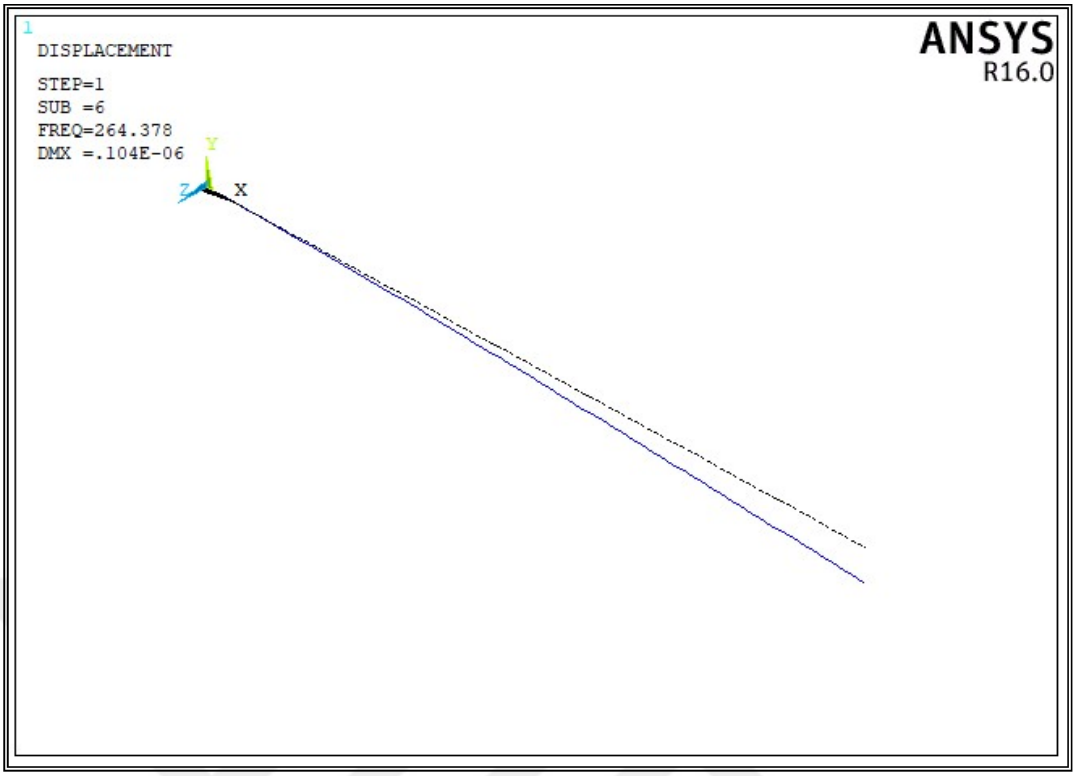

Figure 7.29 Vibration response for pure resin associated with sixth mode (Personal archive, 2019)

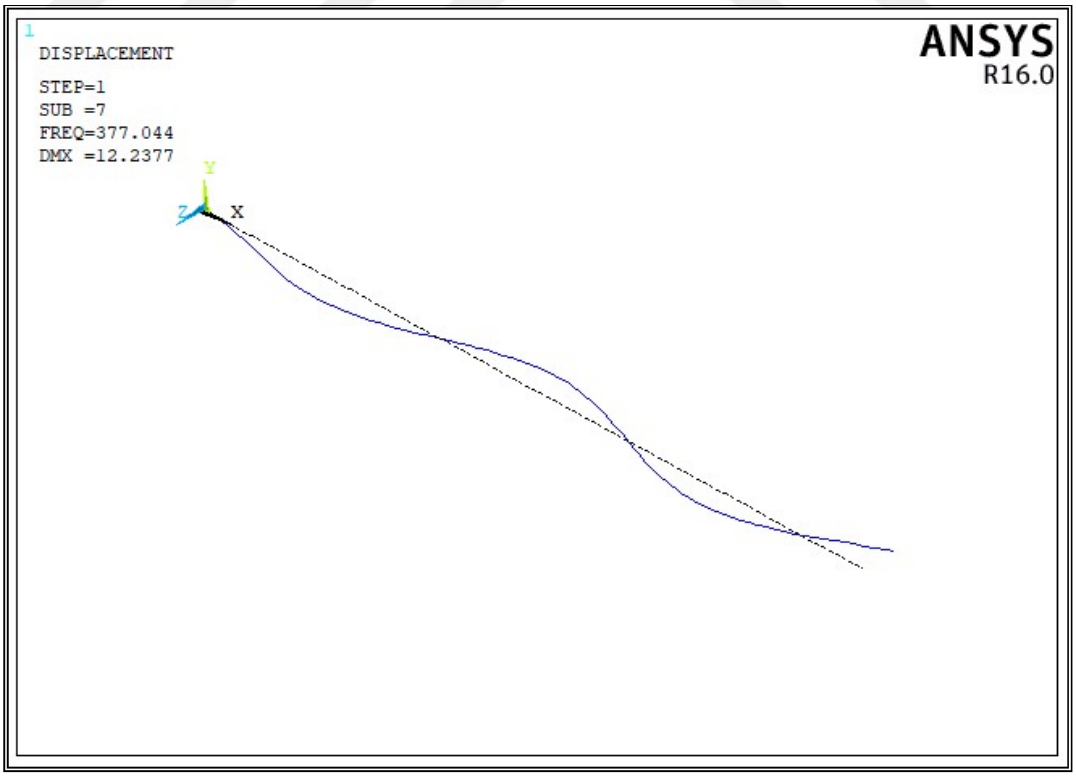

Figure 7.30 Vibration response for pure resin associated with seventh mode (Personal archive, 2019)

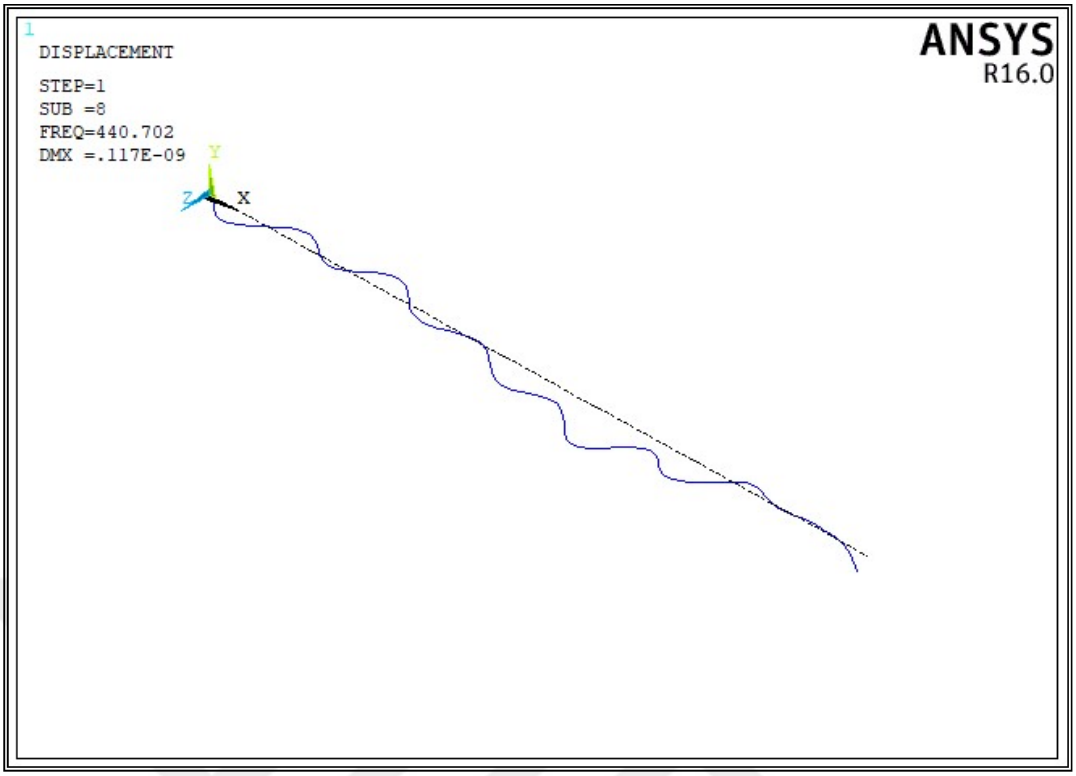

Figure 7.31 Vibration response for pure resin associated with eighth mode (Personal archive, 2019)

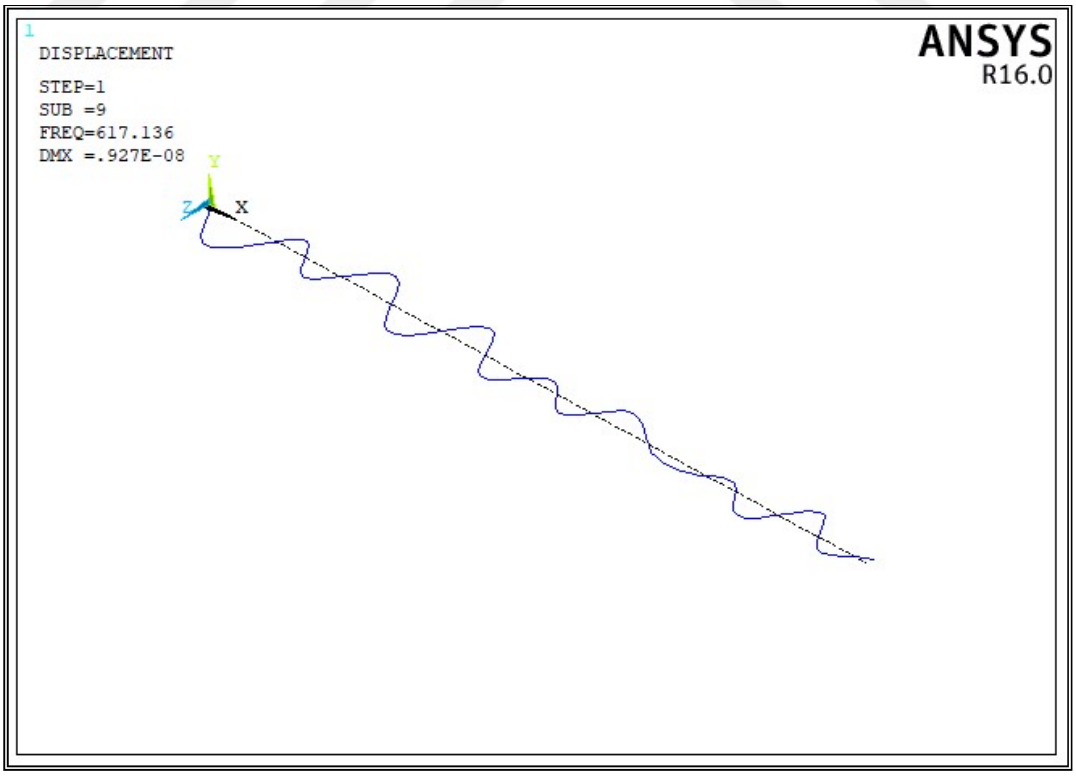

Figure 7.32 Vibration response for pure resin associated with ninth mode (Personal archive, 2019)

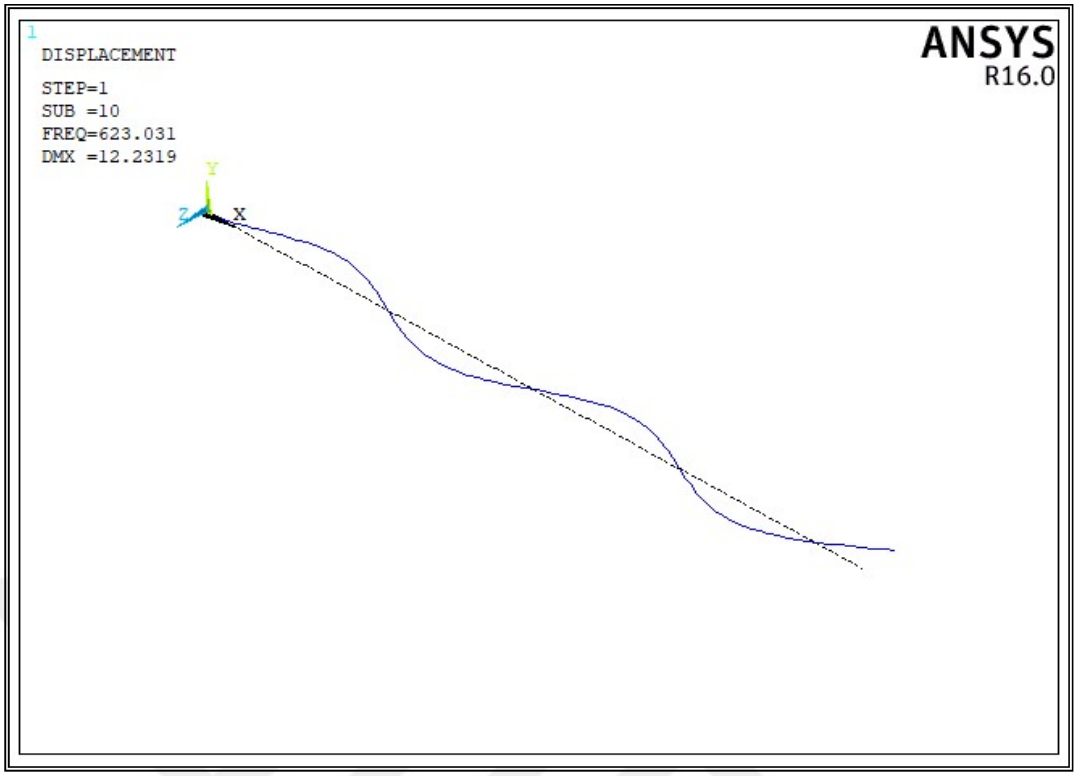

Figure 7.33 Vibration response for pure resin associated with tenth mode (Personal archive, 2019)

7.7 Results of Vibration Analysis

7.7.1 Vibration Response Obtained from Numerical Analysis

The effects of mineral types and weight ratios on the vibration response according to mode shapes were analyzed with ANSYS finite element software. Ten modal buckling load values were given in Table 7.1 and Figure 7.34 for pure resin, huntite, graphene, nano sized huntite and mix of huntite-graphene specimens.

In general, addition 1% weight ratio of mineral shows good results on the frequency values. The lowest frequency value among the specimens is natural frequency of pure resin. It shows that addition mineral increase the natural frequency value up to a certain amount that is 1 wt%.

Table 7.1 Natural frequency values [Hertz]

	Rc	H05	H1	H3	G05	G1	G3
Mode1	10.974	16.451	19.438	15.769	17.543	12.614	15.561
Mode2	68.757	103.020	121.710	98.752	109.860	79.024	97.482
Mode3	88.119	132.980	155.570	127.650	142.790	100.340	125.710
Mode4	192.470	263.200	282.590	252.310	280.790	221.180	272.800
Mode5	263.160	288.160	340.300	276.210	307.300	274.840	311.130
Mode6	264.380	398.980	466.760	382.990	428.390	301.060	377.150
Mode7	377.040	563.810	665.510	540.440	601.280	433.180	534.190
Mode8	440.700	665.080	778.060	638.420	714.110	501.840	628.690
Mode9	617.140	930.220	1089.600	891.670	992.060	702.760	880.380
Mode10	623.030	931.340	1097.300	894.010	1000.000	715.580	882.220

	Rc	Hn05	Hn1	Hn3	HG05	HG1	HG3
Mode1	10.974	15.303	17.413	15.786	16.446	16.970	14.761
Mode2	68.757	95.835	109.030	98.858	102.990	106.270	92.468
Mode3	88.119	122.540	140.120	126.970	133.760	137.320	120.360
Mode4	192.470	253.110	261.120	252.490	263.220	271.520	258.750
Mode5	263.160	268.070	304.890	276.500	288.080	297.240	283.500
Mode6	264.380	367.640	420.400	380.950	401.310	412.000	361.110
Mode7	377.040	524.570	596.370	541.000	563.670	581.590	506.630
Mode8	440.700	612.840	700.780	635.030	668.960	686.780	601.940
Mode9	617.140	858.180	981.330	889.260	930.000	959.560	836.600
Mode10	623.030	865.600	983.550	892.570	936.770	961.730	842.930

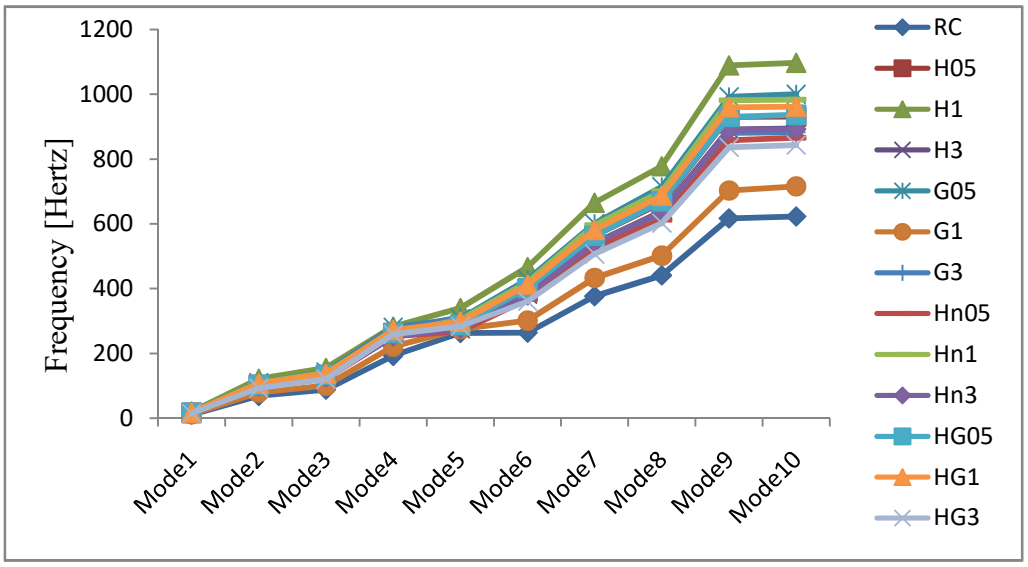

Figure 7.34 Ten mode natural frequency values obtained from numerical analysis

7.7.2 Vibration Response Obtained from Experimental Analysis

Effects of mineral types and weight ratios on the natural frequency values of the composite beams were obtained experimentally. For determination of natural frequencies, response data were processed using Matlab 2015 with function of Fast Fourier Transform (FFT) method. Natural frequency responses of all specimens were obtained graphically from Figure 7.10 to Figure 7.22.

Natural frequency values obtained by the numerical and experimental analyses are given in Table 7.2, Figure 7.35, Figure 7.36 and Figure 7.37. For addition of 1 wt% mineral into the resin, graphene reduces natural frequency values while huntite increases comparision with addition of 0.5 wt% mineral. When the frequency values for huntite+graphene specimens were examined, huntit mineral showed more dominant than graphene mineral.

Table 7.2 Natural frequency [Hertz] obtained by the experimental analysis

		Specimen	Mod1	Mod2	Mod3
Resin	0%	RC	7.813	68.36	199.2
Huntite	0.5%	H05	17.58	97.66	273.4
	1%	H1	19.53	109.4	287.1
	3%	H3	15.63	107.4	302.7
Graphene	0.5%	G05	15.63	105.5	298.8
	1%	G1	11.72	85.94	252
	3%	G3	15.63	82.03	212.9
Huntite nano size	0.5%	Hn05	13.67	97.66	287.1
	1%	Hn1	19.53	109.4	318.4
	3%	Hn3	15.63	107.4	302.7
Huntite+ Graphene	0.5%	HG05	15.63	103.5	293
	1%	HG1	15.63	109.4	308.6
	3%	HG3	13.67	85.94	244.1

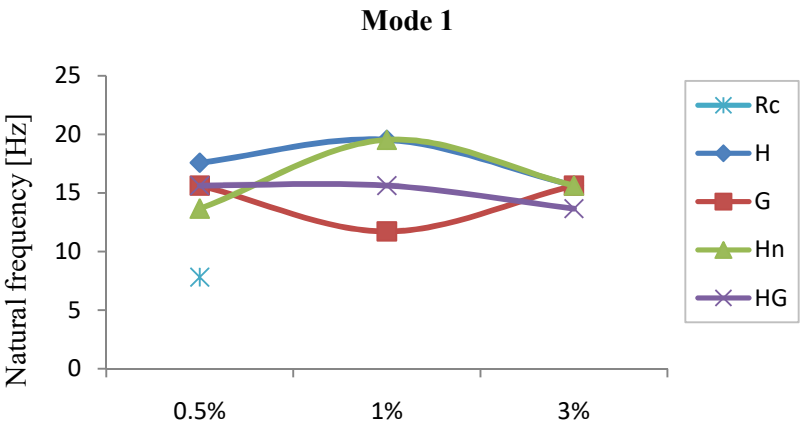

Figure 7.35 Mode 1 natural frequency according to weight ratios

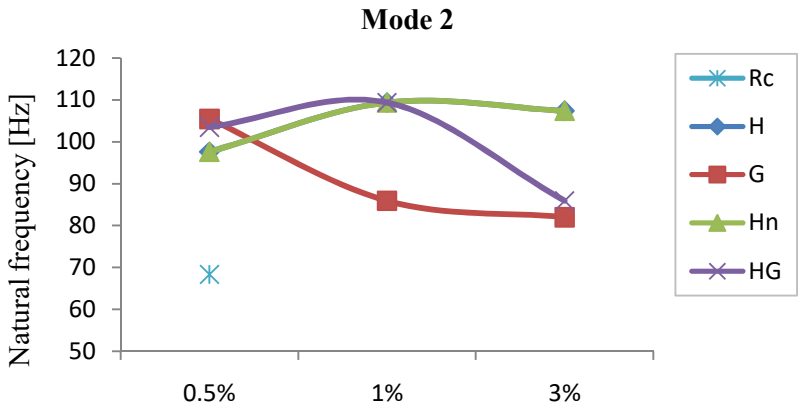

Figure 7.36 Mode 2 natural frequency according to weight ratios

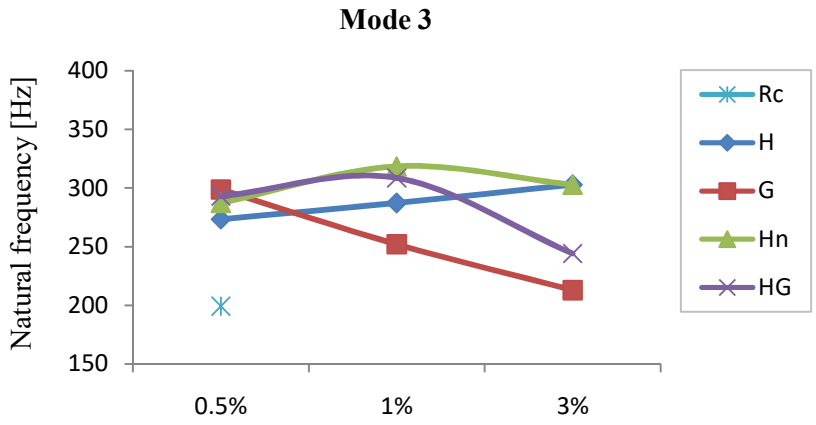

Figure 7.37 Mode 3 natural frequency according to weight ratios

7.7.3 Comparison Experimental and Numerical Analyses

The effects of mineral types and weight ratios on the Mode 1 natural frequency between numerical and experimental analyses were given in Table 7.3 and Figure 7.38. In addition, differences between numerical and experimental analyses were calculated. As shown in Table 7.3, results obtained by the numerical and experimental analyses are so close to each other.

Table 7.3 First mode natural frequency [Hertz] obtained by the numerical and experimental analyses.

	wt%	Specimen	Experiment	ANSYS	Diffrerences%
Resin	0%	RC	7.813	10.974	-28.8
Huntite	0.5%	H05	17.58	16.451	6.9
	1%	H1	19.53	19.438	0.5
	3%	H3	15.63	15.769	-0.9
Graphene	0.5%	G05	15.63	17.543	-10.9
	1%	G1	11.72	12.614	-7.1
	3%	G3	15.63	15.561	0.4
Huntite nano size	0.5%	Hn05	13.67	15.303	-10.7
	1%	Hn1	19.53	17.413	12.2
	3%	Hn3	15.63	15.786	-1.0
Huntite+ Graphene	0.5%	HG05	15.63	16.446	-5.0
	1%	HG1	15.63	16.970	-7.9
	3%	HG3	13.67	14.761	-7.4

For all specimens reinforced by the minerals, the natural frequency obtained by both numerical and experimental analyses are higher than the pure resin, as shown in Figure 7.38. Especially, the graphene-resin specimen exhibits reduction in the natural frequency value compared to other specimens while the huntite-resin specimen exhibits incresion in the natural frequency value compared to other specimens. The critical buckling load of Hn1 specimen determined by both numerical and experimental analyses reach the maximum natural frequency value.

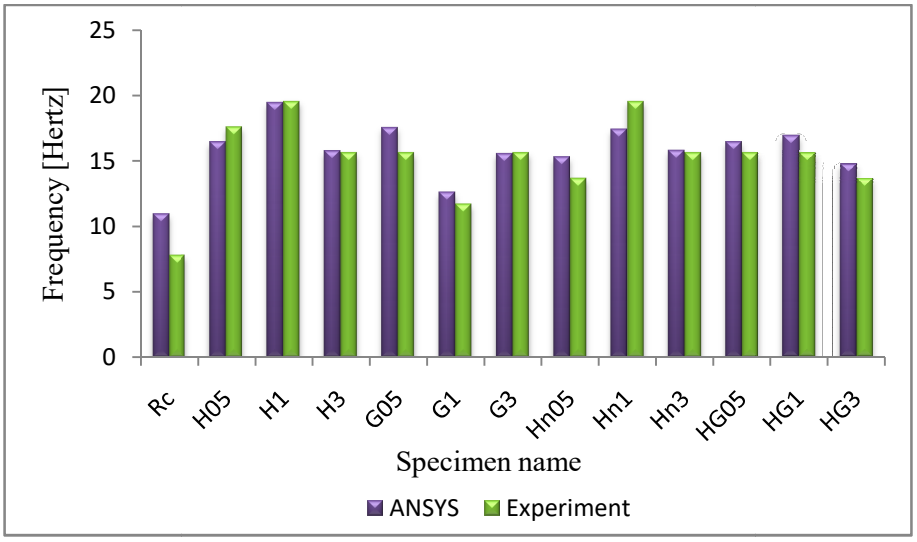

Figure 7.38 Natural frequency values [Hertz] obtained by the numerical and experimental analyses

7.7.4 Damping ratio

Vibration is known as damped vibration if there is energy loss during oscillation. In that system, damping ratio is measured the reduction rate of the oscillation amplitudes. Damping ratio was calculated using Matlab 2015 considering function of Fast Fourier Transform (FFT) method. Amplitudes of vibration were obtained with the graphic shown in Figure 7.39. Then, mean values were calculated using the logarithmic decrement method. The effects of mineral types and weight ratio on damping ratios were obtained experimentally.

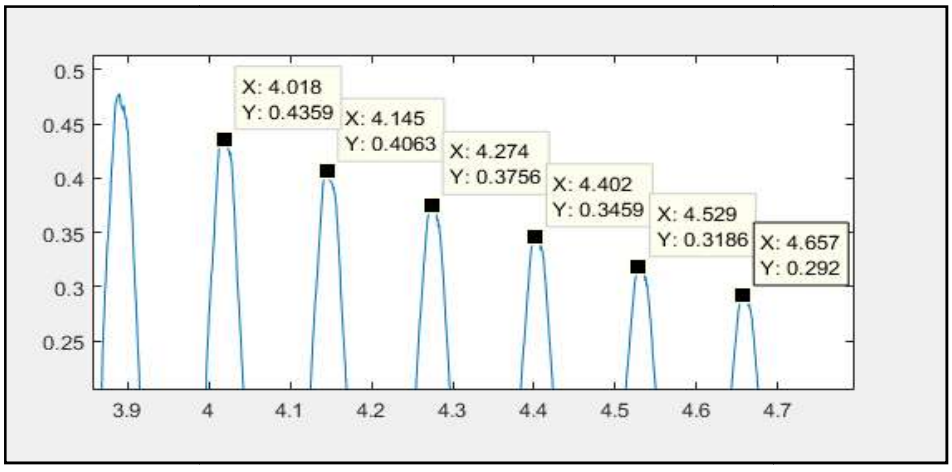

Figure 7.39 Damping ratio obtained by experimental analysis

Table 7.4 Calculation of damping ratio obtained by experimental analysis

Rc	1.damping ratio		2.damping ratio		3.damping ratio		
	y1=	0.43	y3=	0.372	y5=	0.31	
	y2=	0.40	y4=	0.34	y6=	0.291	Mean
	x=	0.011112	ξ=	0.014314	ξ=	0.009036	0.011487416
H0.5	1.damping ratio		2.damping ratio		3.damping ratio		
	y1=	2.107	y3=	1.88	y5=	1.579	
	y2=	1.96	y4=	1.702	y6=	1.481	Mean
	ξ=	0.011509	ξ=	0.015829	ξ=	0.010197	0.012511808
G0.5	1.damping ratio		2.damping ratio		3.damping ratio		
	y1=	2.016	y3=	1.752	y5=	1.533	
	y2=	1.862	y4=	1.625	y6=	1.425	Mean
	ξ=	0.012646	ξ=	0.011976	ξ=	0.011626	0.012082643
Hn0.5	1.damping ratio		2.damping ratio		3.damping ratio		
	y1=	0.841	y3=	0.738	y5=	0.649	
	y2=	0.787	y4=	0.693	y6=	0.607	Mean
	ξ=	0.010561	ξ=	0.010013	ξ=	0.010647	0.010407169
HG0.5	1.damping ratio		2.damping ratio		3.damping ratio		
	y1=	0.615	y3=	0.551	y5=	0.496	
	y2=	0.581	y4=	0.527	y6=	0.468	Mean
	ξ=	0.009051	ξ=	0.007088	ξ=	0.009248	0.008462134
H1	1.damping ratio		2.damping ratio		3.damping ratio		
	y1=	1.267	y3=	1.112	y5=	0.976	
	y2=	1.195	y4=	1.044	y6=	0.914	Mean
	ξ=	0.009311	ξ=	0.010042	ξ=	0.010445	0.009932814
G1	1.damping ratio		2.damping ratio		3.damping ratio		
	y1=	1.935	y3=	1.626	y5=	1.374	
	y2=	1.752	y4=	1.491	y6=	1.271	Mean
	ξ=	0.01581	ξ=	0.013794	ξ=	0.012401	0.014001436

Table 7.4 continue

Hn1	1.damping ratio		2.damping ratio		3.damping ratio		
	y1=	0.802	y3=	0.708	y5=	0.624	
	y2=	0.752	y4=	0.665	y6=	0.587	Mean
	ξ=	0.010245	ξ=	0.009972	ξ =	0.009728	0.009981429

HG1	1.damping ratio		2.damping ratio		3.damping ratio		
	y1=	0.694	y3=	0.614	y5=	0.540	
	y2=	0.653	y4=	0.576	y6=	0.507	Mean
	ξ =	0.009691	ξ =	0.010167	ξ =	0.010036	0.009964739

H3	1.damping ratio		2.damping ratio		3.damping ratio		
	y1=	0.510	y3=	0.454	y5=	0.409	
	y2=	0.480	y4=	0.431	y6=	0.387	Mean
	ξ =	0.009648	ξ =	0.008274	ξ =	0.008799	0.008907236

G3	1.damping ratio		2.damping ratio		3.damping ratio		
	y1=	0.227	y3=	0.209	y5=	0.189	
	y2=	0.218	y4=	0.197	y6=	0.181	Mean
	ξ =	0.006438	ξ =	0.00941	ξ =	0.006883	0.007577419

Hn3	1.damping ratio		2.damping ratio		3.damping ratio		
	y1=	0.311	y3=	0.282	y5=	0.254	
	y2=	0.294	y4=	0.267	y6=	0.24	Mean
	ξ =	0.008946	ξ =	0.008699	ξ =	0.009023	0.008889349

HG3	1.damping ratio		2.damping ratio		3.damping ratio		
	y1=	0.433	y3=	0.385	y5=	0.341	
	y2=	0.409	y4=	0.363	y6=	0.321	Mean
	ξ =	0.009075	ξ =	0.009364	ξ =	0.009619	0.009352831

As shown in Figures 7.39, 7.40 and Table 7.4, damping ratio values are so close to each other. The maximum value is observed for graphene 1% weight ratio.

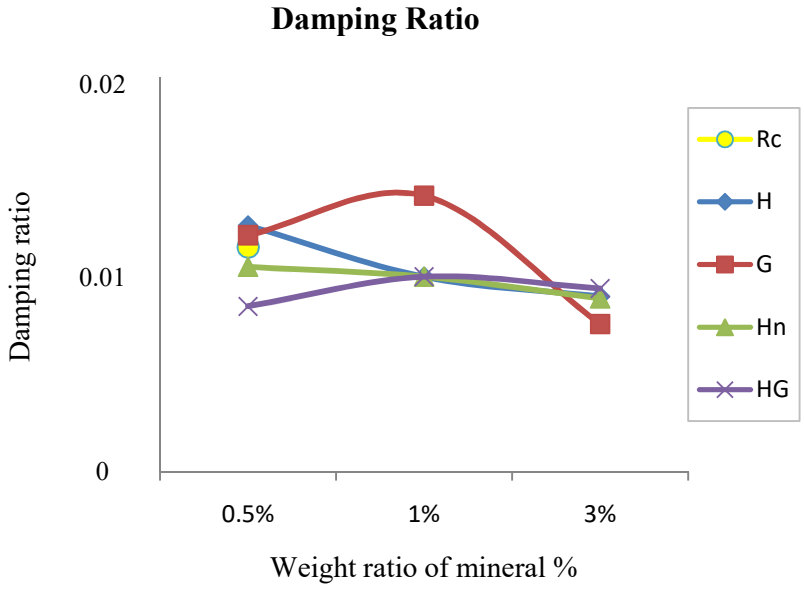

Figure 7.40 Damping ratio according to weight ratios

CHAPTER EIGHT
CONCLUSIONS

In the present study, mechanical properties of composite materials reinforced by mineral were investigated. Mechanical properties of the composite specimens reinforced by minerals were determined experimentally and numerically for different weight ratios of mineral particles. Graphene and huntite minerals were added to epoxy resin to examine the effects of mineral types on mechanical properties. In addition, the effect of non-layered huntite mineral unlike graphene, in nano-sized grain structure was investigated. For these purposes, 0.5 wt%, 1 wt% and 3 wt% graphene and huntite minerals were added to the epoxy and huntite-epoxy, graphene-epoxy, huntite-graphene-epoxy mineral reinforced samples were manufactured. In the numerical analyses, the critical buckling load and free vibration response were obtained using ANSYS Mechanical APDL 17.0 finite element software. In addition to numerical analyses, tensile test, dynamic mechanical analysis, vibration experiment and buckling analysis were carried out to determine the mechanical properties experimentally.

8.1 Tensile Test

The effects of mineral types and weight ratios on the mechanical properties of the composites were investigated experimentally.

- According to stress-strain values, specimens reinforced by huntite mineral were broken with more elongation than graphene mineral added specimes. Namely, it shows that huntite increases the ductility of the material.

- The maximum value in stress was observed in the specimens reinforced by huntite mineral.

8.2 Buckling Analysis

The effects of mineral types and weight ratios on the buckling loads were examined with numerically and experimentally. First five modal buckling loads were obtained for all specimens.

- In general, huntite mineral showed good results on the buckling load value while graphene specimens caused less change on the buckling load values.

- Between mixture of huntite and graphene mineral added specimens, buckling load of the maximum graphene amount (HG3) is minimum for five mode shapes.

- Results obtained by the numerical and experimental analyses are so close to each other. When the differences between numerical and experimental studies are examined, it is seen that the maximum difference is %8.830. This result shows that the experimental and numerical analyses are consistent.

- For all specimens reinforced by the minerals, the critical buckling load values obtained by both numerical and experimental analyses are higher than the pure resin.

- The nano-sized particle structure of huntite mineral shows a significant increase on critical buckling load values compared to other specimens. The critical buckling load of Hn1 specimen determined by both numerical and experimental analyses reaches the highest buckling load value.

- There is negative effect on the critical buckling load by increasing the weight ratio of graphene amount.

- It is observed that the critical buckling load results are increased dramatically with adding the mineral.

8.3 Dynamic Mechanical Analysis

Glass transition temperatures, storage modulus, loss modulus and tan δ were obtained from the dynamic mechanical analysis.

- The glass transition temperature of the resin was found as 82.32 °C that was obtained from maximum point of loss modulus at DMA. When the specimens catalog is examined, it is seen that the glass transition temperature for the resin is 80-85 °C. This data shows the compatibility of the results between real value and DMA for the resin.

- Transition temperature obtained from graphics of loss modulus gives more accurate results according to obtained from graphics of tan δ. Glass transition temperatures of the specimens are close to each other.

- Glass transition temperatures of the specimens are close to each other. But, if the temperature is increased, it will be seen that the graphene mineral that has 1% weight ratio will pass to the rubber zone at last according to other specimens.

- The glass transition temperature was also investigated for mineral weight ratios. There is almost no difference between transition temperatures of the resin and the others at 0.5 wt%.

- When the investigation of 1 wt%, graphene and mixture of huntite and graphene mineral increased the transition temperature while huntit and huntit nano sized mineral decreased.

- Lastly, adding 3 wt% of mineral decreased the glass transition temperature, comparison with pure resin.

- The maximum values of storage modulus and loss modulus are at initial temperature and glass transition temperature, respectively.

- Pure resin has minimum loss modulus. The reason increased loss modulus with adding mineral is internal friction force between mineral particle and resin. Because this friction force causes internal heat and loss.

- When the storage modulus is examined, the maximum value occurs at initial temperature (35°C). When the temperature increases, stiffness decreases by approaching the rubber field after the transition temperature. In other words, material has higher stiffness at initial temperature.

- When compared values of storage modulus and loss modulus, it is seen that they have so similar behaviour.

- Having lowest storage modulus and loss modulus values among the specimens is pure resin. It shows that addition of mineral increases these values.

- Tan δ is the ratio of loss modulus to storage modulus. Pure epoxy has maximum tan δ value because of molecular mobility.

8.4 Vibration Analysis

The effects of mineral types and weight ratios on the vibration behavior were examined numerically and experimentally for pure resin, huntite, graphene, nano sized huntite and mix of huntite-graphene specimens.

- In general, addition of 1% weight ratio of mineral increases the natural frequency values. Having lowest natural frequency value among the specimens is pure resin. It shows that addition mineral increase the natural frequency up to a certain amount that is 1 wt%.

- The addition of minerals to the resin in the 1% weight ratio of graphene added specimens show reducing effect on the natural frequency values, while the huntite added specimens show increased effect.

- When the natural frequency values for huntite+graphene specimens were examined, huntite mineral has more dominant effect than graphene mineral.

- The effects of mineral types and weight ratios on the first fundamental natural frequency between numerical and experimental analyses were investigated. In addition, differences between numerical and experimental analyses were calculated. The maximum difference between anayses is 28.8%.

- For all specimens reinforced by the minerals, the natural frequencies obtained by both numerical and experimental analysis are higher than the pure resin beam. Especially, the graphene-resin specimen exhibits the reduction in the natural frequency compared to other specimens while the huntite-resin specimen exhibits increase on the natural frequency compared to other specimens.

- Damping ratio values are close to each other. The maximum value is observed for graphene 1 wt%.

REFERENCES

Atay, H. Y., & Çelik, E. (2013). Mechanical properties of flame-retardant huntite and hydromagnesite-reinforced polymer composites. *Polymer-Plastics Technology and Engineering*, *52*(2), 182-188.

Baştürk, E., Madakbaş, S., Karadoğan, B., & Vezir Kahraman, M. (2016). Preparation and thermal properties of polyethylene terephthalate/huntite–hydromagnesite composites. *Polymer Composites*, *37*(11), 3275-3279.

Bratukhin, A. G., & Bogolyubov, V. S. (1995). *Composite manufacturing technology*. (1st ed.). UK: Springer Science & Business Media.

Chee, S. S., Jawaid, M., & Sultan, M. T. (2017). Thermal stability and dynamic mechanical properties of kenaf / bamboo fibre reinforced epoxy composites, *BioResources*, *12*(4), 7118-7132.

D'Aloia, A., Proietti, A., Bidsorkhi, H., Tamburrano, A., De Bellis, G., Marra, F., Bregnocci, A., & Sarto, M. (2018). Electrical, mechanical and electromechanical properties of graphene-thermoset polymer composites produced using acetone-DMF solvents. *Polymers, 10*(1), 82.

Dunson, D. (2017). *Characterization of polymers using dynamic mechanical analysis (DMA)*. Retrieved February, 2019, from https://www.eag.com/wp-content/uploads/2017/09/M-022717-Characterization-of-Polymers-using-Dynamic-Mechanical-Analysis.pdf

Gay, D., & Hoa, S. V. (2003). *Composite materials: design and applications*. (1st ed.). Boca Raton: CRC press.

Gere, J. M. (2004). *Mechanics of materials* (6th ed.). USA: Thomson Learning.

Gibson, R. F. (2011). *Principles of composite material mechanics*. (8th ed.). Boca Raton: CRC Press.

Govorov, A., Wentzel, D., Miller, S., Kanaan, A., & Sevostianov, I. (2018). Electrical conductivity of epoxy-graphene and epoxy-carbon nanofibers composites subjected to compressive loading. *International Journal of Engineering Science*, *123*, 174-180.

Haeri, S. Z., Asghari, M., & Ramezanzadeh, B. (2017). Enhancement of the mechanical properties of an epoxy composite through inclusion of graphene oxide nanosheets functionalized with silica nanoparticles through one and two steps sol-gel routes. *Progress in Organic Coatings*, *111*, 1-12.

Hancock, Y. (2011). The 2010 Nobel Prize in physics — Ground-breaking experiments on graphene. *Journal of Physics D: Applied Physics*, *44*(47), 473001.

He, J., Wang, H., Su, Z., Guo, Y., Tian, X., Qu, Q., & Lin, Y. L. (2019). Thermal conductivity and electrical insulation of epoxy composites with graphene-SiC nanowires and BaTiO3. *Composites Part A: Applied Science and Manufacturing*, *117*, 287-298.

Hibbeler, R.C. (2004). *Mechanics of Materials.* (8th ed.). USA: Pearson Prentice Hall.

Hollingbery, L. A., & Hull, T. R. (2010). The thermal decomposition of huntite and hydromagnesite—a review. *Thermochimica Acta*, *509*(1-2), 1-11.

Jamali, N., Khosravi, H., Rezvani, A., & Tohidlou, E. (2019). Mechanical properties of multiscale graphene oxide/basalt fiber/epoxy composites. *Fibers and Polymers*, *20*(1), 138-146.

Kanbur, Y., & Tayfun, Ü. (2017). Polipropilen/huntit kompozitlerinin mekanik, fiziksel ve morfolojik özellikleri. *Sakarya University Journal of Science*, *21*(5), 1045-1050.

Karthik, P. S., Himaja, A. L., & Singh, S. P. (2014). Carbon-allotropes: synthesis methods, applications and future perspectives. *Carbon letters*, *15*(4), 219-237.

Kaw, A. K. (2006). *Mechanics of composite materials*. (2th ed.). Boca Raton: CRC Press.

Kaya, Muammer. (1998). Alev geciktirici ve duman bastırıcı katkı maddeleri. *Eskişehir Osmangazi Üniversitesi Mühendislik ve Mimarlık Fakültesi Dergisi*, *11*(2), 77-88.

Lee, H., & Neville, K. (1967). *Handbook of epoxy resins* (1st ed.). New York: McGraw-Hill

Li, Y., Wang, S., Wang, Q., & Xing, M. (2018). A comparison study on mechanical properties of polymer composites reinforced by carbon nanotubes and graphene sheet. *Composites Part B: Engineering*, *133*, 35-41.

Mahmood, H., Vanzetti, L., Bersani, M., & Pegoretti, A. (2018). Mechanical properties and strain monitoring of glass-epoxy composites with graphene-coated fibers. *Composites Part A: Applied Science and Manufacturing*, *107*, 112-123.

Mallick, P. K. (2008). *Fiber-reinforced composites: materials, manufacturing, and design*. (3th ed.). Boca Raton: CRC Press.

Mazumdar, S. (2002). *Composites manufacturing: materials, product, and process engineering* (5th ed.). Boca Raton: CRC Press.

Menard, K. P. (2008). *Dynamic mechanical analysis: A practical introduction.* (2th ed.). Boca Raton: CRC Press.

Radadiva, T. M. (2015). Properties of graphene. *European Journal of Material Sciences, 2* (1), 6-18.

Rao, S. S., (2011). *Mechanical vibrations* (5th ed.). Upper Saddle River: Prentice hall.

Seki, Y., Sever, K., Sarikanat, M., Sakarya, A., & Elik, E. (2013). Effect of huntite mineral on mechanical, thermal and morphological properties of polyester matrix. *Composites Part B: Engineering*, *45*(1), 1534-1540.

Sepe, M. P. (1998). *Dynamic mechanical analysis for plastics engineering* (1st ed.). USA: Plastics Design Library.

Tang, L. C., Wan, Y. J., Yan, D., Pei, Y. B., Zhao, L., Li, Y. B., Wu, L.B., Jiang, J. X., & Lai, G. Q. (2013). The effect of graphene dispersion on the mechanical properties of graphene/epoxy composites. *Carbon*, *60*, 16-27.

Tong, X. C. (2011). *Advanced materials for thermal management of electronic packaging*. USA: Springer Science & Business Media.

Yakobson, B. I., & Smalley, R. E. (1997). Fullerene nanotubes. *American Scientist*, *85*(4), 324 - 337.

Yıldırım, S., & Çelik, E. (2014). Alev geçiktirici huntit ve hidromanyezit nanopartikül takviyeli polimetrik kompozit kaplamalar. *Afyon Kocatepe Üniversitesi Fen ve Mühendislik Bilimleri Dergisi*, *14*(3), 387-393.

Yücel, B. M. & Gül, Ö. (2017). *Dünyada ve Türkiye'de huntit*. Retrieved March, 2019, from http://www.mta.gov.tr/v3.0/sayfalar/bilgi-merkezi/madenserisi/Huntit

Zhao, L. M., Feng, X., Li, Y. F., & Mi, X. J. (2014). Shape memory effect and mechanical properties of graphene/epoxy composites. *Polymer Science Series A*, *56*(5), 640-645.